2014

Quantum Optical Metrology, Sensing and Imaging

Kebei Jiang
Louisiana State University and Agricultural and Mechanical College, dickjazz@gmail.com

QUANTUM OPTICAL METROLOGY, SENSING AND IMAGING

A Dissertation

Submitted to the Graduate Faculty of the
Louisiana State University and
Agricultural and Mechanical College
in partial fulfillment of the
requirements for the degree of
Doctor of Philosophy

in

The Department of Physics and Astronomy

by
Kebei Jiang
B.S., South China University of Technology, 2007
August 2014

Acknowledgments

First of all, I would like to express my deepest gratitude to my advisor Dr. Jonathan P. Dowling for his consistent guidance, support and encouragement. Despite his humorous appearance, Jon never fails to surprise me with his deep insight into the field of quantum optics and, more importantly, abundant imagination in generating new research ideas. Moreover, Jon's optimistic attitude and easy-going personality makes him one of the best advisors to work with.

I would like to thank Dr. Hwang Lee for his unlimited patience — I often walk in his office with a question in mind and he is always ready to help. I would also like to thank Dr. Mark Wilde for his encouragement and understanding. I wish he had joined our group a few years earlier so that we may have had more chances to collaborate.

Special thanks goes to Dr. Ravi Rau who is extremely knowledgeable and caring of his students. I always remember asking him for advices outside physics and his sorrow and effort during the unfortunate incidence of Sarvnipun Chawla.

I would like to thank Dr. Petr Anisimov, my first postdoctoral colleague, for showing me how research should be done. He also taught me how to use Mathematica and introduced me to Linux, both of which I cannot live without now.

Many thanks to my peers Manish Gupt, Kaushik Seshadreesan, Bhaskar Roy Bardhan, Robinjeet Singh and Christopher Granier for their helpful discussion and quality company. I would like to thank my friends Yang Gao, Weifei Zeng, Zhuojie Huang, E Hu, Katherine Brown, Yue Li, Chloe Zhang, Fei Wu and Gaomin Wang without whom my life will be much less colorful. I would also like to thank Dr. Katherine Brown for proofreading this dissertation.

Last but most important, I am greatly indebted to my parents and my beautiful fiancee Yixing Chen, for their unconditional support and love.

Table of Contents

Abstract

In this dissertation we begin with a brief introduction to quantum optics concentrating on the topics of the noise of quantum optical states, quantum estimation theory, quantum interferometry and the atom-field interaction. This background is necessary for understanding the discussions in later chapters. In particular, quantum interferometry, which is optical interferometry when the light source is a quantum mechanical state, plays a central role in this dissertation. In Chapter 2 we discuss the phase estimation sensitivity of quantum metrology when photon loss is present. In Chapter 3 we extend the discussion to include the phase fluctuation of the system caused by the environment. We model our metrological system with the Mach-Zehnder interferometer (MZI) and use a light field in the symmetric number-path entangled state as the source. In both chapters we use the parity operator as the detection scheme and show that it is optimal under pure dephasing. In Chapter 4 we discuss the application of quantum optical states in remote sensing and propose a new scheme for a quantum radar. Again, our scheme consists of a MZI and a coherent light source. It is shown that using only coherent states of light and quantum homodyne detection, super-resolving ranging and angle determination are achievable. Chapter 5 is devoted to the generation of a super-resolving single-photon number-path entangled state which may serve as a proof-of-principle prototype for quantum lithography. The repeated implementation of MZIs is shown to be able to remove photons coherently from both modes of a symmetric number-path entangled state with arbitrarily high photon number. Lastly, in Chapter 6 we introduce the phenomenon known as polarization self-rotation and discuss its potential in generating a squeezed vacuum state, which has a huge impact in quantum interferometry.

Chapter 1
Introduction

Quantum optics is the study of radiation, mostly in the optical frequency regime, based on the quantum mechanical theorem. It involves the generation, propagation and detection of a light field and its interaction with atoms and molecules. Quantum mechanics was born due to Planck's assumption of simple harmonic oscillators with discrete energy level in the wall of a black-body. Although Planck treated the radiation wave as a classical wave, the idea of 'quantized particle' later inspired Einstein, in his effort to explain the photoelectric effect, to introduce the concept of photons of the radiation field. The unification of the wave- and particle-like aspect of light was achieved by Dirac who associated each mode of the radiation field with a quantized simple harmonic oscillator [1, 2]. In this new theory photons are interpreted as the excitations of normal modes of the electromagnetic field and the old visualization of photons as 'wave-packet' are replaced with non-local oscillations spread out the space. In the first part of this introduction, we present a brief introduction to the quantization of radiation field.

1.1 Field Quantization and Quantum Noise

1.1.1 Field Quantization and States of Radiation Field

Classically speaking, the radiation fields in free space obey the Maxwell's equations [3], which are a set of partial differential equations read

$$\nabla \cdot \mathbf{E} = 0,$$

$$\nabla \cdot \mathbf{B} = 0,$$

$$\nabla \times \mathbf{E} = -\frac{\partial \mathbf{B}}{\partial t},$$

$$\nabla \times \mathbf{B} = \mu_0 \epsilon_0 \frac{\partial \mathbf{E}}{\partial t},$$

where ϵ_0 and μ_0 are the free space permittivity and permeability, respectively, and $\mu_0\epsilon_0 = c^{-2}$ where c is the speed of light. It leads to the wave equation

$$\nabla^2\mathbf{E} - \frac{1}{c^2}\frac{\partial^2\mathbf{E}}{\partial^2 t} = 0.$$

We start with exploiting the connection between electromagnetic (EM) field in a cavity and the simple harmonic oscillators. Assuming an EM field polarized in the x direction and a perfect empty one-dimensional cavity of length L, the electric field propagating in the z direction can written as a summation over all possible normal modes with frequencies ω_j as

$$\mathbf{E}(z,t) = \sum_j A_j q_j(t)\sin(k_j z)\hat{x}.$$

Here $k_j = \omega_j/c$ is the wave vector of jth mode and q_j is the time-dependent amplitude. Given the vanishing boundary conditions on both ends of the cavity we have $k_j = j\pi/L$, with $j = 1, 2, 3...$, and

$$A_j = \left(\frac{2\omega_j^2}{V\epsilon_0}\right)^{1/2},$$

where V is the cavity volume. This leads to the associated magnetic fields being

$$\mathbf{B}(z,t) = \frac{1}{c^2}\sum_j A_j \frac{\dot{q}_j(t)}{k_j}\cos(k_j z)\hat{y},$$

and the total Hamiltonian being

$$\begin{aligned}\mathcal{H} =& \frac{1}{2}\int dV\left(\epsilon_0 E^2 + \frac{1}{\mu_0}B^2\right)\\ =& \frac{1}{2}\sum_j(\omega_j^2 q_j^2 + p_j^2),\end{aligned}$$

where $p_j = \dot{q}_j$. In analogy to the simple harmonic oscillator with unit mass, it is easy to show q_j and p_j have the dimensions of position and momentum, respectively. By imposing the commutation relation that $[q_i, p_j] = i\hbar\delta_{ij}$, the canonical variables transfer into Hermitian operators and the field is quantized.

It is useful to introduce the dimensionless non-hermitian field operators such that

$$a_j = \sqrt{\frac{1}{2\hbar\omega_j}}(\omega q_j + ip_j),$$
$$a_j^\dagger = \sqrt{\frac{1}{2\hbar\omega_j}}(\omega q_j - ip_j),$$

and $[a_i^\dagger, a_j] = \delta_{i,j}$. The electric field and Hamiltonian then become

$$\mathbf{E} = \frac{E_0}{2}\sum_j \left(ae^{i(kz-\omega t)} + a^\dagger e^{-i(kz-\omega t)}\right),$$
$$\mathcal{H} = \sum_j \hbar\omega_j\left(a_j^\dagger a_j + \frac{1}{2}\right). \tag{1.1}$$

We may now consider three very important kinds of state of the EM field, the photon number or the Fock state, the coherent state, and the squeezed state. For simplicity, we also assume these states are of single-mode. The Fock states $|n\rangle$ are the eigenstates of the Hamiltonian $\mathcal{H}$ with eigenvalue n, where n is the number of photon contained in the field. The photon number operator is given by $N = a^\dagger a$ and

$$N|n\rangle = n|n\rangle,$$
$$|n\rangle = \frac{1}{\sqrt{n!}}\left(a^\dagger\right)^n|0\rangle.$$

The set $\{|n\rangle\}$ constitutes a complete orthonormal basis of the Hilbert space, namely,

$$\langle m|n\rangle = \delta_{mn},$$
$$\sum_{n=0}^{\infty} |n\rangle\langle n| = 1.$$

Given that

$$a|n\rangle = \sqrt{n}|n-1\rangle,$$
$$a^\dagger|n\rangle = \sqrt{n+1}|n\rangle,$$
$$a|0\rangle = 0,$$

a and $a^\dagger$ are known as the annihilation and creation operators, respectively, and $|0\rangle$ is the vacuum state. It is also important to note that $\mathcal{H}|0\rangle = 1/2\hbar\omega$, which is the zero point energy arising from vacuum fluctuations. Photon number states are highly non-classical and are difficult to generate experimentally.

On the other hand, coherent states $|\alpha\rangle$ closely resemble the output states of a coherent laser. They are defined as the eigenstates of the annihilation operator are called coherent states

$$a|\alpha\rangle = \alpha|\alpha\rangle.$$

In the number state basis we have

$$|\alpha\rangle = \ e^{-\frac{|\alpha|^2}{2}} \sum_n \frac{\alpha^n}{\sqrt{n!}}|n\rangle,$$

where the coefficients come from normalization of the coherent states. The average photon number of a coherent state is $\bar{n} = |\alpha|^2$. Alternatively, the coherent states can be generated by applying the displacement operator $D(\alpha)$ to the vacuum state, where

$$D(\alpha) = \ \exp(\alpha a^\dagger - \alpha^* a).$$

Finally we introduce the squeezed states defined as

$$\begin{aligned} |\alpha, \xi\rangle &= D(\alpha)S(\xi)|0\rangle, \\ S(\xi) &= \ \exp\big(\frac{1}{2}(\xi^* a^2 - \xi a^{\dagger 2})\big), \end{aligned}$$

where $S(\xi)$ is the squeezing operator with $\xi = re^{i\theta}$ and r is the squeezing parameter, θ is the squeezing angle. Squeezed state are the eigenstates of the operator $\mu a + \nu a^\dagger$ with $\mu = \cosh r$ and $\nu = e^{i\theta}\sinh r$, such that

$$(\mu a + \nu a^\dagger)|\alpha, \xi\rangle = \ (\alpha \cosh r + \alpha^* e^{i\theta}\sinh r)|\alpha, \xi\rangle.$$

The average number of photon in a squeezed state is

$$\langle S|a^\dagger a|S\rangle = \ |\alpha|^2 + \sinh^2 r.$$

In the limit of $r = 0$ a squeezed state reduces to a coherent state. In the following subsection, we discuss the noise feature of the coherent and squeezed states.

1.1.2 Quantum Noise

According to the Heisenberg Uncertainty Principle (HUP), two observables A and B of a physical system cannot be simultaneously known to arbitrary high precision if they have nonzero commutation relation. Namely,

$$\Delta A \Delta B \geq \frac{1}{2}|\langle [A, B] \rangle|,$$

where $\Delta O = \sqrt{\langle O^2 \rangle - \langle O \rangle^2}$ with $O = A, B$, is the uncertainty of the corresponding observable. For the particular case of a particle, its position x and momentum p must obey the relation such that

$$\Delta x \Delta p \geq \frac{\hbar}{2}.$$

It is then clear that a more accurate determination of the particle's position must be compensated with a less precise value of its momentum, and vice versa. Quantum radiation fields have to obey HUP as well. One of the consequences of this is the quantum noise, *i.e.*, the ever-present quantum fluctuation of the EM field. To show this we introduce yet another set of dimensionless Hermitian operators

$$X_{1j} = \frac{a_j + a_j^\dagger}{2},$$
$$X_{2j} = \frac{a_j - a_j^\dagger}{2i}$$

which describe a pair of quadratures of the electric field. Eq. (1.1) for a single-mode field then reads

$$\mathbf{E} = E_0\big(X_1 \cos(kz - \omega t) + X_2 \sin(kz - \omega t)\big).$$

It is clear that X_1 and X_2 are associated with field amplitudes oscillating out of phase by $\pi/2$. Therefore, the expectation values of this pair of operators constitute a phase space picture

where the feature of states can be easily visualized. In addition, the X_1 and X_2 operators are usually called the amplitude and phase quadrature operators, respectively. They have the commutation relation $[X_1, X_2] = i/2$. This gives rise to the uncertainty relation

$$\Delta X_1 \Delta X_2 \geq \frac{1}{4}.$$

For a coherent state $|\alpha\rangle$, it is easy to see that

$$\langle X_1 \rangle = \frac{1}{2}(\alpha + \alpha^*),$$
$$\langle X_2 \rangle = \frac{1}{2i}(\alpha - \alpha^*),$$

and $\Delta X_1 = \Delta X_2 = 1/2$. Thus a coherent state can be pictured as an error circle of radius 1/2 centered (Re[α],Im[α]) in the phase space (see Figure 1.1.) If consider the time evolution of the state of the radiation field, *i.e.*, $\alpha = |\alpha| \exp(-i\omega t)$, the error circle will rotate clockwise with frequency ω in the phase space. The connection between the phase space picture and the time-dependent-amplitude picture of a field in coherent state is shown in Figure 1.2. It is easy to see that the quantum uncertainties of an electric field in a coherent state do not depend on the phase and that they are equal in the amplitude and phase quadratures. This quantum noise is the well known *shot-noise*, which originates from the discrete nature of photons. It is surprising that this noise exists even when $\alpha = 0$. It is therefore called the vacuum fluctuation and is one of the hallmarks of quantum optical theories.

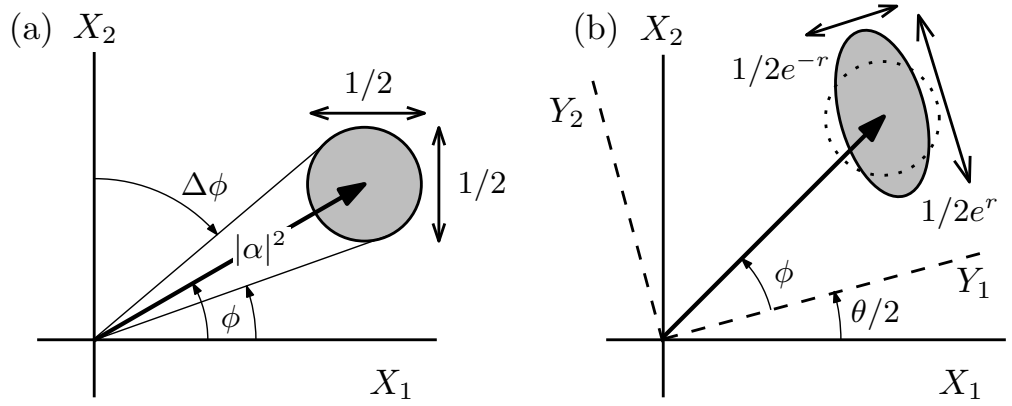

FIGURE 1.1: The phase representation of (a) a coherent state $|\alpha\rangle$ with $\alpha = |\alpha|e^{i\phi}$ and (b) a squeezed version of it, namely, $|\alpha, \xi\rangle = S(\xi)|\alpha\rangle$ with $\xi = re^{i\theta}$.

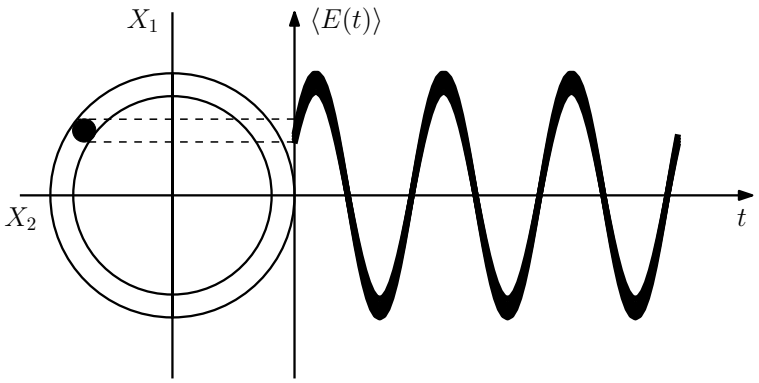

FIGURE 1.2: The size of the error circle of a field in coherent state does not change while revolving in the phase space. The expectation value of the electric field is the projection onto an axis parallel with X_1.

Next we consider a squeezed state $|\alpha, \xi\rangle$ with $\xi = re^{i\theta}$. We first introduce the rotated quadrature operators Y_1, Y_2 such that

$$\begin{pmatrix} Y_1 \\ Y_2 \end{pmatrix} = \begin{pmatrix} \cos\frac{\theta}{2} & \sin\frac{\theta}{2} \\ -\sin\frac{\theta}{2} & \cos\frac{\theta}{2} \end{pmatrix} \begin{pmatrix} X_1 \\ X_2 \end{pmatrix},$$

or equivalently $Y_1 + iY_2 = (X_1 + iX_2)e^{-i\theta/2}$. It is straightforward to show that

$$\begin{aligned} \langle Y_1 + iY_2\rangle &= \alpha e^{-\theta/2}, \\ \Delta Y_1 &= \frac{1}{2}e^{-r}, \\ \Delta Y_2 &= \frac{1}{2}e^{r}. \end{aligned}$$

The phase space picture of such a squeezed state is shown in Figure 1.1. It should be noted that the fluctuations are now both phase (θ) dependent and different in perpendicular quadratures, which is quite different from the case of coherent states. Moreover, a time-dependent visualization of squeezed states is shown in Figure 1.3.

1.2 Quantum Estimation via Optical Interferometry

An estimation theory is required when certain parameters of interest are not directly accessible by measurement, either because of unavoidable noise in the measuring process or due to there being no appropriate observable. Both conditions are fulfilled in the particular case of quantum phase measurement — there is no universally accepted quantum phase operator [4]

and ever-present noise! Throughout this dissertation, we consider quantum optical inteferometry as our measurement scheme and try to extract phase information of the target out of the signals. The target can be the position of a fast moving object or the phase shift caused by some external field. In this section, we first introduce the basic idea of quantum optical inteferometry and the performance of several optical states in an interferometric setup, then we present the Quantum Cramér-Rao Bound (QCRB) as a variant of the HUP. When some detection scheme in quantum interferometry is able to saturate the QCRB, we usually consider this scheme to be optimal. In Chapter 3, for example, we will show that the parity detection is optimal even when phase fluctuation is present.

1.2.1 Quantum Optical Interferometry

A typical Mach-Zehnder interferometer (MZI) is shown in Figure 1.4. Typically passive lossless four-port interferometers can be described using Schwinger notation [5]. First we

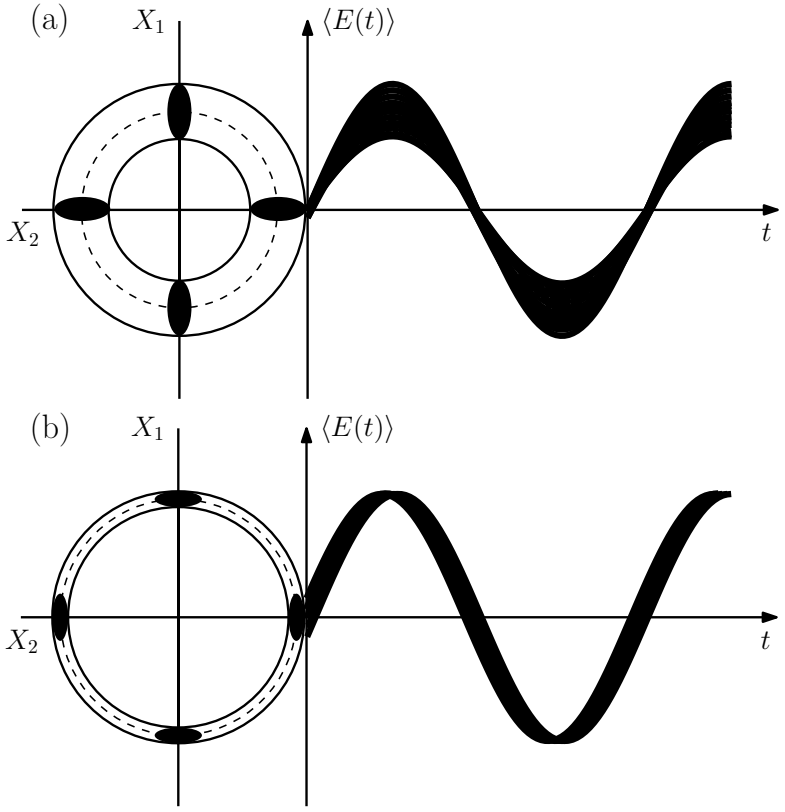

FIGURE 1.3: The phase space representation of a electric field in a squeezed state with (a) initial squeezing in phase quadrature, and (b) initial squeezing in amplitude quadrature.

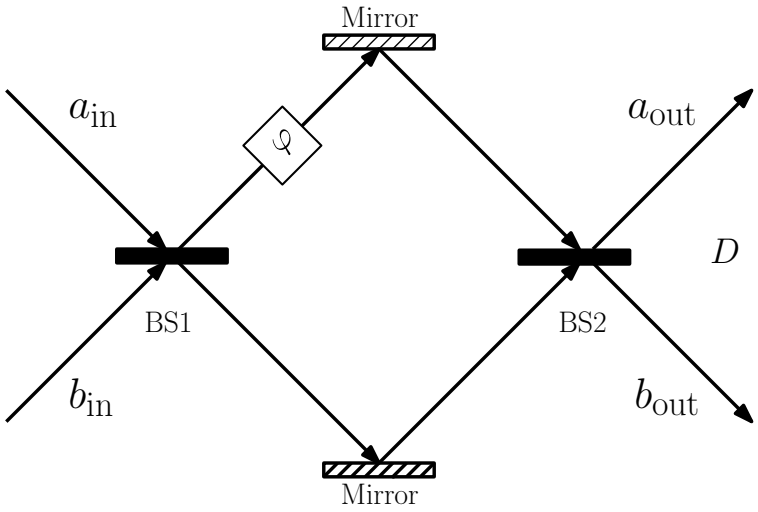

FIGURE 1.4: Schematic of a Mach-Zehnder interferometer. It includes two 50:50 beam splitters, two mirrors and a phase shifter φ, which mimics the unknown phase we want to measure. a and b are the input modes of the MZI while c and d are the output modes. D represents any measurement may be carried out at the output for information extraction.

introduce the angular momentum operators in terms of the two optical modes a and b on one side of the beam splitter (BS)

$$\mathbf{J} = \begin{pmatrix} J_x \\ J_y \\ J_z \end{pmatrix} = \frac{1}{2} \begin{pmatrix} a^\dagger b + b^\dagger a \\ -i(a^\dagger b - b^\dagger a) \\ a^\dagger a - b^\dagger b \end{pmatrix},$$

and $J_0 = (a^\dagger a + b^\dagger b)/2$, which obey $[J_i, J_j] = i\varepsilon_{ijk} J_k$ and $[J_0, J_i] = 0$ $(i = x, y, z)$. Therefore the common eigenstate of J_0 and J_z is the two-mode Fock state

$$|j, \mu\rangle_z = |j + \mu, j - \mu\rangle_{a,b} \tag{1.2}$$

with eigenvalues $j = \langle J_0 \rangle$ and $\mu = \langle J_z \rangle$. Note that the representative Hilbert space is spanned by the complete orthonormal basis $|j, \mu\rangle$ with $\mu \in [-j, j]$. Next, it can be shown that the operation of a BS is given by [6]

$$\mathbf{J}_{\text{out}} = \; e^{i\alpha J_z} e^{i\beta J_y} e^{i\gamma J_z} \mathbf{J}_{\text{in}} e^{-i\gamma J_z} e^{-i\beta J_y} e^{-i\alpha J_z},$$

in the Heisenberg picture, and

$$|\psi_{\text{out}}\rangle = \; e^{-i\alpha J_z} e^{-i\beta J_y} e^{-i\gamma J_z} |\psi_{\text{in}}\rangle$$

in the Schrödinger picture. Here $\alpha,\ \beta$, and γ are the Euler angles parameterizing SU(2) and physically they are related to the transmission and reflectance coefficients. In parallel we may write the BS operation in terms of the input modes $a_{\rm in}, b_{\rm in}$ and the output modes $a_{\rm out}, b_{\rm out}$ as

$$\begin{pmatrix} a_{\rm out} \\ b_{\rm out} \end{pmatrix} = \begin{pmatrix} e^{i(\alpha+\gamma)/2}\cos\frac{\beta}{2} & e^{-i(\alpha-\gamma)/2}\sin\frac{\beta}{2} \\ -e^{i(\alpha-\gamma)/2}\sin\frac{\beta}{2} & e^{-i(\alpha+\gamma)/2}\cos\frac{\beta}{2} \end{pmatrix} \begin{pmatrix} a_{\rm in} \\ b_{\rm in} \end{pmatrix}.$$

For example, in the angular momentum picture, a 50:50 BS causes a $\pm\pi/2$ rotation of the $\mathbf{J}$ vector around the x axis, *i.e.*, $e^{\pm i\pi J_x/2}\mathbf{J}e^{\mp i\pi J_x/2}$; in the field operator language, this amounts to

$$\begin{pmatrix} a_{\rm out} \\ b_{\rm out} \end{pmatrix} = \frac{1}{\sqrt{2}} \begin{pmatrix} 1 & \mp i \\ \mp i & 1 \end{pmatrix} \begin{pmatrix} a_{\rm in} \\ b_{\rm in} \end{pmatrix}.$$

Similarly, the phase shift φ can be understood as a rotation of $\mathbf{J}$ by an angle φ or $a_{\rm out} = a_{\rm in}, b_{\rm out} = e^{i\varphi}b_{\rm in}$.

The effect of the entire MZI then becomes

$$\begin{aligned} U &= e^{i\pi J_x/2}e^{-i\varphi J_z}e^{-i\pi J_x/2} \\ &= e^{-i\varphi J_y}, \end{aligned} \tag{1.3}$$

which is a φ rotation around y axis. Accordingly we have

$$\begin{pmatrix} a_{\rm out} \\ b_{\rm out} \end{pmatrix} = \begin{pmatrix} \cos\frac{\varphi}{2} & -\sin\frac{\varphi}{2} \\ \sin\frac{\varphi}{2} & \cos\frac{\varphi}{2} \end{pmatrix} \begin{pmatrix} a_{\rm in} \\ b_{\rm in} \end{pmatrix}.$$

By assuming $D = a_{\rm out}^\dagger a_{\rm out} - b_{\rm out}^\dagger b_{\rm out} = 2J_{z,\rm out}$, which is the detected intensity difference, we may calculate the output signal as

$$\begin{aligned} \langle J_{z,\rm out}\rangle &= \langle\psi_{\rm in}|J_{z,\rm out}|\psi_{\rm in}\rangle \\ &= \langle\psi_{\rm in}|U^\dagger J_z U|\psi_{\rm in}\rangle \\ &= -\sin\varphi\langle\psi_{\rm in}|J_x|\psi_{\rm in}\rangle + \cos\varphi\langle\psi_{\rm in}|J_z|\psi_{\rm in}\rangle \end{aligned}$$

and

$$\begin{aligned}\langle J_{z,\text{out}}^2\rangle &= \langle\psi_{\text{in}}|U^\dagger J_z^2 U|\psi_{\text{in}}\rangle \\ &= \sin^2\varphi\langle\psi_{\text{in}}|J_x^2|\psi_{\text{in}}\rangle - \sin\varphi\cos\varphi\langle\psi_{\text{in}}|J_xJ_z + J_zJ_x|\psi_{\text{in}}\rangle + \cos^2\varphi\langle\psi_{\text{in}}|J_z^2|\psi_{\text{in}}\rangle.\end{aligned}$$

The minimum detectable phase shift then can be obtain by [7]

$$\delta\varphi = \frac{\Delta J_{z,\text{out}}}{|\partial\langle J_{z,\text{out}}\rangle/\partial\varphi|}. \tag{1.4}$$

We now apply this formalism to coherent states. Consider the coherent input state $|\alpha,0\rangle = |\alpha\rangle_a|0\rangle_b$. It is easy to show that

$$\begin{aligned}\langle J_x\rangle &= \langle J_xJ_z\rangle = \langle J_zJ_x\rangle = 0, \\ \langle J_z\rangle &= 1/2|\alpha|^2, \\ \langle J_x^2\rangle &= 1/4|\alpha|^2, \\ \langle J_z^2\rangle &= 1/4|\alpha|^4.\end{aligned}$$

Then

$$\delta\varphi = \frac{1}{\sqrt{\bar{n}}|\sin\varphi|},$$

where $\bar{n} = |\alpha|^2$ is the average number of photon in the state. The $1/\sqrt{\bar{n}}$ dependence of phase uncertainty is another manifestation of the *shot-noise* and is called the *shot-noise limit* (SNL). This agrees with the HUP which demands that $\Delta\varphi\Delta N \geq 1$ and $\Delta N = \sqrt{\bar{n}}$ for a coherent state (see Figure 1.1.) SNL is the standard noise level that all noise levels are compared against. Any state leading to a sensitivity level lower than the SNL is called super sensitive.

1.2.2 Fisher Information and Cramér-Rao Bound

Classical Fisher Information (CFI) leads to the ultimate precision in estimating an known parameter φ when a particular measurement $X(x)$ is given (x is one realization of the X.)

By assuming the information-carrying system is in a state ρ_φ we have the likelihood function [8, 9]

$$p(x|\varphi) = \mathrm{Tr}[X(x)\rho_\varphi]. \tag{1.5}$$

From this probability distribution we can estimate the value of φ by using an estimator function $\varphi_{\mathrm{est}}(x)$. The whole problem then reduces to finding the optimal estimator function that minimizes the uncertainty in the estimation process, *i.e.*, minimizes

$$(\Delta\varphi)^2 = \int p(x|\varphi)(\varphi_{\mathrm{est}} - \varphi)^2 dx.$$

We assume the estimator is unbiased such that

$$\int (\varphi_{\mathrm{est}}(x) - \varphi)p(x|\varphi)dx = 0.$$

Differentiating both sides of the equation with respect to φ gives

$$\int (\varphi_{\mathrm{est}}(x) - \varphi)p(x|\varphi)\left(\frac{\partial \ln p(x|\varphi)}{\partial\varphi}\right)dx = 1,$$

where the 1 on the right hand side comes from the normalization of the probability density function. Now the Cauchy-Schwarz inequality leads to

$$\int (\varphi_{\mathrm{est}}(x) - \varphi)^2 p(x|\varphi)dx \int p(x|\varphi)\left(\frac{\partial \ln p(x|\varphi)}{\partial\varphi}\right)^2 dx \geq 1.$$

By defining the classical Fisher information

$$\begin{aligned} F &= \int p(x|\varphi)\left(\frac{\partial \ln p(x|\varphi)}{\partial\varphi}\right)^2 dx \\ &= \int \frac{1}{p(x|\varphi)}\left(\frac{\partial p(x|\varphi)}{\partial\varphi}\right)^2 dx, \end{aligned} \tag{1.6}$$

we reach

$$(\Delta\varphi)^2 \geq \frac{1}{F},$$

where $\sqrt{1/F}$ is called the classical Cramér-Rao bound (CCRB). If ν independent measurements are conducted, the central limit theorem enhances this precision to

$$(\Delta\varphi)^2 \geq \frac{1}{\nu F}.$$

It should be emphasized that the CCRB is the bound that applies to all unbiased estimators, φ_{est}, for a fixed probability distribution $p(x|\varphi)$ [10]. Recall in Eq. 1.5 that $p(x|\varphi)$ depends on the particular choice of measurement X (a POVM). Therefore, the next logical step is to look for the ultimate limit that bounds all possible measurements. This generalization of CCRB was first proposed by Braunstein and Caves in 1994 and was beautifully proved in that same paper [10].

The new bound is called the quantum Cramér-Rao bound (QCRB) and is inversely proportional to the quantum Fisher information (QFI), F_{Q} [11, 10, 12], which is independent of the measurement procedure. Recall that any detection scheme that saturates this bound is considered to be optimal. To quantify the QFI of a state ρ_φ, we first introduce the symmetric logarithmic derivative, L, which is a self-adjoint operator satisfying the equation

$$\frac{\partial\rho_\varphi}{\partial\varphi} = \frac{1}{2}(L\rho_\varphi + \rho_\varphi L). \tag{1.7}$$

In the eigenbasis of ρ_φ its elements satisfy

$$\frac{\lambda_i + \lambda_j}{2}\langle i|L|j\rangle = \langle i|\frac{\partial\rho_\varphi}{\partial\varphi}|j\rangle,$$

for all i and j, where λ_i and $|i\rangle$ are the eigenvalue and the corresponding eigenvector of ρ_φ. For any Hermitian operator O and $\rho'_\varphi = \partial\rho_\varphi/\partial\varphi$, we have [9]

$$\text{Tr}[O\rho'_\varphi] = \text{Re}(\text{Tr}[\rho_\varphi OL]).$$

By identifying that $\partial p(x|\varphi)/\partial\varphi = \mathrm{Tr}[X\rho'_\varphi]$, Eq. (1.6) becomes

$$\begin{aligned}
F &= \int \frac{(\mathrm{Tr}[X\rho'_\varphi])^2}{\mathrm{Tr}[X\rho_\varphi]}dx \\
&= \int \frac{(\mathrm{Re}(\mathrm{Tr}[\rho_\varphi XL]))^2}{\mathrm{Tr}[X\rho_\varphi]}dx \\
&\leq \int \frac{|\mathrm{Tr}[\rho_\varphi XL]|^2}{\mathrm{Tr}[X\rho_\varphi]}dx \\
&= \int \left|\mathrm{Tr}\left[\frac{\sqrt{\rho_\varphi X}}{\mathrm{Tr}[X\rho_\varphi]}\sqrt{X}L\sqrt{\rho_\varphi}\right]\right|^2 dx \\
&\leq \int \mathrm{Tr}[XL\rho_\varphi L]dx \\
&= \mathrm{Tr}[\rho_\varphi L^2] \\
&= F_Q,
\end{aligned}$$

where the second inequality is from the Schwarz inequality $|\mathrm{Tr}[A^\dagger B]|^2 \leq \mathrm{Tr}[A^\dagger A]\mathrm{Tr}[B^\dagger B]$ with $A = \sqrt{\rho_\varphi X}, B = \sqrt{X}L\sqrt{\rho_\varphi}$ and the second last equality is a result of the normal condition of the measurement operator $\int X(x)dx = 1$. Therefore the uncertainty of estimating the unknown parameter, φ, is given by

$$(\Delta\varphi)^2 \geq \frac{1}{\nu F} \geq \frac{1}{\nu F_Q},$$

where $1/\sqrt{F_Q}$ is the QCRB.

Finally we consider the estimation sensitivity of extracting the phase information from, for example, a phase shifted pure state. For a MZI, it is equivalent to having a pure state $|\psi\rangle$ inside the interferometer right after the first BS. The generator of the phase shift is given by $\exp(-i\varphi J_z)$ as shown in Eq. (1.3). Denoting D as the measurement operator, we have

$$\frac{\partial}{\partial\varphi}\langle D\rangle = -i\big(\langle\psi|DJ_z|\psi\rangle - \langle\psi|J_zD|\psi\rangle\big). \tag{1.8}$$

Assuming $\langle D\rangle = 0$ and $\langle J_z\rangle = 0$, we then have $\Delta D^2 = \langle\psi|DD|\psi\rangle = ||\psi_D\rangle|^2$ and similarly $\Delta J_z^2 = ||\psi_{J_z}\rangle|^2$. The Cauchy-Schwarz inequality then states that

$$\Delta D^2\Delta J_z^2 \geq |\langle\psi_D|\psi_{J_z}\rangle|^2.$$

By rewriting the r.h.s. of Eq. (1.8) in terms of $|\psi_D\rangle$ and $|\psi_{J_z}\rangle$, it is easy to show that

$$\Delta D^2 \Delta J_z^2 \geq \frac{1}{4}\left|\frac{\partial\langle D\rangle}{\partial\varphi}\right|^2.$$

Given

$$\delta\varphi^2 = \frac{\Delta D^2}{|\partial\langle D\rangle/\partial\varphi|^2},$$

we have

$$\delta\varphi^2 \geq \frac{1}{4\Delta J_z^2}. \tag{1.9}$$

Since J_z represents the photon number difference between the two paths inside the MZI and this difference cannot be larger than the total photon number N, Eq. (1.9) enforces a limit on the phase uncertainty given by

$$\delta\varphi_{\mathrm{HL}}^2 = \frac{1}{N^2}.$$

This is the so-called *Heisenberg limit*, which is a $1/\sqrt{N}$ enhancement over the SNL. We therefore conclude that to beat the classical noise limit, one should employ optical states with a large photon number difference inside the MZI. One extreme example is the N00N state whose photon number difference is equal to the total photon number. Interestingly, the famous scheme of mixing a squeezed vacuum with coherent light at the input [13] effectively generates a combination of N00N states inside the interferometer [14].

1.3 The Atom-Field Interaction

Dirac's quantum theory of radiation also marked the beginning of the quantum mechanical treatment of the atom-field interaction. The coupling energy was originally introduced into the total Hamiltonian as a perturbation term. Later, with the invention of high-intensity and tunable laser light, strong near-resonant field-atom interactions became possible. The Rabi model is a semi-classical model that correctly describes atom-field interactions when the radiation field is treated classically, while the Jaynes-Cummings model applies to the

cases where both atom and field are quantized. In this section we derive a general atom-field interaction Hamiltonian under appropriate approximations. The application of this Hamiltonian to both the Rabi and the JC models of a four-level atomic system will be discussed in Chapter 6.

The system we study here is the interaction between a classical EM field and a simple atom composed of an electron in the Coulomb field of a stationary nucleus suited at $\mathbf{r_0}$. The field is characterized by the potentials $\mathbf{A}(\mathbf{r},t)$ and $U(\mathbf{r},t)$, which includes both the Coulomb field of the nucleus and the external field interacting with the atom. The total Hamiltonian is given by

$$\mathcal{H} = \frac{1}{2m}(\mathbf{p} - q\mathbf{A}(\mathbf{r},t))^2 + qU(\mathbf{r},t).$$

In the Göppert-Mayer gauge [15], which is obtained from the Coulomb gauge by the gauge transformation

$$\chi(\mathbf{r},t) = -(\mathbf{r}-\mathbf{r}_0)\cdot\mathbf{A}_\perp(\mathbf{r}_0,t),$$

we have

$$\mathcal{H} = \frac{1}{2m}(\mathbf{p} - q\mathbf{A}'(\mathbf{r},t))^2 + V_{\text{coul}}(\mathbf{r}) + q(\mathbf{r}-\mathbf{r}_0)\cdot\frac{\partial}{\partial t}\mathbf{A}_\perp(\mathbf{r}_0,t), \tag{1.10}$$

where $V_{\text{coul}}(\mathbf{r}) = qU_{\text{coul}}(\mathbf{r})$. Here the Göppert-Mayer potentials are

$$\begin{aligned}\mathbf{A}'(\mathbf{r},t)) &= \mathbf{A}_\perp(\mathbf{r},t)) - \mathbf{A}_\perp(\mathbf{r}_0,t)), \\ U'(\mathbf{r},t)) &= U_{\text{coul}}(\mathbf{r}) - (\mathbf{r}-\mathbf{r}_0)\cdot\frac{\partial}{\partial t}\mathbf{A}_\perp(\mathbf{r}_0,t).\end{aligned} \tag{1.11}$$

Given $\mathbf{E}(\mathbf{r},t) = -\partial/\partial t\mathbf{A}_\perp(\mathbf{r},t)$ and dipole operator $\mathbf{d} = q(\mathbf{r}-\mathbf{r}_0)$, Eq. (1.10) becomes

$$\mathcal{H} = \frac{1}{2m}(\mathbf{p} - q\mathbf{A}'(\mathbf{r},t))^2 + V_{\text{coul}}(\mathbf{r}) - \mathbf{d}\cdot\mathbf{E}(\mathbf{r}_0,t). \tag{1.12}$$

In the optical regime, the wavelength of the radiation field is much longer than the size of the atom, therefore we may adopt the long-wavelength approximation $\mathbf{A}_\perp(\mathbf{r},t) \approx \mathbf{A}_\perp(\mathbf{r}_0,t)$.

In this case Eq. (1.12) requires that $\mathbf{A}'(\mathbf{r},t)) = 0$ and the final form of the Hamiltonian becomes

$$\mathcal{H} = \mathcal{H}_0 + \mathcal{H}_1, \tag{1.13}$$

$$\mathcal{H}_0 = \frac{\mathbf{p}^2}{2m} + V_{\text{coul}}(\mathbf{r}), \tag{1.14}$$

$$\mathcal{H}_1 = -\mathbf{d}\cdot\mathbf{E}(\mathbf{r}_0,t). \tag{1.15}$$

This Hamiltonian is known as the electric dipole Hamiltonian, and it fully determines the dynamics of the electron.

Chapter 2
Quantum Metrology under Photon Loss

In this chapter we discuss the metrological properties of the symmetric number-path entangled states and their performances under photon loss. We first introduce the maximally number-path entangled state, *i.e.*, the N00N state, followed by the discussion on the improved version of it—the M&M′ state. It is shown that although N00N states of light is capable of reaching the Heisenberg limit with certain detection schemes, they are very vulnerable under photon loss. The M&M′ states are specifically designed to overcome this disadvantage of N00N states and are robust against photon loss.

In this chapter we calculate both the visibility and sensitivity of the phase signal from the interferometer with M&M′ being the input state. On one hand, the signal from parity detection can be negative therefore the ordinary definition of visibility is not applicable. We define a 'relative visibility' to solve this problem. A promising goal of this chapter is to provide a strategy for choosing the symmetric number-path entangled state that optimizes either visibility or sensitivity for a given loss.[1]

2.1 The N00N and M&M′ States

The application of quantum states of light has long been proposed to achieve greater resolution, and sensitivity than what is possible classically [16, 13]. A maximally number-path entangled state is a superposition of all photons in one path with none in the other, and vice versa. These states are known as N00N states and defined as

$$|N :: 0\rangle_{a,b} = \frac{1}{\sqrt{2}}(|N,0\rangle_{a,b} + |0,N\rangle_{a,b}), \tag{2.1}$$

[1]Part of this chapter previously appeared as Kebei Jiang, Chase J. Brignac, Yi Weng, Moochan B. Kim, Hwang Lee, and Jonathan P. Dowling, *Strategies for choosing path-entangled number states for optimal robust quantum-optical metrology in the presence of loss*, Phys. Rev. A, **86**, 013826 (2012). It is reprinted by permission of the American Physical Society (APS). See the permission letter in Appendix B.

where a and b indicate the two paths of a two-mode interferometer. On one hand, it is straightforward to see that a N00N state is a number-path entangled state, as a measurement of photon number on one path will collapse that on the other path. Mathematically, it cannot be written as a product state [17] and strongly violates some Bell-type inequalities [18]. On the other hand, even though no standard measure of multipartite entanglement is universally accepted, N00N states are usually defined to be maximally entangled for its apparent resemblance to maximally entangled bipartite states. In addition, N00N states *are mathematically equivalent to the Greenberger-Horne-Zeilinger (GHZ) states, both of which are the $J = \pm N/2$ subspace of the N pseudo-spin Hilbert space.* For this reason, we adopt the Schwinger notation discussed in Sec. 1.2.1 in later calculations. Readers who are interested in the equivalence between optical and atomic spectroscopy are referred to Ref. [19] and [20].

The N00N state enjoys a fine reputation in quantum metrology and lithography because of its ability to generate multifold phase-dependent signals, which in turn leads to super-resolution (always possible) and super-sensitivity (tricky with loss, see Ref. [21].) Super-resolution and sensitivity refer to a better performance than those of a coherent state $|\alpha\rangle$. Here we present a brief comparison between these two kinds of states under a phase shift and demonstrate the superiority of the N00N state in phase estimation. The unitary evolution associated with a phase shifter is given by $U(\varphi) \equiv \exp(i\varphi n)$, with n being the photon number operator. Assuming the phase shifter in suited on path b of the interferometer and it is easy to show that

$$\begin{aligned} U(\varphi)\left|\frac{\alpha}{\sqrt{2}}, \frac{i\alpha}{\sqrt{2}}\right\rangle_{a,b} &= \left|\frac{\alpha}{\sqrt{2}}, \frac{i\alpha\exp(i\varphi)}{\sqrt{2}}\right\rangle_{a,b}, \\ U(\varphi)|N::0\rangle &= \frac{1}{\sqrt{2}}(|N,0\rangle_{a,b} + \exp(iN\varphi)|0,N\rangle_{a,b}), \end{aligned} \tag{2.2}$$

where $|\alpha/\sqrt{2}, i\alpha/\sqrt{2}\rangle_{a,b}$ is the state inside the interferometer given the input state is $|\alpha, 0\rangle_{a,b}$. It is obvious that the N00N states evolves in phase N-times faster than the coherent state. Consider a intensity-difference measurement of the MZI with coherent state input, we have

the signal $I(\varphi) = I_0 \cos(\varphi)$ [22], where $I_0 \propto \bar{n} = |\alpha|^2$ is the amplitude of the signal. On the other hand, by using a proper detecting scheme for N00N state input, the signal varies as $I(\varphi) = I_0 \cos(N\varphi)$ and this is the origin of all the improvement mentioned before. Both cases are shown in Figure 2.1, where same wavelength λ and amplitude (*i.e.* $\bar{n} = N$) are assumed. The rapid oscillation of N00N state signal can be understood as if a 'big' single classical photon (a Bose condensate of the ensemble of N photons) with effective de Broglie wavelength λ/N is used [23]. As a result, the Rayleigh diffraction limit of λ is beaten by a factor of N and hence super-resolution. In the case of no loss, the slope at the horizontal axis crossing of the N00N state signal is N times steeper than that of the coherent state signal, which gives rise to a $\sqrt{N}$ enhancement in sensitivity—super-sensitivity.

However, N00N states tend to decohere easily when photons are lost from the system, which will be shown in the following sections. This makes N00N states unusable in real life, where loss is almost always present [24, 25, 26, 27, 28]. Therefore in 2008, Huver *et al.* proposed a class of generalized Fock states where decoy photons are introduced to the N00N state in both arms of a two-mode interferometer [29]. These are called M&M′ states and they are

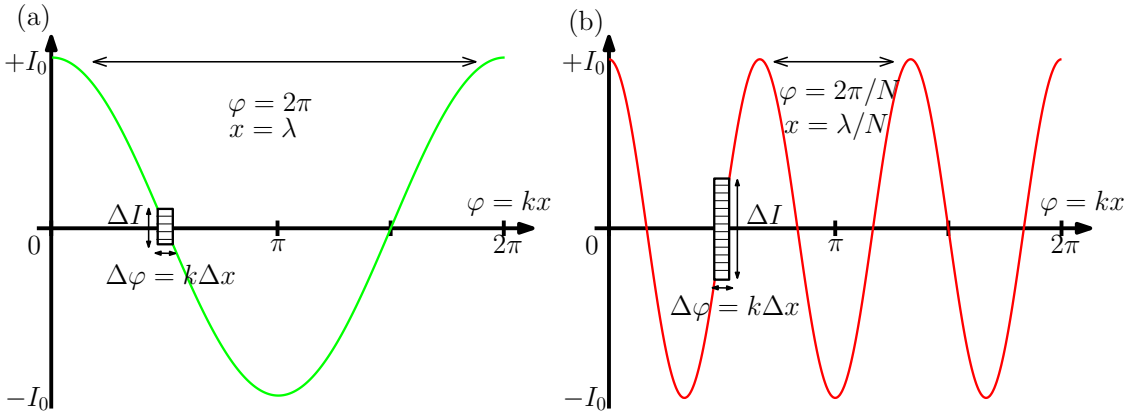

FIGURE 2.1: The comparison of the detection signals of MZI with its input as (a), a coherent state and (b), a N00N state, both with wavelength λ. The N00N state signal oscillates N times faster than the coherent state signal and its maximum slope is N times as steep, where $N = 3$ in this case. Improvement of the N00N state over the coherent state leads to super-resolution and super-sensitivity, respectively. One interpretation is that the ensemble of N photons can be deemed as a Bose condensate with an effective de Broglie wavelength of λ/N.

denoted as $|m :: m'\rangle$ and

$$|m :: m'\rangle_{a,b} = \frac{1}{\sqrt{2}}(|m, m'\rangle_{a,b} + |m', m\rangle_{a,b}). \tag{2.3}$$

Here a and b are the two paths of the interferometer and again it is easy to show that M&M$'$ states are entangled. Such states can be produced by post-selecting on the output of a pair of optical parametric oscillators [30]. It was discovered that M&M$'$ states have better metrological performance over N00N states in the presence of photon loss (see the heuristic explanation at the end of Huver's paper from 2008). In the following sections, we locate the best performing m and m' under certain fixed loss, where the photon number difference ($\Delta m = m - m'$) between the two arms in the initial state is set to be N for easy comparison between the N00N state and the M&M$'$ state (However, in the following calculation, we treat the N00N state as a special case of the M&M$'$ state with $m' = 0$ and only differentiate them when comparison is necessary.)

2.2 Density Matrix

To calculate the density matrix we start with the classical MZI as shown in Figure 2.2, where the source and the detector are represented by their respective boxes. Similar to the approach in Ref. [26, 31, 32], the loss in the interferometer is modeled by adding fictitious beam splitters. Notice that it will not change the density matrix of the field if the beam splitter is placed before the phase shifter. However, the full density matrix of the field and environment together will be different for different orders of the beam splitter and phase shifter. By defining $U_\phi = e^{in_{b'}\phi}$ and $U_{\mathrm{BS}} = \exp\left[i\pi\left(b'^{\dagger}v_{b'} + \mathrm{h.c.}\right)/4\right]$, it amounts to prove that $U_\phi^\dagger U_{\mathrm{BS}}^\dagger \rho U_{\mathrm{BS}} U_\phi \neq U_{\mathrm{BS}}^\dagger U_\phi^\dagger \rho U_\phi U_{\mathrm{BS}}$, which is obvious in a Bloch sphere picture. As a matter of fact, the configuration of these two optical elements can be parametrized and optimized for noisy quantum metrology. Readers may refer to Ref. [33] for more detail.

The wave function for the M&M$'$ input state at stage I is defined in Eq. 2.3 and without loss of generality, we assume $\Delta m = m - m'$ is positive. Then the phase shifter introduces a

phase shift φ on arm b so that the state at stage II becomes (see Figure 2.2)

$$|\Psi\rangle_{\rm II} = \frac{1}{\sqrt{2}}\left(e^{im'\varphi}|m,m'\rangle_{a',b'} + e^{im\varphi}|m',m\rangle_{a',b'}\right) \tag{2.4}$$
$$= \alpha|m,m'\rangle_{a',b'} + \beta|m',m\rangle_{a',b'},$$

where $\alpha = e^{im'\varphi}/\sqrt{2}$ and $\beta = e^{im\varphi}/\sqrt{2}$. We can see that because of the different number of photons being phase-shifted on arm b, the two paths accumulated different phase shifts and thus provide the possibility of interference upon detection.

The mode transformation caused by the beam splitter is given by [4]

$$a = t_a^* a' + r_a^* v_a',$$
$$b = t_b^* b' + r_b^* v_b', \tag{2.5}$$

where $t_i = \sqrt{T_i}\exp(i\varphi_i)$ and $r_i = \sqrt{R_i}\exp(i\psi_i)$ $(i = a, b)$ are the complex transmission and reflectance coefficients for modes a and b, and $T_i + R_i = 1$. By tracing out the vacuum modes

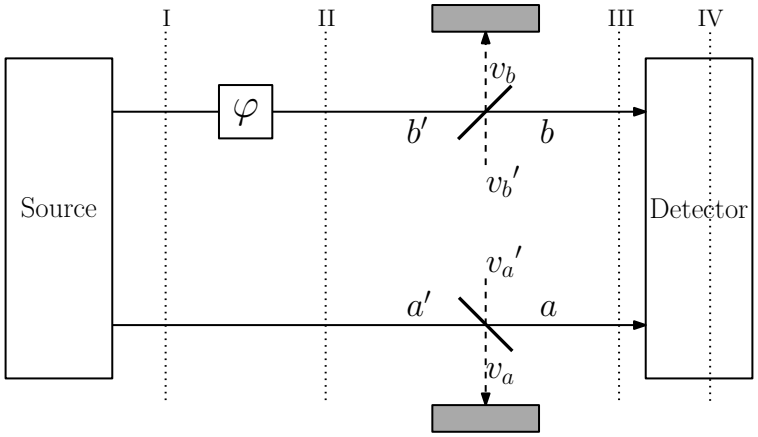

FIGURE 2.2: Schematic diagram of a simplified Mach-Zehnder interferometer with the modes a and b for the M&M$'$ states as the input. The original source and detector are 'hidden' in the respective boxes. Two fictitious BS' are introduced to mimic the loss of photon (or the damping of the TMHO) into the environment. The upper beam passes through a phase-shifter φ, and the acquired phase depends on the number of difference of photons $\Delta m = m - m'$. Transformed parity detection is used as the detection scheme at both of the two modes at stage III inside the interferometer.

on both paths, we have a density matrix ρ_{ab} that corresponds to the output field as

$$\begin{aligned}
\rho_{ab} &= \mathrm{Tr}_{v_a,v_b}[|\Psi\rangle_{\mathrm{III}\ \mathrm{III}}\langle\Psi|] \\
&= \sum_{k=0}^{m}\sum_{k'=0}^{m'}\big(|\alpha|^2 d_1|k,k'\rangle_{a,b\ a,b}\langle k,k'| \\
&\qquad +|\beta|^2 d_2|k',k\rangle_{a,b\ a,b}\langle k',k|\big) \\
&\quad +\sum_{k=0}^{m'}\sum_{k'=0}^{m'}(\alpha\beta^* d_3|\Delta m+k,k'\rangle_{a,b\ a,b}\langle k,\Delta m+k'| \\
&\qquad +\alpha^*\beta d_4|k',\Delta m+k\rangle_{a,b\ a,b}\langle\Delta m+k',k|)\,,
\end{aligned} \tag{2.6}$$

where coefficients $d_i (i=1,2,3,4)$ are defined as

$$\begin{aligned}
d_1(k,k') &= \binom{m}{k}\binom{m'}{k'}|T_a|^k|R_a|^{m-k}|T_b|^{k'}|R_b|^{m'-k'}, \\
d_2(k,k') &= \binom{m}{k}\binom{m'}{k'}|T_a|^{k'}|R_a|^{m'-k'}|T_b|^{k}|R_b|^{m-k}, \\
d_3(k,k') &= \binom{m}{\Delta m+k}^{\frac{1}{2}}\binom{m}{\Delta m+k'}^{\frac{1}{2}}\binom{m'}{k}^{\frac{1}{2}}\binom{m'}{k'}^{\frac{1}{2}}, \\
&\quad \times T_a^{\frac{1}{2}(\Delta m+2k)}R_a^{m'-k}T_b^{\frac{1}{2}(\Delta m+2k')}R_b^{m'-k'} \\
d_4(k,k') &= \binom{m}{\Delta m+k}^{\frac{1}{2}}\binom{m}{\Delta m+k'}^{\frac{1}{2}}\binom{m'}{k}^{\frac{1}{2}}\binom{m'}{k'}^{\frac{1}{2}} \\
&\quad \times T_a^{\frac{1}{2}(\Delta m+2k')}R_a^{m'-k'}T_b^{\frac{1}{2}(\Delta m+2k)}R_b^{m'-k}.
\end{aligned} \tag{2.7}$$

An equivalent way to describe the loss process is by using the Kraus operators and readers may refer to Ref. [34, 35, 36] and references therein.

2.3 Parity Detection and Its Signal

In addition to state preparation, achieving super-resolution (rapidly oscillating fringes that are commonly associated with beating the Rayleigh limit in the specific context of coherent, interferometric, optical lithography[37, 38, 39, 40])[2] and super-sensitivity (beating the shot-

[2]There are really two common uses of 'Rayleigh limit' in optics. There is most common, the minimum angular resolution of an imaging system to distinguish two points, which is not what we mean here. Second most common, used in the optical coherent lithography community, is the ability to write interference fringes at less than half the spacing of the imaging wavelength, which is directly related to the ability to generate the effect of higher frequency oscillations from lower frequency light. That is the use found in Ref. [40].

noise limit [41]) usually requires detection schemes with particular properties. For example, it is straightforward to show that the intensity-differencing signal of a N00N state input is phase independent and not applicable for phase estimation [22]. Therefore in this chapter, we use the parity operator, which is originally proposed by Bollinger *et al.* in the context of trapped ions [42] and later adopted for optical interferometry by Gerry [43], as our detection scheme. The parity operator is assigned a parity of $+1$ if the measured number of photon is even and a parity of -1 if odd, and is shown to reach the Heisenberg-limited sensitivity when combined with lossless N00N states [43, 44, 45]. It can be expressed as $\Pi = \exp(i\pi n)$ in the number basis or $\Pi = \exp(i\pi(J_0 - J_z))$ in Schwinger notation [6, 46, 47]. Readers who are interested in more details about the parity operator and its application in quantum optical metrology may refer to Ref. [22].

We start with $\Pi = (-1)^{J_0 - J_z}$ at stage IV and transform it back to stage III as Q. The generator for the beam splitter transformation is J_x, and we have

$$\begin{aligned} \mathrm{Q} &= \exp(-i\frac{\pi}{2}J_x)\Pi\exp(i\frac{\pi}{2}J_x) \\ &= \exp(i\pi J_0)\exp(i\pi J_y). \end{aligned} \tag{2.8}$$

Following Ref. [47], the parity operator inside the interferometer in number basis becomes

$$\mathrm{Q} = \sum_{n=0}^{N_{\mathrm{tot}}} i^n \sum_{k=0}^{n} (-1)^k |k, n-k\rangle\langle n-k, k|, \tag{2.9}$$

where the first summation is over all possible photon loss, and N_{tot} is the total number of photons without loss. It is easy to check that $\mathrm{Q}^2 = 1$.

With both the density matrix and the parity operator obtained at stage III, it is straightforward to calculate the expectation value of the parity operator for an M&M$'$ state as

$$\begin{aligned} \langle \mathrm{Q} \rangle &= \mathrm{Tr}(\mathrm{Q}\rho) \\ &= K_1 + K_2 \cos \Delta m\varphi, \end{aligned} \tag{2.10}$$

where K_1 and K_2 are defined as

$$\begin{aligned} K_1 &= \sum_{k=0}^{m'} (d_1(k,k) + d_2(k,k)) \\ &= \left(R_a^{m'} R_b^m + R_a^m R_b^{m'} \right) \\ &\quad \times {}_2F_1(-m, -m'; 1; \frac{T_a T_b}{R_a R_b}), \end{aligned} \tag{2.11}$$

$$\begin{aligned} K_2 &= \sum_{k=0}^{m'} (d_3(k,k) + d_4(k,k)) \\ &= R_a^{m'} R_b^{m'} T_a^{\frac{\Delta m}{2}} T_b^{\frac{\Delta m}{2}} \binom{m}{\Delta m} \\ &\quad \times {}_2F_1(-m', -m'; 1 + \Delta m; \frac{T_a T_b}{R_a R_b}). \end{aligned} \tag{2.12}$$

Here ${}_2F_1(a, b; c; z) = \sum_{n=0}^{\infty} \frac{(a)_n (b)_n}{(c)_n} \frac{z^n}{n!}$ is the ordinary hypergeometric function [48]. The Pochhammer symbol within are defined to be

$$(x)_n = \begin{cases} 1, & \text{if } n = 0; \\ x(x+1)\dots(x+n-1), & \text{if } n > 0, \end{cases}$$

which truncates the infinite summation in the hypergeometric function at $n = m'$. Note Eqs. (2.10) and (2.12) reduce to the N00N state result if $m = N$ and $m' = 0$.

For later calculations and analysis in this chapter we use loss rates $L_i \equiv 1 - T_i$ $(i = a, b)$ instead of the transmission rates T_i following traditional notation in metrology.

2.4 Visibility

We use the parity operator for detection and its expectation value can be negative in certain regions of parameter space. To quantify the degree of measured phase information we need a proper definition of visibility. From Eq. (2.12) we can see that K_1 decreases and K_2 increases as the loss rate decreases. Hence, K_1 and K_2 have a range from 0 to 1 and so it is reasonable to define the measured signal as

$$S = \frac{K_2}{K_1 + K_2} \tag{2.13}$$

which is always positive. We can then define a visibility related to the highest phase information degree (*i.e.* strongest signal) as

$$V(L_a, L_b) = \frac{S(L_a, L_b)}{S(0,0)} \tag{2.14}$$

with $S(0,0)$ being the signal without loss. This relative visibility has a value from 0 to 1.

2.4.1 Visibility for General Cases

In Figure 2.3, we plot visibility as a function of loss rate. We see that, for M&M$'$ states with a large total number of photons, the visibility changes rapidly at high or low loss but slowly at mild loss.

To clearly see the effect of photon number on visibility, we assume $L_a = L_b = L$ and plot visibility as a function of L for different states in Figure 2.4. We observe M&M$'$ states exhibit a lower visibility than corresponding N00N states for loss rates lower than 50%, and exhibit higher visibility for loss greater than 50%. Each row has a fixed photon number difference and the total number of photons increases from left to right. We can see that with increasing total number of photons, the distance between the M&M$'$ state and the N00N state curves increases. Each column has fixed m' and the photon number difference increases from top to bottom. We can see that as the photon number difference increases, the distance between the M&M$'$ state and the N00N state curves decreases.

Therefore, to obtain the best visibility, under photon loss less than 50%, N00N states should be used with N as large as possible, *i.e.* the bottom row of the figure; for loss greater than 50%, M&M$'$ states should be used with as many photons as possible while keeping photon number difference to a minimum, *i.e.* the upper right corner of the figure.

Mathematically, the above results can be explained by expanding the visibility of any M&M$'$ state around $L = 1/2$ as

$$V|_{L\approx\frac{1}{2}} = \frac{1}{2} + \frac{\Delta m^2}{m+m'}(L - \frac{1}{2}) + O[(L - \frac{1}{2})^2]. \tag{2.15}$$

Note that any N00N state is just the corresponding M&M′ state with $m' = 0$, therefore it gives the steepest slope around $L = 1/2$ in every case. Physically speaking, this result is different from Ref. [29], where N00N states always have lower visibility than M&M′ states under any loss. The reason for this discrepancy is that all off-diagonal terms of the density matrix are included in Ref. [29] while here the parity operator collects only part of the off-diagonal terms, making the amplitude of the resultant signal smaller.

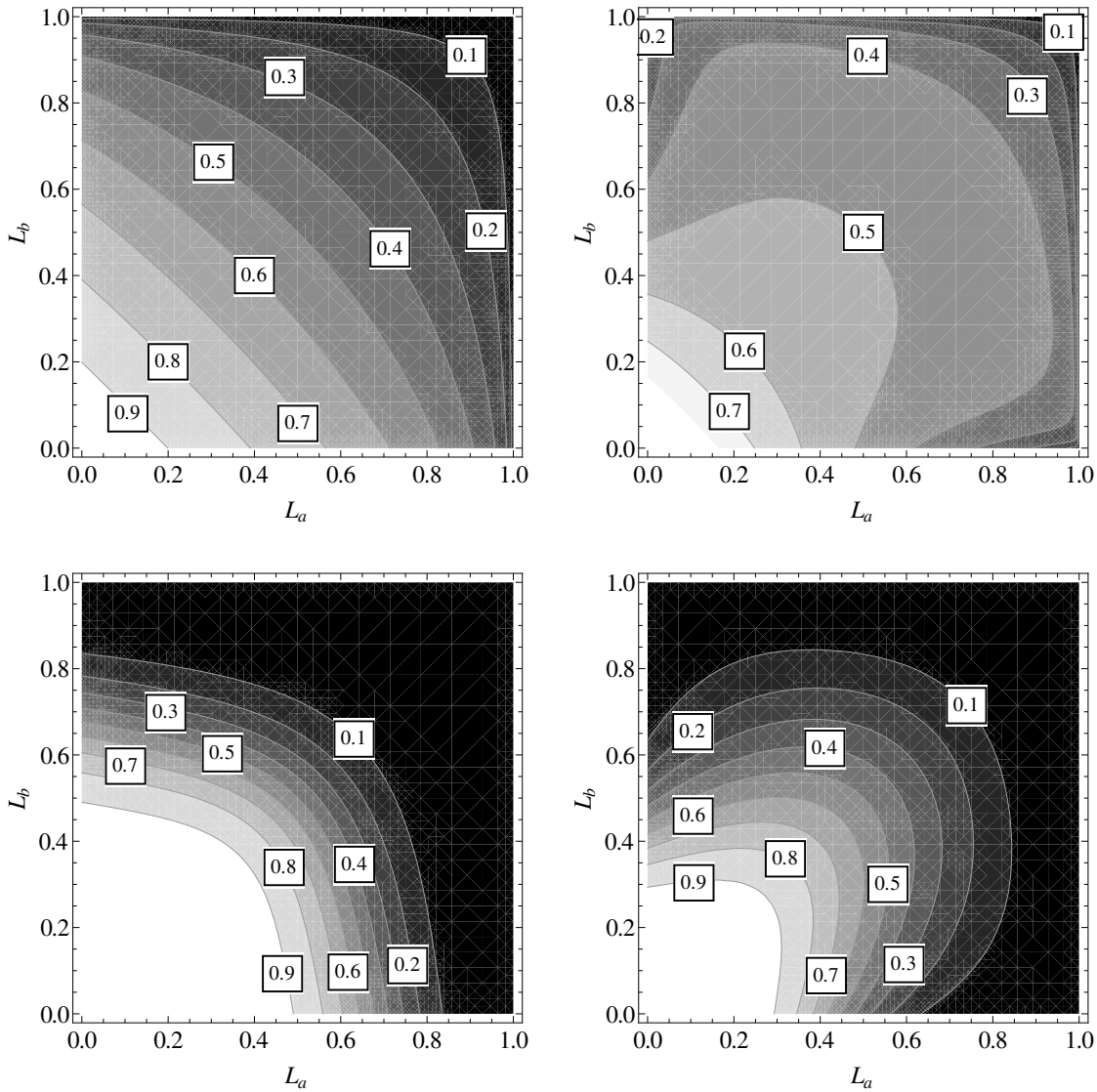

FIGURE 2.3: From left to right, top to bottom. Visibility for M&M′ states with $\Delta m = 1$ ($|1 :: 0\rangle$ and $|3 :: 2\rangle$) and M&M′ states with $\Delta m = 4$ ($|4 :: 0\rangle$ and $|6 :: 2\rangle$), as a function of loss rates (dimensionless) in both arms of two-mode interferometer, L_a and L_b, respectively. Contour lines represent the values of the visibility.

2.4.2 Visibility for Extreme Cases

For situations with almost no loss, *i.e.* the loss rate $L \to 0$, the visibility function Eq. (2.14) can be expanded as

$$V|_{L\approx 0} = \binom{m}{\Delta m} L^{\Delta m} + O[L^{\Delta m+1}], \tag{2.16}$$

which explains the behaviors of visibility curves around $L = 0$ for different Δm in Figure 2.4. Similarly, visibility for very lossy situations can be easily expanded as

$$V|_{L\approx 1} = 1 - \binom{m}{\Delta m}(1-L)^{\Delta m} + O[(1-L)^{\Delta m+1}] \tag{2.17}$$

because of the symmetry of the system. Another example for symmetry is that for 50% loss the visibilities are calculated to be exactly one half for all m and m' value, which is the consequence of Eq. (2.15).

2.5 Sensitivity

Another important quantity in quantum optical metrology is the precision, or sensitivity, of the phase measurement. The Heisenberg limit for any M&M$'$ state under loss rate L_a and L_b should be $1/\widetilde{N}$ while the corresponding shot-noise limit is $1/\sqrt{\widetilde{N}}$ where $\widetilde{N} = (m+m')(1 - L_a/2 - L_b/2)$ is the effective number of transmitted photons. Therefore we usually compare the performance of different states with the same total number of photons. However, in order to keep the same resolving power we fix the photon number difference Δm between two arms of the two-mode interferometer in this section.

2.5.1 Sensitivity for General Loss

Sensitivity calculated from Eqs. (1.4), (2.10) and (2.12) can be expanded as

$$\delta\varphi = \begin{cases} \frac{1}{\Delta m} + \frac{(m+m')}{\Delta m}\csc(\Delta m\varphi)L + O[L^2], \\ \text{if } \Delta m \text{ is even;} \\ \frac{1}{\Delta m} + \frac{(m+m')}{\Delta m}\sec(\Delta m\varphi)L + O[L^2], \\ \text{if } \Delta m \text{ is odd.} \end{cases} \tag{2.18}$$

It is then trivial to show that at the limit of $L \to 0$, M&M$'$ states and corresponding N00N states approach minimal phase sensitivity $\delta\varphi_{min} = 1/\Delta m$ at optimal phase shifts

$$\varphi_{op} = \begin{cases} \frac{(2n-1)}{2}\frac{\pi}{\Delta m}, & \text{if } \Delta m \text{ is even;} \\ n\frac{\pi}{\Delta m}, & \text{if } \Delta m \text{ is odd, } n = 1, 2, \ldots. \end{cases} \tag{2.19}$$

For a M&M$'$ state or N00N state to be able to beat the shot-noise limit under parity detection, we should have

$$\Delta m > \sqrt{m + m'}. \tag{2.20}$$

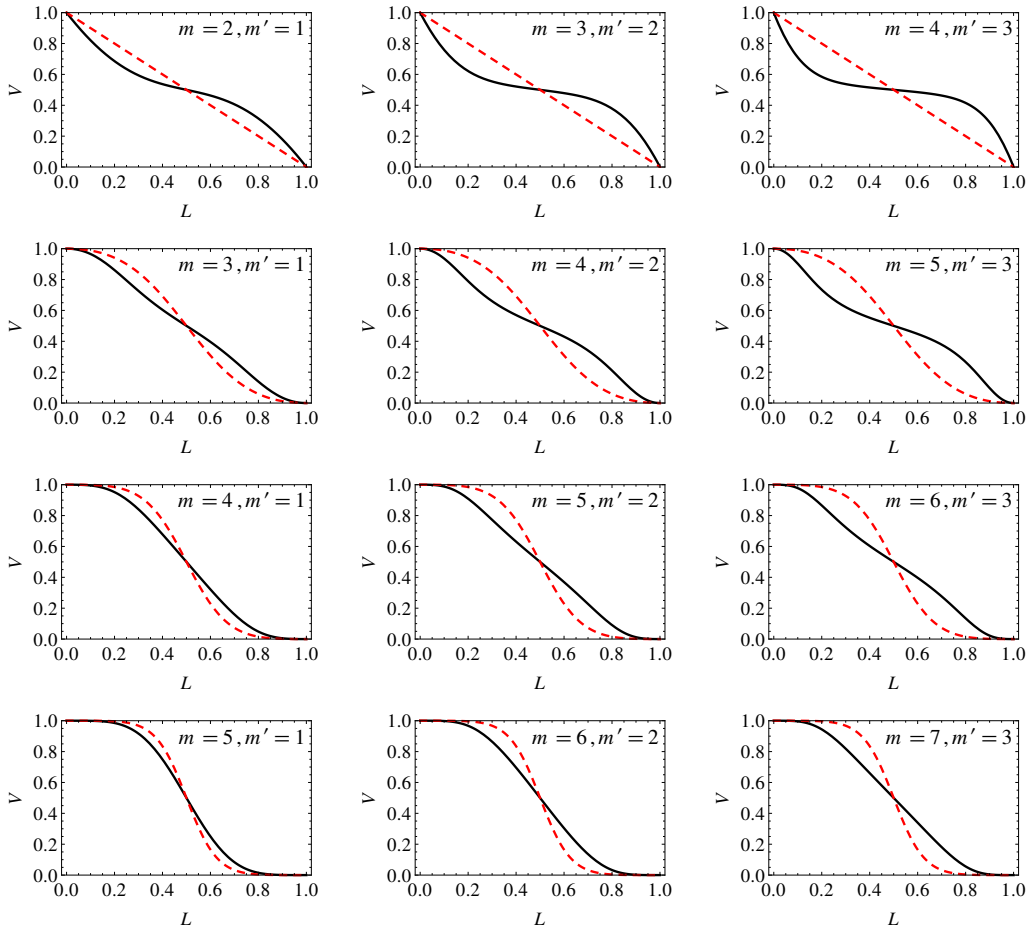

FIGURE 2.4: Visibility for M&M$'$ states (solid black curves) as a function of the dimensionless loss rate L in both arms of the two-mode interferometer. Each row has a fixed photon number difference and the total number of photons increases from left to right; each column has a fixed m' and photon number difference increases from top to bottom. The dashed red curves represent the corresponding N00N states with $N = \Delta m$.

To meet the above criteria, here we choose $\Delta m = 6$ and $\varphi = \pi/(2\Delta m)$, assuming $L_a = L_b$ for practical purposes. In Figure 2.5 it can be seen that $|6 :: 0\rangle$ and $|8 :: 2\rangle$ give sub-shot-noise performances for loss less than about 10%, and $|6 :: 0\rangle$ gives higher sensitivity than $|8 :: 2\rangle$ up to 25% loss; for loss greater than 25%, $|6 :: 0\rangle$ is outperformed by $|8 :: 2\rangle$ but both are worse than shot-noise.

2.5.2 Sensitivity for Smaller Loss

Often we are more interested in low-loss regions where the sensitivity of M&M′ states and N00N states are comparable to the shot-noise limit. Figure 2.6 shows that the sensitivity of $|6 :: 0\rangle$ and $|8 :: 2\rangle$ are noticeably worse than the respective shot-noise limit under moderate loss (35% in this case). Here $|8 :: 2\rangle$ turns out to be more robust than $|6 :: 0\rangle$ as predicted in Ref. [29].

This robustness, however, does not apply to situations where the loss is even smaller. In Figure 2.7 we show the sensitivity of $|6 :: 0\rangle$ and $|8 :: 2\rangle$ under 5% loss. Here both states give higher sensitivity than the shot-noise limit and N00N is the best of all. In contrast, the result in Ref. [29] shows that, with a certain detection operator, M&M′ states always give

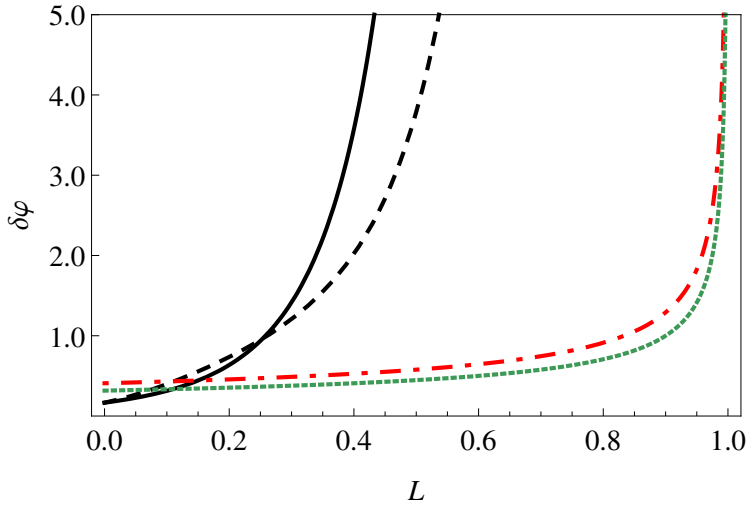

FIGURE 2.5: Sensitivity for M&M′ states as a function of the dimensionless loss rate L in both arms of a two-mode interferometer. Solid black curve corresponds to $|6 :: 0\rangle$, dot-dashed red curve to $1/\sqrt{6(1-L)}$, dashed black curve to $|8 :: 2\rangle$ and dotted red curve to $1/\sqrt{10(1-L)}$. Parity detection using M&M′ states is worse than shot-noise under around 10% loss.

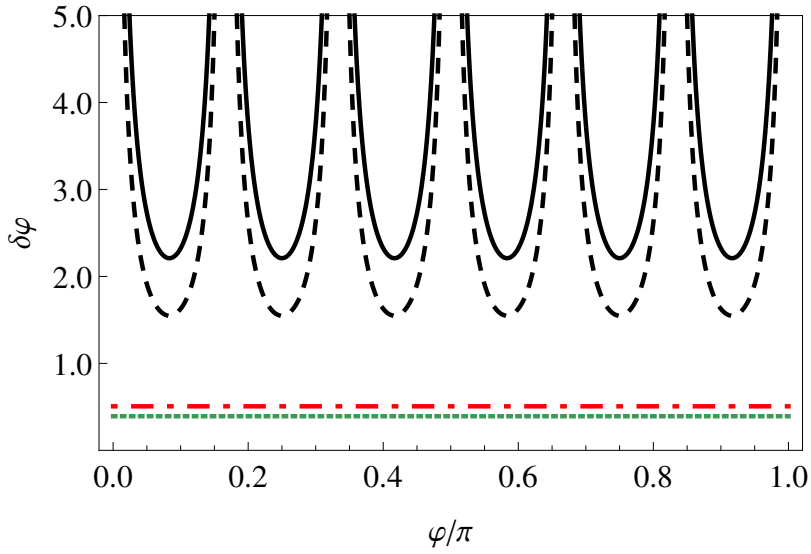

FIGURE 2.6: Sensitivity of M&M′ states as a function of phase shift φ (measured in unit of π) from a two-mode interferometer under 35% loss. Solid black curve corresponds to $|6::0\rangle$, dot-dashed red line to $1/\sqrt{6\times(1-0.35)}$, dashed black curve to $|8::2\rangle$ and dotted red line to $1/\sqrt{10\times(1-0.35)}$. While the sensitivity of M&M′ and N00N states are worse than respective shot-noise limit, M&M′ is more robust as expected.

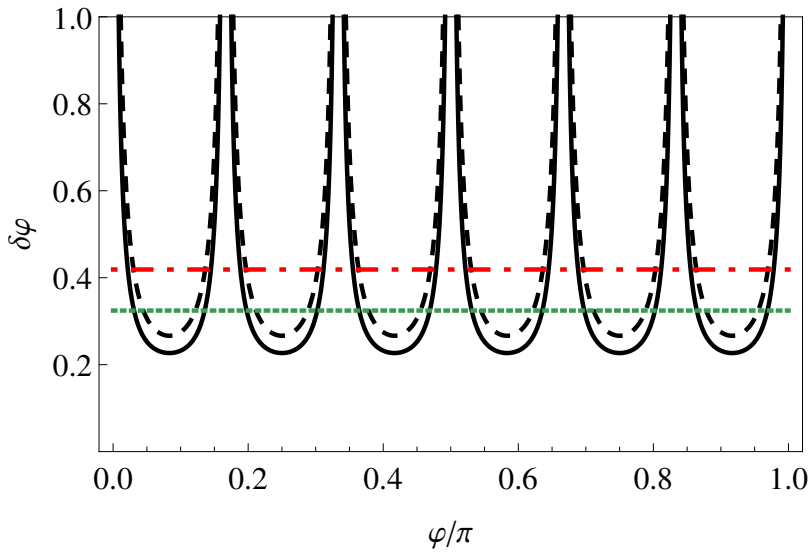

FIGURE 2.7: Sensitivity of M&M′ states as a function of phase shift φ (measured in unit of π) from a two-mode interferometer under 5% loss. Solid black curve corresponds to $|6::0\rangle$, dot-dashed red line to $1/\sqrt{6\times(1-0.05)}$, dashed black curve to $|8::2\rangle$ and dotted red line to $1/\sqrt{10\times(1-0.05)}$. While the sensitivity of M&M′ and N00N states are better than their respective shot-noise limits, N00N is more robust, which is unexpected.

better sensitivity than using N00N states and the shot-noise limit no matter how high the loss. This discrepancy indicates that the parity operator is not the optimal detector that always favors M&M′ states (see conclusion for more discussion.)

2.6 Conclusion

We calculate the visibility and sensitivity of a phase-carrying signal by using M&M′ states with parity detection in a lossy environment. In our calculation, we take the photon number difference between the two arms of the two-mode interferometer Δm to be fixed to maintain the desired resolving power. Since visibility is not well defined for signal using parity detection, we use a visibility which is measured against signal without loss. To have high visibility, one should use N00N states with large N (when loss is low) and M&M′ states with large $m+m'$ but small Δm (when loss is high). Considering only sensitivity, our calculation shows that N00N states with large N or M&M′ states with large Δm under low loss are capable of performing with sub-shot-noise limit precision.

It is worthwhile to mention two points. First, modeling loss with a single fictitious beam splitter is sufficient for practical purposes. If one reverses the order of the phase shifter and the beam splitter in Figure 2.2, the same density matrix will be obtained as proved in Ref. [35, 36]. This also means our model is equivalent to a continuous loss model. Second, Ref. [29] uses a detection operator that is carefully chosen so that it sums up all off-diagonal terms of the density matrix and provides sub-shot-noise sensitivity. Meanwhile the parity operator collects some of the diagonal and off-diagonal terms. The inclusion of diagonal terms may reduce the signal size and therefore visibility or sensitivity of phase information. However, such an operator in Ref. [29] is yet to be produced in a lab setting. On contrary, a lot of effort has been made to realize parity measurements. A straightforward parity measurement relies on high precision photon number-resolving detection at single-photon level, which has been demonstrated experimentally in near-infrared region [49]. Alternative parity detection setups without number-resolving detectors have been proposed as well [50, 51].

Chapter 3
Quantum Metrology under Phase Fluctuation

In the previous chapter we discussed the performances of symmetric number-path entangled states, both the N00N state and the M&M′ state, under different photon losses. In real life applications such as quantum radar, phase fluctuation due to different noise sources can further aggravate the phase-sensitivity by adding significant noise to the phase φ to be estimated or detected. For instance, when one considers propagation of the entangled states over distances of kilometers, through say the atmosphere, then atmosphere turbulence becomes an issue as it can cause uncontrollable noise in the phase. In this sense, phase-fluctuation stands as the most detrimental for phase estimation, rendering the quantum metrological advantage for achieving super-sensitivity and super-resolution useless. It is therefore necessary to investigate the impacts of such random phase-fluctuations on the phase-sensitivity of entangled states. We consider both the M&M′ and N00N states, and show how the phase-sensitivity and visibility of the phase signal are affected by added phase-fluctuations caused by turbulence noise.[1]

Here we first derive the master equation for a two-mode harmonic oscillator (TMHO) under pure phase fluctuation and apply it to the M&M′ state in presence of the turbulence noise. In particular, we study the parity detection [43] and calculate the lower bound of the phase-fluctuated sensitivity. It is shown that the M&M′ state, which is more robust against photon loss than the N00N state, performs equally well when subject to phase fluctuations. At the end, we calculate the QCRB of our dephasing system, which gives the ultimate limit

[1]Sections 3.3 and 3.4 previously appeared as Bhaskar Roy Bardhan, Kebei Jiang, and Jonathan P. Dowling, *Effects of phase fluctuations on phase sensitivity and visibility of path-entangled photon Fock states*, Phys. Rev. A, **88**, 023857 (2013). Permission of using it in this dissertation has been granted by the principal author.

to the precision of the phase measurement, to show that the parity detection for both of the states presents an optimal detection strategy in the sensitivity of phase estimation.

3.1 TMHO under Pure Dephasing

3.1.1 Derivation of a General Master Equation

Following Ref. [52, 53] , we adopt the *System+Reservoir* model to deal with the dephasing of our TMHO. By TMHO, we can think of the two paths of a interferometer where each path represents a possible mode of the electromagnetic field. For instance, a N00N state of field would be deemed as 'N excitations shared by a TMHO'. Throughout this derivation we set $\hbar = 1$. We have Table 3.1 for our mathematical model. Notice that in general the system density matrix $\rho(t)$ and reservoir density matrix R_t are not separable because of the interaction between S and R. Instead we have $\rho(t) = \mathrm{Tr}_R(\chi(t))$.

First of all, to get rid of the rapid oscillating terms in the Hamiltonian, *i.e.*, $H_S + H_R$, we transform into Interaction picture by doing $\tilde{O}(t) = e^{i(H_S+H_R)t}O(t)e^{-i(H_S+H_R)t}$, where $O(t)$ is the operator in Schrödinger picture and $\tilde{O}(t)$ is in the Interaction picture. We then follow Heisenberg Equation of Motion and write down

$$\dot{\tilde{\chi}}(t) = -i\left[\tilde{H}_{SR}(t), \tilde{\chi}(t)\right]. \tag{3.1}$$

This can be integrated formally as

$$\tilde{\chi}(t) = \chi(0) - i\int_0^t dt'\left[\tilde{H}_{SR}(t'), \tilde{\chi}(t')\right]. \tag{3.2}$$

Substituting for $\tilde{\chi(t)}$ in Eq. (3.1) we have

$$\dot{\tilde{\chi}}(t) = -i\left[\tilde{H}_{SR}(t), \tilde{\chi}(0)\right] - \int_0^t dt'\left[\tilde{H}_{SR}(t), \left[\tilde{H}_{SR}(t'), \tilde{\chi}(t')\right]\right]. \tag{3.3}$$

TABLE 3.1: The mathematical model of the TMHO system

	System (S)	reservoir (R)	Composite (S⊗R)
Density Matrix	$\rho(t) = Tr_R(\chi(t))$	R_t	$\chi(t)$
Hamiltonian	H_S	H_R	$H_S + H_R + H_{SR}$

Notice the t and t' in the integral on the right hand side.

By tracing over the reservoir D.O.F. on both sides of Eq. (3.3) and assuming that the interaction between the system and the reservoir starts at $t = 0$, *i.e.*, they are not entangled when $t \leq 0$, we have therefore $\tilde{\chi}(0) = \chi(0) = \tilde{\rho}(0)\tilde{R}_0 = \rho(0)R_0$, which can be readily seen if one takes $t = 0$ in the Interaction Transformation, and we are left with

$$\dot{\tilde{\rho}}(t) = -i\tilde{\rho}(0)\mathrm{Tr}_R\left\{\left[\tilde{H}_{SR}(t), \tilde{R}_0\right]\right\} - \int_0^t dt'\mathrm{Tr}_R\left\{\left[\tilde{H}_{SR}(t), \left[\tilde{H}_{SR}(t'), \tilde{\chi}(t')\right]\right]\right\}. \tag{3.4}$$

If we further assume that the reservoir operators coupling to the system S have zero mean in state $\tilde{R}_0$ (whose physical meaning will be discussed later), then $\mathrm{Tr}_R\left\{\left[\tilde{H}_{SR}(t), \tilde{R}_0\right]\right\} = 0$. The E.O.M. of the density matrix of system S becomes

$$\dot{\tilde{\rho}}(t) = -\int_0^t dt'\mathrm{Tr}_R\left\{\left[\tilde{H}_{SR}(t), \left[\tilde{H}_{SR}(t'), \tilde{\chi}(t')\right]\right]\right\}. \tag{3.5}$$

At this point, we need to introduce two major approximations:

- **Born Approximation**—H_{SR} **is small**. We assume the interaction between the system and reservoir is quite small, so that $\tilde{\chi}(t)$ should be very little deviated from the *separable state* $\tilde{\rho}(t)\tilde{R}_t$; moreover, since R is much bigger than S, it is reasonable to assume $\tilde{R}_t \approx \tilde{R}_0$ and then $\tilde{\chi}(t) = \tilde{\rho}(t)\tilde{R}_0 + O(\tilde{H}_{SR})$, therefore Eq. (3.5) becomes

$$\dot{\tilde{\rho}}(t) = -\int_0^t dt'\mathrm{Tr}_R\left\{\left[\tilde{H}_{SR}(t), \left[\tilde{H}_{SR}(t'), \tilde{\rho}(t')\tilde{R}_0\right]\right]\right\}. \tag{3.6}$$

  From the commutator in Eq. (3.5), it is easy to see $O(\tilde{H}_{SR})$ leads to terms higher than second order in H_{SR} which can be ignored.

- **Markov Approximation**—$\rho(t)$ **has no memory**. Eq. (3.5) shows that the density matrix of the system $\rho(t)$ depends on all the history from the moment when it starts interacting with the reservoir. However, the system S does not affect itself directly but interacts with the reservoir R at t and the updated R later changes S again at $t + \Delta t$. In our case, since the R is much bigger than S, it will be changed very little

by S and 'forgets' about this change way before (*i.e.*, $\ll \Delta t$) it interacts with S again. As a result, the system S will have to 'forget' about the history as well.[2] Therefore, $\tilde{\rho}(t') \approx \tilde{\rho}(t)$ and finally we have the general Master Equation as

$$\dot{\tilde{\rho}}(t) = -\int_0^t dt' \mathrm{Tr}_R \left\{ \left[\tilde{H}_{SR}(t), \left[\tilde{H}_{SR}(t'), \tilde{\rho}(t)\tilde{R}_0 \right] \right] \right\}. \tag{3.7}$$

To sum up, in Born-Approximation, we write the total state of the system and the reservoir as a separable state; in Markov-Approximation, we separate the state of the system $\tilde{\rho}(t)$ from its history. Now we have a Integro-Differential equation of $\tilde{\rho}(t)$ which can be solved.

3.1.2 TMHO under Pure Dephasing

Given Eq. (3.7) as the general Master Equation, we are now in the position to specify our system. For a single frequency TMHO with mode a and b, we have $H_S = \omega_0(a^\dagger a + b^\dagger b) = \omega_0(n_a + n_b)$ and $H_R = \sum_j \omega_j r_j^\dagger r_j$, where r_j is the annihilation operator in reservoir mode j. Now we need to write down the interaction Hamiltonian H_{SR} carefully.

(a) In general, we associate s_i with operators in the system S and γ_j with operators in the reservoir R, and assume

$$H_{SR} = \sum_{\alpha=a,b} s_\alpha \gamma_\alpha. \tag{3.8}$$

It is easy to see that $\tilde{H}_{SR} = \sum_\alpha \tilde{s}_\alpha \tilde{\gamma}_\alpha$ because of the commutation relations. To specify the s_α and γ_α in our case, we need more physics insight.

(b) For pure phase-fluctuation or dephasing (elastic collision), no energy is exchanged between S and R so that there will be no $a^\dagger r$ or $ar^\dagger$ terms in H_{SR}. Therefore we should have

$$H_{SR} = \sum_{i,j} \kappa_{i,j}^a a^\dagger a r_i^\dagger r_j + \sum_{i,j} \kappa_{i,j}^b b^\dagger b r_i^\dagger r_j \tag{3.9}$$

[2] We may think of a two-level atom interacts with the vacuum. The vacuum has a full range spectrum and therefore (Fourier Transform) has a correlation time $t = 0$, whose time scale is much smaller than the evolution time of the atom.

where $\kappa^{\alpha}_{i,j}$ with $\alpha = a, b$ is the coupling strength between HO mode α with vacuum mode i and j. By comparing Eqs. (3.8) and (3.9), we have

$$s_a = a^\dagger a, \;\; s_b = b^\dagger b; \tag{3.10}$$

$$\text{and} \;\; \gamma_a = \sum_{i,j} \kappa^a_{i,j} r_i^\dagger r_j, \;\; \gamma_b = \sum_{i,j} \kappa^b_{i,j} r_i^\dagger r_j. \tag{3.11}$$

(c) It is easy to see $\tilde{s}_{a,b} = s_{a,b}$ since $[s_{a,b}, H_S] = [s_{a,b}, H_R] = 0$. However,

$$\begin{aligned}
\tilde{\gamma}_\alpha(t) &= e^{iH_R t}\gamma_\alpha e^{-iH_R t} \\
&= \sum_{i,j} \kappa^\alpha_{i,j} \exp\left(i\sum_k \omega_k r_k^\dagger r_k t\right) r_i^\dagger r_j \exp\left(-i\sum_{k'} \omega_{k'} r_{k'}^\dagger r_{k'} t\right) \\
&= \sum_{i,j} \kappa^\alpha_{i,j} \exp\left(i\omega_i r_i^\dagger r_i t + i\omega_j r_j^\dagger r_j t\right) r_i^\dagger r_j \exp\left(-i\omega_i r_i^\dagger r_i t - i\omega_j r_j^\dagger r_j t\right) \\
&= \sum_{i,j} \kappa^\alpha_{i,j} r_i^\dagger r_j e^{i(\omega_i - \omega_j)t}; \qquad (3.12)
\end{aligned}$$

$$\text{and} \quad \tilde{H}_{SR}(t) = \sum_{i,j} \kappa^a_{i,j} a^\dagger a r_i^\dagger r_j e^{i(\omega_i-\omega_j)t} + \sum_{i,j} \kappa^b_{i,j} b^\dagger b r_i^\dagger r_j e^{i(\omega_i-\omega_j)t}. \tag{3.13}$$

From Eqs. (3.7) and (3.9), we have

$$\begin{aligned}
\dot{\tilde{\rho}}(t) &= -\int_0^t dt' \mathrm{Tr}_R \left\{ \left[\sum_{\alpha'=a,b} s_{\alpha'}\tilde{\gamma}_{\alpha'}(t), \left[\sum_{\alpha=a,b} s_\alpha \tilde{\gamma}_\alpha(t'), \tilde{\rho}(t)\tilde{R}_0 \right] \right] \right\} \\
&= -\int_0^t dt' \mathrm{Tr}_R \left\{ \sum_{\alpha,\alpha'} \left[s_{\alpha'}\tilde{\gamma}_{\alpha'}(t), \left[s_\alpha \tilde{\gamma}_\alpha(t'), \tilde{\rho}(t)\tilde{R}_0 \right] \right] \right\} \\
&= -\sum_{\alpha,\alpha'} \int_0^t dt' \mathrm{Tr}_R \Big\{ s_{\alpha'}\tilde{\gamma}_{\alpha'}(t) s_\alpha \tilde{\gamma}_\alpha(t') \tilde{\rho}(t)\tilde{R}_0 - s_{\alpha'}\tilde{\gamma}_{\alpha'}(t)\tilde{\rho}(t)\tilde{R}_0 s_\alpha \tilde{\gamma}_\alpha(t') \\
&\qquad - s_\alpha \tilde{\gamma}_\alpha(t')\tilde{\rho}(t)\tilde{R}_0 s_{\alpha'}\tilde{\gamma}_{\alpha'}(t) + \tilde{\rho}(t)\tilde{R}_0 s_\alpha \tilde{\gamma}_\alpha(t') s_{\alpha'}\tilde{\gamma}_{\alpha'}(t) \Big\}. \qquad (3.14)
\end{aligned}$$

Consider terms like $\mathrm{Tr}_R\left\{\tilde{\gamma}_\alpha(t')\tilde{R}_0\tilde{\gamma}_{\alpha'}(t)\right\} = \mathrm{Tr}_R\left\{\tilde{\gamma}_\alpha(t')\tilde{\gamma}_{\alpha'}(t)\tilde{R}_0\right\} = \langle\tilde{\gamma}_\alpha(t')\tilde{\gamma}_{\alpha'}(t)\rangle_{\tilde{R}_0}$. In Ref. [52] and [54], it is assumed that $\langle\tilde{\gamma}_\alpha(t')\tilde{\gamma}_{\alpha'}(t)\rangle_{\tilde{R}_0} = \gamma_\alpha\delta_{\alpha,\alpha'}\delta(t-t')$, where γ_α should be understood as the phase-fluctuating rate of HO mode α, to reduce the number of terms in the Master Equation. The $\delta_{\alpha,\alpha'}$ assumption amounts to rewriting reservoir Hamiltonian

as

$$\begin{aligned} H_R &= H_{R_a} + H_{R_b} \\ &= \sum_i \omega_i^a (r_i^a)^\dagger r_i^a + \sum_i \omega_i^b (r_i^b)^\dagger r_i^b \end{aligned} \tag{3.15}$$

and Interaction Hamiltonian as

$$\begin{aligned} \tilde{H}_{SR}(t) &= \tilde{H}_{SR_a}(t) + \tilde{H}_{SR_b}(t) \\ &= \sum_{i,j} \kappa_{i,j}^a a^\dagger a (r_i^a)^\dagger r_j^a e^{i(\omega_i - \omega_j)t} + \sum_{i,j} \kappa_{i,j}^b b^\dagger b (r_i^b)^\dagger r_j^b e^{i(\omega_i - \omega_j)t}, \end{aligned} \tag{3.16}$$

where $\kappa_{i,j}^\alpha$ is the interaction strength between HO mode α and reservoir mode r_i^α and r_j^α. Physically, this is equivalent to assume that the part of reservoir interacting with HO mode a is independent of the part interacting with HO mode b, and their correlation always vanishes. We adopt this assumption here and Eq. (3.14) becomes

$$\begin{aligned} \dot{\tilde{\rho}}(t) &= -\sum_{\alpha,\alpha'} \int_0^t dt' \left(s_{\alpha'} s_\alpha \tilde{\rho}(t) - s_{\alpha'} \tilde{\rho}(t) s_\alpha - s_\alpha \tilde{\rho}(t) s_{\alpha'} + \tilde{\rho}(t) s_\alpha s_{\alpha'} \right) \gamma_\alpha \delta_{\alpha,\alpha'} \delta(t - t') \\ &= -\sum_{\alpha=a,b} \gamma_\alpha \left(s_\alpha s_\alpha \tilde{\rho}(t) - s_\alpha \tilde{\rho}(t) s_\alpha - s_\alpha \tilde{\rho}(t) s_\alpha + \tilde{\rho}(t) s_\alpha s_\alpha \right) \\ &= \sum_{\alpha=a,b} \gamma_\alpha \left([s_\alpha, \tilde{\rho}(t) s_\alpha] + [s_\alpha \tilde{\rho}(t), s_\alpha] \right). \end{aligned} \tag{3.17}$$

Now by applying the inverse transformation $\rho(t) = e^{-i(H_S + H_R)t} \tilde{\rho}(t) e^{i(H_S + H_R)t}$ on both sides of Eq. (3.17) and notice that $[s_\alpha, H_S + H_R] = 0$, we have

$$\begin{aligned} \dot{\rho}(t) &= \sum_{\alpha=a,b} \gamma_\alpha \left([s_\alpha, \rho(t) s_\alpha] + [s_\alpha \rho(t), s_\alpha] \right) \\ &= \gamma_a \left([n_a, \rho(t) n_a] + [n_a \rho(t), n_a] \right) + \gamma_b \left([n_b, \rho(t) n_b] + [n_b \rho(t), n_b] \right). \end{aligned} \tag{3.18}$$

which agrees with Eq. (2) in Ref. [54].

3.2 Application to M&M′ States under Phase Noise

3.2.1 Density Matrix

We start with the propagation of the M&M′ state through a simplified Mach-Zehnder interferometer as shown in Figure 3.1, where both photon loss and phase fluctuation are included

and the details of source and detection are again represented by their respective boxes. The input state at stage I is a M&M′ state defined as in Chap. 2. We then have a state at stage II similar to the density matrix in Sec. 2.2, which now depends on the interaction time t between the interferometer and the source of phase fluctuation. The corresponding density matrix now has time-dependent coefficients $d_i(t)(i = 1, 2, 3, 4)$, which are to be solved from the Master Equation Eq. (3.18) and are subjected to the following initial conditions:

$$
\begin{aligned}
d_1(k,k',t=0) &= \binom{m}{k}\binom{m'}{k'}|T_a|^k|R_a|^{m-k}|T_b|^{k'}|R_b|^{m'-k'},\\
d_2(k,k',t=0) &= \binom{m}{k}\binom{m'}{k'}|T_a|^{k'}|R_a|^{m'-k'}|T_b|^{k}|R_b|^{m-k},\\
d_3(k,k',t=0) &= \binom{m}{\Delta m+k}^{\frac{1}{2}}\binom{m}{\Delta m+k'}^{\frac{1}{2}}\binom{m'}{k}^{\frac{1}{2}}\binom{m'}{k'}^{\frac{1}{2}},\\
&\quad\times T_a^{\frac{1}{2}(\Delta m+2k)}R_a^{m'-k}T_b^{\frac{1}{2}(\Delta m+2k')}R_b^{m'-k'}
\end{aligned}
$$

and

$$
\begin{aligned}
d_4(k,k',t=0) &= \binom{m}{\Delta m+k}^{\frac{1}{2}}\binom{m}{\Delta m+k'}^{\frac{1}{2}}\binom{m'}{k}^{\frac{1}{2}}\binom{m'}{k'}^{\frac{1}{2}}\\
&\quad\times T_a^{\frac{1}{2}(\Delta m+2k')}R_a^{m'-k'}T_b^{\frac{1}{2}(\Delta m)+2k}R_b^{m'-k}. \qquad (3.19)
\end{aligned}
$$

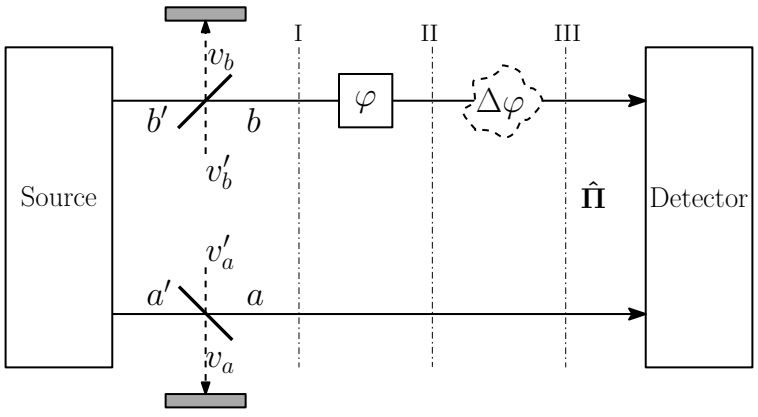

FIGURE 3.1: On top of Figure 2.2, a 'cloud' of noisy phase-fluctuation $\Delta\varphi$ is added to cause the phase fluctuation or dephasing.

Now we can calculate $\rho_{a,b}(t)$ from Eq. (3.18), term by term, as,

$$
\begin{aligned}
[n_a, \rho_{a,b}(t) n_a] &= n_a \rho_{a,b}(t) n_a - \rho_{a,b}(t) n_a^2 \\
&= \sum_{k=0}^{m} \sum_{k'=0}^{m'} \Big\{ |\alpha|^2 d_1(t) k^2 |k, k'\rangle_{a,b\ a,b}\langle k, k'| + |\beta|^2 d_2(t) k'^2 |k', k\rangle_{a,b\ a,b}\langle k', k| \Big\} \\
&\quad + \sum_{k=0}^{m'} \sum_{k'=0}^{m'} \Big\{ \alpha\beta^* d_3(t)((\Delta m)+k)k |(\Delta m)+k, k'\rangle_{a,b\ a,b}\langle k, (\Delta m)+k'| \\
&\qquad\qquad + \alpha^*\beta d_4(t) k'((\Delta m)+k') |k', (\Delta m)+k\rangle_{a,b\ a,b}\langle (\Delta m)+k', k| \Big\} \\
&\quad - \sum_{k=0}^{m} \sum_{k'=0}^{m'} \Big\{ |\alpha|^2 d_1(t) k^2 |k, k'\rangle_{a,b\ a,b}\langle k, k'| + |\beta|^2 d_2(t) k'^2 |k', k\rangle_{a,b\ a,b}\langle k', k| \Big\} \\
&\quad - \sum_{k=0}^{m'} \sum_{k'=0}^{m'} \Big\{ \alpha\beta^* d_3(t) k^2 |(\Delta m)+k, k'\rangle_{a,b\ a,b}\langle k, (\Delta m)+k'| \\
&\qquad\qquad + \alpha^*\beta d_4(t)((\Delta m)+k')^2 |k', (\Delta m)+k\rangle_{a,b\ a,b}\langle (\Delta m)+k', k| \Big\} \\
&= \sum_{k=0}^{m'} \sum_{k'=0}^{m'} \Big\{ \alpha\beta^* d_3(t) k(\Delta m) |(\Delta m)+k, k'\rangle_{a,b\ a,b}\langle k, (\Delta m)+k'| \\
&\qquad\qquad - \alpha^*\beta d_4(t)(\Delta m)((\Delta m)+k') |k', (\Delta m)+k\rangle_{a,b\ a,b}\langle (\Delta m)+k', k| \Big\},
\end{aligned}
$$

and

$$
\begin{aligned}
[n_a \rho_{a,b}(t), n_a] &= \sum_{k=0}^{m'} \sum_{k'=0}^{m'} \Big\{ -\alpha\beta^* d_3(t)(\Delta m)((\Delta m)+k) |(\Delta m)+k, k'\rangle_{a,b\ a,b}\langle k, (\Delta m)+k'| \\
&\qquad\qquad + \alpha^*\beta d_4(t) k'(\Delta m) |k', (\Delta m)+k\rangle_{a,b\ a,b}\langle (\Delta m)+k', k| \Big\}, \\
[n_b, \rho_{a,b}(t) n_b] &= \sum_{k=0}^{m'} \sum_{k'=0}^{m'} \Big\{ -\alpha\beta^* d_3(t)(\Delta m)((\Delta m)+k') |(\Delta m)+k, k'\rangle_{a,b\ a,b}\langle k, (\Delta m)+k'| \\
&\qquad\qquad + \alpha^*\beta d_4(t) k(\Delta m) |k', (\Delta m)+k\rangle_{a,b\ a,b}\langle (\Delta m)+k', k| \Big\}, \\
[n_b \rho_{a,b}(t), n_b] &= \sum_{k=0}^{m'} \sum_{k'=0}^{m'} \Big\{ \alpha\beta^* d_3(t) k'(\Delta m) |(\Delta m)+k, k'\rangle_{a,b\ a,b}\langle k, (\Delta m)+k'| \\
&\qquad\qquad - \alpha^*\beta d_4(t)(\Delta m)((\Delta m)+k) |k', (\Delta m)+k\rangle_{a,b\ a,b}\langle (\Delta m)+k', k| \Big\}.
\end{aligned}
$$

Therefore, we have the evolution of the density matrix $\rho(t)$ as:

$$\dot{\rho}(t) = -(\Delta m)^2(\gamma_a + \gamma_b)\times$$
$$\sum_{k,k'=0}^{m'} \left\{ \alpha\beta^* d_3(t)|\Delta m + k, k'\rangle_{a,b\ a,b}\langle k, \Delta m + k'| + \alpha^*\beta d_4(t)|k', \Delta m + k\rangle_{a,b\ a,b}\langle \Delta m + k', k| \right\}.$$

and

$$\begin{aligned}\rho(t) = & \sum_{k=0}^{m}\sum_{k'=0}^{m'} \left\{ |\alpha|^2 d_1(0)|k, k'\rangle_{a,b\ a,b}\langle k, k'| + |\beta|^2 d_2(0)|k', k\rangle_{a,b\ a,b}\langle k', k| \right\} \\ & + \sum_{k,k'=0}^{m'} \left\{ \alpha\beta^* d_3(0) e^{-(\Delta m)^2(\gamma_a+\gamma_b)t}|\Delta m + k, k'\rangle_{a,b\ a,b}\langle k, \Delta m + k'| \right. \\ & \qquad \left. + \alpha^*\beta d_4(0) e^{-(\Delta m)^2(\gamma_a+\gamma_b)t}|k', \Delta m + k\rangle_{a,b\ a,b}\langle \Delta m + k', k| \right\}.\end{aligned}$$

This makes sense because we are dealing with pure dephasing and the diagonal terms of the density matrix (population) should have no change. It is straightforward to see that

$$\begin{aligned} & d_{1,2}(t) = d_{1,2}(0); \\ \text{and} \quad & d_{3,4}(t) = e^{-(\Delta m)^2\gamma t} d_{3,4}(0), \end{aligned} \tag{3.20}$$

where $\gamma_a = 0$ and $\gamma_b = \gamma$ are assumed in light of Figure 3.1.

3.2.2 Derivation of the Relation between $\Delta\varphi$ and γ

In our model we have the phase-fluctuations as $\Delta\varphi(t)$ and the off-diagonal terms in the density matrix $\rho(t)$ is changed by a factor of $\exp(-(\Delta m)^2\gamma t)$. We therefore need to specify the relation between the phase-fluctuation distribution and this factor, which is fairly straightforward. Similar to the Brownian motion conditions, there are two distinct time scales in our derivation:

dt: The time scale that describes the fluctuation of the *instantaneous* force between the system S and the reservoir R, which is on the order of collision time. One may think of many water molecules collide with the 'big' pollen particle. In the Central Limit Theorem, the sum effect of a lot of independent/random collisions (each of which are

not necessarily Gaussian) amounts to a random process with a Gaussian probability density. Therefore for each infinitesimal time dt, we will have a *Wiener noise* [55] whose variance $V = \sigma^2 = dt$. This sum considers a lot of random process at the *same* time dt.

t: The time scale over which the system S evolves appreciably and $t = \int_0^t dt$. This can be thought of as the jiggling of the direction/velocity of the pollen. This is the sum of a lot of Wiener processes, one for each dt, which is also a Gaussian distribution, with zero average and variance $V = t$.

By assuming a Wiener noise $\Delta\varphi(t)$ with zero average and a variance $V[dW] = \kappa dt$ (κ is the dephasing rate which can be measured) in our calculation, it is easy to show that

$$\langle \Delta\varphi(t) \rangle = 0, \tag{3.21}$$

$$V[\Delta\varphi(t)] = \kappa t, \tag{3.22}$$

$$P(\Delta\varphi(t)) = \frac{1}{\sqrt{2\pi\kappa t}} \exp\left(\frac{-(\Delta\varphi(t))^2}{2\kappa t}\right), \tag{3.23}$$

where $P(\Delta\varphi(t))$ is the Gaussian probability density function (PDF) of the phase-fluctuation at time t. In the limit of small $\Delta\varphi$, we have

$$\exp(i(\Delta m)(\Delta\varphi(t))) \approx 1 + i(\Delta m)\Delta\varphi(t) - \frac{1}{2}(\Delta m)^2(\Delta\varphi(t))^2, \tag{3.24}$$

and therefore

$$\begin{aligned} \langle \exp(i(\Delta m)(\Delta\varphi)\rangle &= \int_0^t dt' \exp(i(\Delta m)(\Delta\varphi(t')))P(\Delta\varphi(t')) \\ &\approx 1 - \frac{1}{2}(\Delta m)^2\langle(\Delta\varphi(t))^2\rangle \\ &= 1 - \frac{1}{2}(\Delta m)^2\kappa t \end{aligned} \tag{3.25}$$

where in the last line we have used the fact that $\langle \Delta\varphi(t) \rangle = 0$. Now compare it with the decay terms in the off-diagonal terms we have $\gamma = \kappa/2$.

3.3 Visibility and Sensitivity

To focus on the effect of phase fluctuation, we first assume zero photon loss and the corresponding density matrix at time t becomes

$$\begin{aligned}\rho_{\mathrm{M\&M'}}(t) = \; & |\alpha|^2|m,m'\rangle\langle m,m'| + |\beta|^2|m',m\rangle\langle m',m| \\ & + \alpha^*\beta e^{-(\Delta m)^2\gamma t}|m,m'\rangle\langle m',m| \\ & + \alpha\beta^* e^{-(\Delta m)^2\gamma t}|m',m\rangle\langle m,m'|. \end{aligned} \tag{3.26}$$

The similar equation for the N00N state can be obtained from Eq. (2.2) as

$$\begin{aligned}\rho_{\mathrm{N00N}}(t) = \; & |\alpha|^2|N,0\rangle\langle N,0| + |\beta|^2|0,N\rangle\langle 0,N| \\ & + \alpha^*\beta e^{-N^2\gamma t}|N,0\rangle\langle 0,N| \\ & + \alpha\beta^* e^{-N^2\gamma t}|0,N\rangle\langle N,0|. \end{aligned} \tag{3.27}$$

We again adopt the parity operator Π at stage III inside the Mach-Zehnder interferometer [47] and expand it in number basis as

$$\Pi = i^{(m+m')}\sum_{k=0}^{m}(-1)^k|k,(m+m')-k\rangle\langle(m+m')-k,k|. \tag{3.28}$$

And it should be noticed that the parity operator inside the interferometer detects both mode a and b of the field (see Figure 3.1). The expectation value of the parity for the M&M$'$ state is then calculated as

$$\begin{aligned}\langle\Pi\rangle_{\mathrm{M\&M'}} =& \mathrm{Tr}\left(\Pi\rho_{\mathrm{M\&M'}}\right) \\ =& (-1)^{(m+m')}e^{-(\Delta m)^2\gamma t}\cos(\Delta m(\varphi-\pi/2)). \end{aligned} \tag{3.29}$$

If we put a half-wave plate in front of the phase shifter, which amounts to replace φ by $\varphi+\pi/2$, the expectation value becomes,

$$\langle\Pi\rangle_{\mathrm{M\&M'}} = (-1)^{(m+m')}e^{-(\Delta m)^2\gamma t}\cos(\Delta m\varphi). \tag{3.30}$$

Similarly we can also obtain the expectation value of the parity operator for the N00N state as

$$\langle \Pi \rangle_{\mathrm{N00N}} = \ (-1)^N e^{-N^2 \gamma t} \cos(N\varphi). \tag{3.31}$$

3.3.1 Visibility

Similar to Chap. 2, we use quantify the degree of measured phase information by defining the phase-fluctuation-dependent relative visibility as

$$V_{\mathrm{M\&M'}} = \frac{\langle \Pi_{\mathrm{M\&M'}} \rangle_{\max} - \langle \Pi_{\mathrm{M\&M'}} \rangle_{\min}}{\langle \Pi_{\mathrm{M\&M'}}(\gamma = 0) \rangle_{\max} - \langle \Pi_{\mathrm{M\&M'}}(\gamma = 0) \rangle_{\min}}, \tag{3.32}$$

where the numerator corresponds to the difference in the maximum and minimum parity signal in presence of phase fluctuations, while the denominator corresponds to the one with no dephasing, *i.e.* $\gamma = 0$. Visibility for the N00N state is similarly defined as

$$V_{\mathrm{N00N}} = \frac{\langle \Pi_{\mathrm{N00N}} \rangle_{\max} - \langle \Pi_{\mathrm{N00N}} \rangle_{\min}}{\langle \Pi_{\mathrm{N00N}}(\gamma = 0) \rangle_{\max} - \langle \Pi_{\mathrm{N00N}}(\gamma = 0) \rangle_{\min}} \tag{3.33}$$

Using Eqs. (3.30) and (3.31), we then obtain the visibilities for the M&M$'$ state

$$V_{\mathrm{M\&M'}} = e^{-(\Delta m)^2 \gamma t} \tag{3.34}$$

and for the N00N state

$$V_{\mathrm{N00N}} = e^{-N^2 \gamma t}. \tag{3.35}$$

We note that the visibility of the N00N state with the parity detection in Eq. (3.35) agrees with the visibility in Ref. [54].

The visibility in Eqs. (3.34) and (3.35) depends on the value of the decay rate γ and N (or $\Delta m = m - m'$), and for a given value of γ, the visibility falls down faster as N increases. Hence, N00N states (or M&M$'$ states) with large number of photons do not provide a way to obtain better visibility in presence of dephasing. This is shown in Figure 3.2, where we plotted the visibility for different N (or Δm) with respect to the decay rate γ.

3.3.2 Phase Sensitivity

We now calculate the phase sensitivity for both the M&M′ and N00N states using the expectation values of the parity operator obtained above. Phase sensitivity $\delta\varphi$ is again calculated by the linear error propagation method $\Delta\Pi/|\partial\langle\Pi\rangle/\partial\varphi|$, where $\Delta\Pi = \sqrt{\langle\Pi^2\rangle - \langle\Pi\rangle^2}$. Given $\langle\Pi^2_{\mathrm{M\&M'}}\rangle = 1$ the phase-sensitivity with the parity detection for the M&M′ state is then

$$\delta\varphi_{\mathrm{M\&M'}} = \sqrt{\frac{1 - e^{-2(\Delta m)^2\gamma t}\cos^2(\Delta m\varphi)}{(\Delta m)^2 e^{-2(\Delta m)^2\gamma t}\sin^2(\Delta m\varphi)}}. \tag{3.36}$$

For the N00N state the phase-sensitivity with the parity detection is similarly obtained as

$$\delta\varphi_{\mathrm{N00N}} = \sqrt{\frac{1 - e^{-2N^2\gamma t}\cos^2 N\varphi}{N^2 e^{-2N^2\gamma t}\sin^2 N\varphi}}. \tag{3.37}$$

We note that in the limit of no dephasing ($\gamma \to 0$), $\delta\varphi_{\mathrm{M\&M'}} \to 1/(\Delta m)$. For the N00N state, $\gamma \to 0$ case leads to $\delta\varphi_{\mathrm{N00N}} \to 1/N$ (Heisenberg limit for the NOON state). In Figure 3.3, we plot the phase sensitivities $\delta\varphi_{\mathrm{M\&M'}}$ and $\delta\varphi_{\mathrm{N00N}}$ for the various dephasing rates γ choosing $\Delta m = N$, so that the amount of phase information is the same for either state. For $\Delta m = N$, Eqs. (3.36) and (3.37) show that the M&M′ and N00N states give rise to the same phase

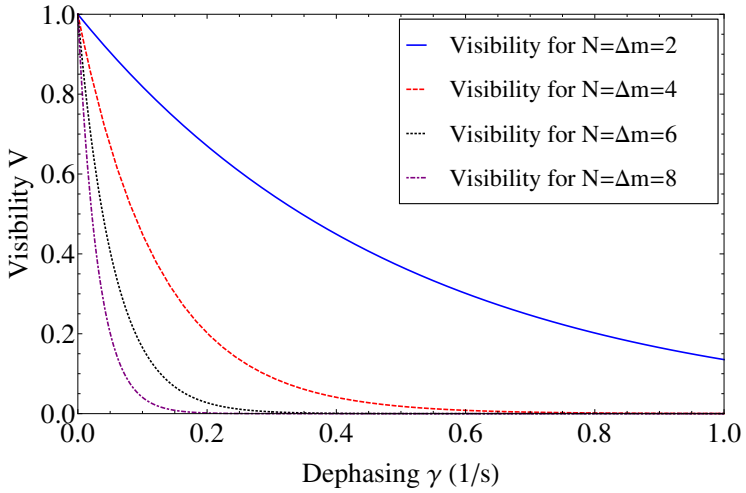

FIGURE 3.2: Visibility V of the M&M′ state for different $\Delta m = m - m'$ (for different N in case of N00N states with the same phase information) as a function of γ. The visibility V is plotted for N (or Δm) $= 2$ (solid blue curve), N (or Δm) $= 4$ (dashed red curve), N (or Δm) $= 6$ (dotted black curve) and N (or Δm) $= 8$ (dot-dashed purple curve). We see that the visibility drops faster for larger values of Δm (or N).

sensitivity. In particular, we show the phase sensitivity for the states $|4 :: 0\rangle$ and $|5 :: 1\rangle$ and find that both the states perform equally well in the presence of phase fluctuations when parity detection is used, although the former has been shown to outperform N00N states in the presence of photon loss [29, 56].

The minimum phase sensitivities $\delta\varphi_{\min}$ can be obtained from Eqs. (3.36) and (3.37) for $\varphi = \pi/(2\Delta m)$, or $\varphi = \pi/(2N)$ for the M&M$'$ or N00N states, respectively. For the $|4 :: 0\rangle$ and $|5 :: 1\rangle$ states, we plot the minimum phase sensitivity $\delta\varphi_{\min}$ in Figure 3.4 as a function of γ and compare it with the SNL and HL for both the states. The HL for a general M&M$'$ state is $1/(m + m')$ in terms of the total number of photons available and is equal to $1/N$ for the N00N state. The SNL for these two states are given by $1/\sqrt{m + m'}$ and $1/\sqrt{N}$, respectively. In Figure 3.4, we see that the minimum phase sensitivity $\delta\varphi_{\min}$ hits the HL for

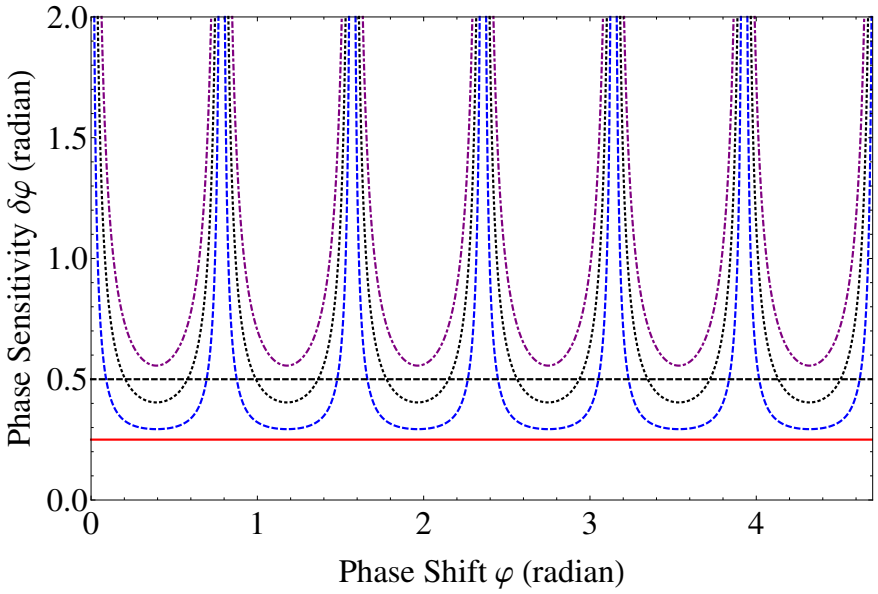

FIGURE 3.3: Phase sensitivity $\delta\varphi$ of the M&M$'$ state $|5 :: 1\rangle$, or the N00N state $|4 :: 0\rangle$, having the same phase information, as a function of phase shift φ from a two-mode interferometer for different values of γ. $\gamma = 0.1$ (dashed blue curve), $\gamma = 0.3$ (dotted black curve) and $\gamma = 0.5$ (dot-ashed purple curve). The Heisenberg limit $(1/N)$ and the shot-noise limit $(1/\sqrt{N})$ of the phase sensitivity for the N00N state are shown by the solid red line and the dashed black line, respectively, for comparison. Notice even though the curves for the N00N state and M&M$'$ state overlap with each other, their respective HL and SNL are different, where total number of photon is counted. Therefore when $N = \Delta m$, the N00N state is always the better choice under pure phase fluctuations.

the N00N state for $\gamma = 0$ only, while it never reaches the HL for the M&M′ state. However, $\delta\varphi_{\min}$ is below the SNL for both of the states for small values of γ, but increase in the phase fluctuation leads to the phase sensitivity above the SNL, as shown in Figure 3.4.

3.3.3 Effects of Both Photon Loss and Phase Fluctuations

If consider both photon loss (modeled by two fictitious beam splitters with reflectance R_a and R_b as shown in Figure 3.1) and phase fluctuations, we define the time-dependent parity signal as

$$K_1(t) = \sum_{k=0}^{m'} \left(d_1(k,k,t) + d_2(k,k,t)\right),$$
$$K_2(t) = \sum_{k=0}^{m'} \left(d_3(k,k,t) + d_4(k,k,t)\right). \tag{3.38}$$

And recall the coefficients in Eq. (3.20), it is straightforward to see $K_1(t) = K_1(0)$ and $K_2(t) = K_2(0)e^{-(\Delta m)^2\gamma t}$, where $K_{1,2}(0)$ are defined in Chap. 2. We now have the time-dependent parity signal as

$$\langle \Pi \rangle = K_1(t) + (-1)^{m+m'} K_2(t) \cos((\Delta m)\varphi), \tag{3.39}$$

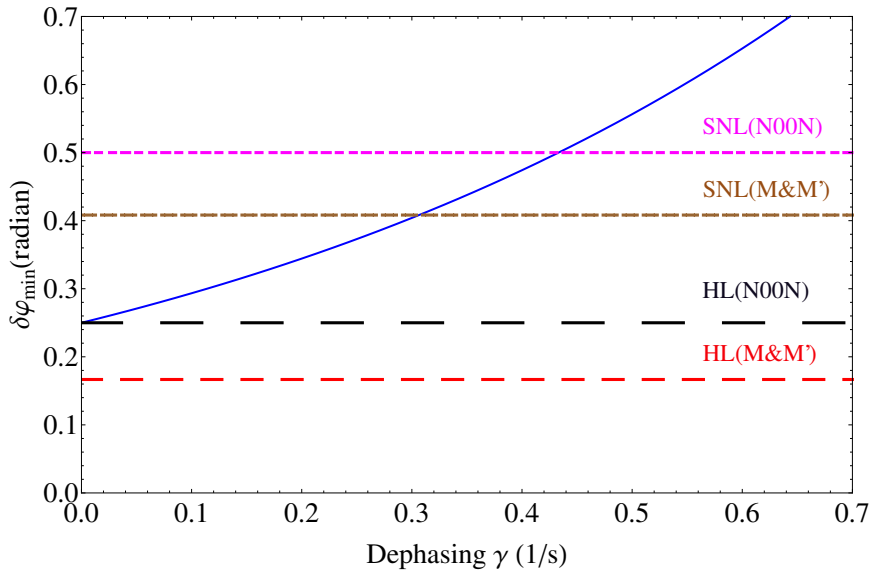

FIGURE 3.4: Minimum phase sensitivity $\delta\varphi_{\min}$ of the M&M′ state $|5 :: 1\rangle$ or the N00N state $|4 :: 0\rangle$ as a function of γ. The shot-noise limit (SNL) and the Heisenberg limit (HL) of the phase sensitivity for both the states are also shown for comparison.

where the $\pi/2$ phase shift is applied. A relative visibility with respect to both loss and phase-fluctuations can be defined as

$$\begin{aligned} V_{\mathrm{M\&M'}} &= \frac{\langle \Pi_{\mathrm{M\&M'}} \rangle_{\max} - \langle \Pi_{\mathrm{M\&M'}} \rangle_{\min}}{\langle \Pi_{\mathrm{M\&M'}}(\gamma = 0, L = 0) \rangle_{\max} - \langle \Pi_{\mathrm{M\&M'}}(\gamma = 0, L = 0) \rangle_{\min}}, \\ &= K_2(0) e^{-\Delta m^2 \gamma t} \end{aligned} \tag{3.40}$$

where L stands for the loss in both paths (R_a and R_b). In the limit of $L \to 0$, $K_2(0)$ approaches one and the visibility reduces to the previous result. Notice the depahsing only affects the off-diagonal terms of the density matrix while loss affects both diagonal and off-diagonal terms. However, because of the linearity of the MZI, the effect from photon loss is independent of that from phase-fluctuation, as expected.

This signal also gives rise to the phase-sensitivity for the parity detection for a M&M$'$ state under both photon-loss and phase-fluctuations as

$$\delta\varphi_{\mathrm{M\&M'}} = \sqrt{\frac{1 - \left\{ K_1(t) + (-1)^{m+m'} K_2(t) \cos(\Delta m \varphi) \right\}^2}{\left\{ \Delta m K_2(t) \sin(\Delta m \varphi) \right\}^2}}, \tag{3.41}$$

where linear error propagation method is employed. Notice that when loss is negligible this sensitivity recovers Eq. (3.36). All results in this section apply to N00N states with $N = m$ and $m' = 0$.

3.3.4 Quantum Cramér-Rao Bound

In this last subsection, we calculate the Quantum Cramér-Rao Bound (QCRB) for both the M&M$'$ and N00N states in presence of the phase fluctuations, and show that the parity detection attains the QCRB for both of these states subject to the dephasing. A general framework for estimating the ultimate precision limit in noisy metrology has been studied by Escher *et al.* in Ref. [33], where they considered the *system+reservoir* as a big system and treated the configuration of the MZI as an variational parameter whose optimal value leads to the best precision.

By evaluating ρ_φ and $\partial\rho_\varphi/\partial\varphi$ from Eq. (3.26), we obtain the quantum Fisher information (see Sec. 1.2.2) for the M&M$'$ state

$$F_{\mathrm{M\&M'}} = (\Delta m)^2 e^{-2(\Delta m)^2\gamma t} \tag{3.42}$$

leading to the quantum Cramér-Rao bound

$$\delta\varphi_{\mathrm{QCRB,M\&M'}} \geq \frac{1}{\sqrt{F_{mm'}}} = \frac{1}{(\Delta m)e^{-(\Delta m)^2\gamma t}}. \tag{3.43}$$

For the N00N states, similar calculation yields

$$F_{\mathrm{N00N}} = N^2 e^{-2N^2\gamma t}, \tag{3.44}$$

and

$$\delta\varphi_{\mathrm{QCRB,\ N00N}} \geq \frac{1}{\sqrt{F_{\mathrm{N00N}}}} = \frac{1}{Ne^{-N^2\gamma t}}. \tag{3.45}$$

Eqs. (3.43) and (3.45) represent the lowest bound on the uncertainty of the phase measurement for the M&M$'$ and N00N states, respectively.

For a detection scheme to be optimal, it has to saturate the quantum Cramér-Rao bound. Eqs. (3.36) and (3.37) represent phase sensitivity for the M&M$'$ and N00N states respectively, and these expressions can be shown to be identical to the quantum Cramér-Rao bounds in Eqs. (3.43) and (3.45) for $\varphi = \pi/(2\Delta m)$, or $\varphi = \pi(2N)$ for the M&M$'$ or N00N states respectively. Thus, parity detection saturates the quantum Cramér-Rao bounds and is optimal for both the states in presence of the phase fluctuations.

3.4 Conclusion

In this chapter, we studied the effects of phase fluctuations on the phase sensitivity and visibility of M&M$'$ and N00N states in an optical interferometric setup. Although M&M$'$ states are more robust than N00N states against photon loss, we showed that they do not provide any better performance in presence of such phase fluctuations than their equivalent N00N counterpart. We have used the parity detection technique for phase estimation and

presented a brief study on the quantum Fisher information for both states. It is shown that for both the states parity detection serves as the optimal detection strategy as it saturates the quantum Cramér-Rao bound of the interferometric scheme.

Chapter 4
Quantum Sensing and Quantum Radar

In this chapter we discuss the application of quantum optical states in the field of quantum remote sensing, *i.e.*, the design of a quantum radar. For remote sensing, atmospheric absorption and diffraction rapidly degrades any actively transmitted quantum states of light, such as the N00N states discussed in Chap. 2, so that for this high-loss regime the optimal strategy is to transmit the coherent state of light, which suffers no worse loss than the linear Beer's law (also known as Beer-Lambert law) for classical radar attenuation and provides sensitivity at the shot-noise limit in the returned power. We show that coherent radar radiation sources, coupled with a quantum homodyne detection scheme, provide both longitudinal and angular super-resolution much below the Rayleigh diffraction limit, with sensitivity at shot-noise in terms of the detected photon power. Our approach provides a template for the development of a complete super-resolving quantum radar system with currently available technology.

In Sec. 4.1 we briefly discuss previous efforts that motivated us to the current scheme of quantum radar. In Sec. 4.2 we review the use of quantum parity detection to produce super-resolving ranging measurements at the shot-noise limit. In Sec. 4.3 we discuss the quantum homodyne detection scheme as an implementation of parity detection. In Sec. 4.4 we show how to modify the technology to provide super-resolved angular determination. A conclusion is presented in Sec. 4.5.[1]

[1]Part of this chapter previously appeared as Kebei Jiang, Hwang Lee, Christopher C. Gerry and Jonathan P. Dowling, *Super-resolving quantum radar: Coherent-state sources with homodyne detection suffice to beat the diffraction limit*, J. Appl. Phys, **114**, 193102 (2013). It is reprinted by permission of the American institute of Physics (AIP). See the permission letter in Appendix B.

4.1 Previous Work

Ever since the work of our group (Quantum Science and Technology group in Louisiana State University) on quantum lithography, it has been shown that entangled quantum states of the electromagnetic field, such as the Schrödinger-cat-like N00N states, provide a resolving power that is sub-Rayleigh diffraction limited (super-resolution) and a sensitivity that is sub-shot-noise limited (super-sensitivity) [57, 58, 59, 16]. This realization of a quantum-entanglement advantage leads to proposals to develop remote quantum sensors, quantum lidar and quantum radar. In the particular case of quantum radar, such quantum states of light are actively transmitted through the atmosphere, reflected off the target, and then upon return provide sub-Rayleigh diffraction resolution in ranging [60]. We show two radar systems based on either a Michelson (Figure 4.1) or a Mach-Zehnder (Figure 4.2) interferometer, the former of which is typically deployed in coherent lidar and radar systems.

N00N states in remote sensing is deployed in an interferometric mode where half of the N00N state is transmitted to the target and reflected back and later mixed with the other half at the detector. We illustrate such a quantum-entangled radar system in Figure 4.1(a) where the entangled photon source is attached to a Michelson interferometer in a monostatic configuration.[2] This kind of quantum-entangled radar scheme requires that one half of the N00N state be retained at the radar station and stored in a low-loss delay line for a time equal to the round trip time that the other half takes between the radar station and the target. Implementing the correct delay time then requires approximate advanced knowledge of the distance to the target. Such an quantum-entangled radar system could not be a stand alone system, but would have to work with the simultaneous deployment of a conventional radar at the same site.

[2]The term 'monostatic' means the source and the detector are at the same location as compared to 'bistatic' where they are in different locations.

A more severe problem with this entangled-photon approach to quantum radar, which is as well mentioned in Chap. 2, is that the N00N states are very susceptible to the loss expected from absorption and scattering in the atmosphere and also from diffraction (this implies that not all of the N00N state would be detected upon return due to the finite size of the detector aperture) [26, 61, 62]. Unavoidable loss would also be present in the delay line. Our group provided a quantum theoretical interpretation of this 'super-Beer' loss behavior for N00N states in terms of the quantum 'which-path' information available to the environment upon photon loss [29, 63]. In that same paper we introduced the M&M′ states, which is defined in Chap. 2, as a robust alternative of the N00N states. If $m - m' = N$, then the state remains N-fold super-resolving, and for low loss can still do better than shot-noise in sensitivity. In such M&M′ states the m' decoy photon keeps the complete 'which-path'

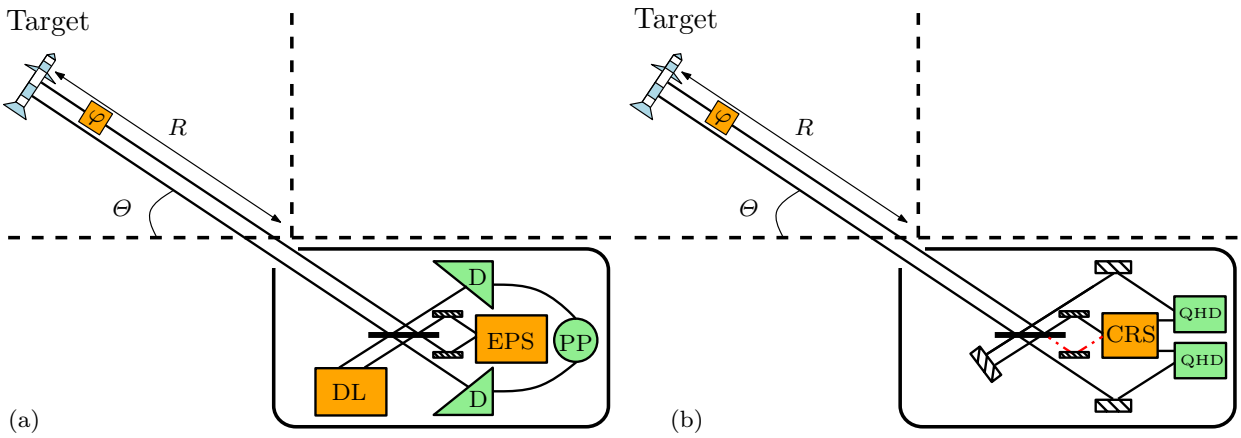

FIGURE 4.1: Here we compare two monostatic quantum radar systems in a Michelson configuration. The first (a) uses an entangled photon source (EPS) and photon number resolving detectors, and the second (b) uses a coherent radar source (CRS) and quantum homodyne detection (QHD). In both the range distance R and the altitudinal angle above the horizon Θ are shown. For clarity the azimuthal angle Φ along the horizon is suppressed. The phase shifter φ is the relative phase between the two arms, which carries the range information. In (a) half of the entangled state from the EPS is reflected off the target and half is stored in a delay line (DL). The photon-counting detectors (D) then sends their data to a post-processor (PP). In (b) the EPS is replaced with a CRS, the DL is replaced with a mirror, and the detection is carried out using two QHDs. Dotted red lines in (b) indicates the quantum vacuum that enters in the unused port of the interferometer. The solid black rectangle is a beam splitter and the striped rectangles are mirrors. The lines connecting the CRS to the QHDs shows that the same radar source may be used as the local oscillator in the QHD.

information from becoming available to the environment with just a single photon lost. The ranging information is then better preserved.

Our group then set out to numerically search Hilbert space for quantum states of the electromagnetic field with best sensitivity under a specified loss [34]. The results there indicate that for the low loss regime the N00N states are optimal, for intermediate loss the M&M′ states are optimal, but that *at high loss only coherent states are optimal*. Konrad Banaszek, Ian Walmsley, and their collaborators, independently discovered this result about the same time [35, 36]. Since coherent states are the natural output of a conventional lidar or radar source, their conclusion was that switching from coherent to entangled states would not give sub-shot-noise sensitivity in the high-loss regime, because it is known that coherent states by themselves will always achieve at best shot-noise sensitivity in the return power [13]. That is, *super-sensitivity with entangled state transmission is impossible to achieve when total loss exceeds about 6 dB*. This means a entangled-photon radar is useless for most applications. This conclusion motivated us to search for a scheme using coherent states for *super-resolving* lidar and radar in the high-loss regime while maintaining shot-noise-limit sensitivity with respect to the return power. That is to remove the fragile entanglement and still beat the Rayleigh diffraction limit with coherent states alone.

First of such effort was made in 2007 when the group of Andrew White demonstrated that coherent states could indeed provide super-resolution if a quantum detection scheme was deployed [37]. In this scheme of Resch *et al.* they projected the return coherent state onto a N00N-state basis to extract resolution for a particular N00N state component of the two-mode coherent field in the interferometer by doing high-efficiency N-photon counting [64]. By using this technique they demonstrated six-fold super resolution. However such a scheme throws away most of the returning photons and is much worse than shot-noise in sensitivity. Hence it is far from ideal in situations where only few photons are expected to return from a distant target as is typical for long-range radar systems. In addition such a

scheme would require photon number resolving detectors of high efficiency which are not yet available at lidar and radar wavelengths.

In 2010 our group managed to find a coherent-state quantum detection scheme that was both super-resolving and that operated at the shot-noise limit in sensitivity. We showed that super-resolution (in longitudinal ranging) at the shot-noise limit with coherent states can be achieved by using the quantum parity detection [64]. Hwang Lee and Yang Gao in our group showed that parity detection provides a unifying measurement scheme in quantum metrology as it provides sub-shot-noise sensitivity with respect to a wide range of quantum-entangled states of the electromagnetic field [65].

One remaining practical drawback to our 2010 proposal, for super-resolving lidar and radar ranging with coherent states alone, was that back then the way to implement the quantum parity detection involved either the use of very strong Kerr nonlinearities [66] or high-efficiency photon-number resolving detectors [64]. The Kerr approach requires high-power in the return radar field, which is not usually the case. For long-wavelength radar systems, due to diffraction, the source emits power in nearly a spherical wave and the ratio of power transmitted to power received back scales as $1/R^4$, where R is the range distance to the target and is typically tens to hundreds of kilometers. For example, if the target is 100 kilometers distant, then for a radar system that transmits a kilowatt in outgoing power, the return power will only be about 400 fW. On the other hand, the photon-number resolved detection approach is problematic in the infrared, the microwave and longer wavelength radar regimes where photon-number detectors have extremely low efficiency [67].

The breakthrough that allows us to apply parity measurement to lidar and radar wavelengths came in 2010. In collaboration with Girish Agarwal, our group showed that parity detection of the coherent state can be carried out with a simple quantum homodyne detection scheme [51]. Homodyne detection mixes the return radar state in the system with a local oscillator, which is a stable radar source of the same frequency as the transmitted

beam and with a known and adjustable phase [68]. The point was to recognize that a parity measurement of a single-mode electromagnetic field is equivalent to measuring the Wigner function of the field at the origin in phase space [69, 70, 71, 72]. An additional advantage of coherent-state quantum radar is that the delay line used in the entangled state protocol is no long required. The delay line may be replaced with a stable radar local oscillator and thus we do not need advance knowledge of the distance to the target. Therefore our proposed quantum radar system operates as a stand-alone system. The homodyne technique has the additional advantage that the local oscillator can boost the signal well above the thermal noise floor of radar detectors. We still need high-efficiency detectors (which can be routinely made with superconductor technology) but not the number resolving feature. With such a scheme the presence or absence of even a single photon in the return field may be detected [73].

In the 2010 paper, in collaboration with Jerome Luine at Northrop-Grumman, our group compared parity measurement with a closely related 'on-off' photon detection scheme. In a 'on-off' detection scheme the detector distinguishes between zero photons versus more than zero photons in a single mode. The numerical simulation showed that such a scheme provides super-resolution comparable to that of parity detection [64]. Recently the group of Ulrik Andersen has proposed and implemented a homodyne version of the 'on-off' detection scheme and has experimentally demonstrated super-resolution at the shot-noise limit with coherent states and a quantum detection scheme [74]. Independently the group of Hagai Eisenberg has also experimentally demonstrated super-resolution at the shot-noise limit using only coherent light and homodyne-based parity detection [75]. These results, both carried out with visible light, vindicate our approach and lead us to believe that the entire scheme may now be scaled to the infrared, microwave and long-wavelength radar regimes.

Last but not the least, in all the schemes discussed above we have shown how to obtain super-resolved ranging information, which is the distance to the target, R. To completely

characterize the location of a distant target we need super-resolving altitudinal angle Θ (location of the target above the horizon) and azimuthal angle Φ (location of the target along the horizon. See Figure 4.1) as well. This angular information is of particular importance in long-wavelength radar systems, where the target may be tens or hundreds of kilometers away and the radar power is reflected back in a spherical wave. This means that the return radar signal arrives at the detector essentially as a plane wave, which makes the determination of the angular position of the target very difficult. The trick is to convert the angular information into a phase shift and then use the same technique used to acquire super-resolved range information to obtain super-resolved angular information. Together with ranging we then have complete super-resolved angular location of the target embodied in the determination of R, Θ and Φ.

4.2 Super-Resolved Ranging with Parity Detection

It is usually helpful to analyze the Michelson interferometer (MI) in Figure 4.1(b) as an unfolded MZI shown in Figure 4.2. The performance of an MZI and the MI are identical. The MZI corresponds to a bistatic radar system where the source and detector are at different locations and the MI to a monostatic system where the source and detector are co-located. The only physical difference is that the MZI has two separate beam splitters (BS) and the MI has a single beam splitter that is utilized twice. As shown in Figure 4.2 the unknown phase to be detected is denoted by φ and is given by $\varphi = k\ell$, where k is the wave number, λ is the wavelength and ℓ is the path-length *difference* between the two arms of the interferometer that lie between the two BS. In the MI configuration of Figure 4.1(b) the length of the lower reference arm can be made to be zero and then $\ell = R$ is the range to the target we are trying to estimate.

The output of the CRS is a coherent state $|\alpha\rangle$ (see Sec. 1.1.1) with $\alpha = \sqrt{\bar{n}}e^{i\theta}$, where $\sqrt{\bar{n}}$ and θ are the amplitude and phase of the field, respectively. Since we are only interested in the phase difference accumulated upon propagation, we can assume $\theta = 0$ and so $\alpha = \sqrt{\bar{n}}$

is real. For a coherent state the measurement of the intensity will yield only $\bar{n}$ photons on average with quantum fluctuations about this mean on the order of $\Delta n = \sqrt{\bar{n}}$. Notice this is related to the famous shot-noise limit we discussed in Chapter 1, which is the best sensitivity one can get using classical sources. Only in the classical limit, when the intensity is very large, is Δn negligible compared to $\bar{n}$. As we are particularly interested in the situation where very few photons return to the detector, in that regime Δn cannot be neglected compared to $\bar{n}$ and the quantum theory of light must be used [4].

As shown in Figure 4.2 we emit a coherent state input mixed with vacuum at the first BS that we write as $|\beta\rangle_{\rm A}^{\rm in}|0\rangle_{\rm B}^{\rm in}$. The output becomes $|\alpha\cos(\varphi/2)\rangle_{\rm A}^{\rm out}|\alpha\sin(\varphi/2)\rangle_{\rm B}^{\rm out}$ [16]. Here $\alpha = e^{-\Gamma R/2}\beta$ is the attenuated coherent state at the detector, where Γ is the linear intensity attenuation coefficient and R is the range. We also assume the lower path to be attenuation free which is consistent with the monostatic configuration of the Michelson operation. We will later implement parity measurement at output port B. We can compute the result by noting that the expectation of the parity operator is proportional to the Wigner function of

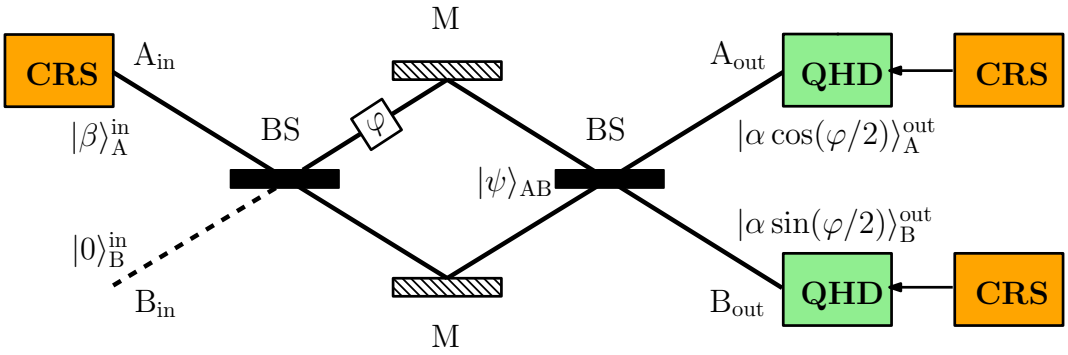

FIGURE 4.2: Here for simplicity we show the monostatic Michelson interferometer in Figure 4.1(b) unfolded into an equivalent bistatic Mach-Zehnder configuration. The coherent state from the CRS is incident in upper mode A and vacuum in lower mode B. After the first beam splitter (BS) we have a two-mode coherent state. After the phase shifter φ, which encodes the range R, this state becomes the two-mode coherent state with a relative phase difference that is reflected by the mirrors (M). Finally after the final BS on the right, we have the attenuated coherent state with the phase information and we implement the parity operator measurement in both the upper mode A and the lower mode B via QHD. The same CRS is also used to feed both QHDs to implement the balanced homodyne procedure. The use of the same CRS is a common trick in quantum optical experiments, which ensures the same frequency of the signal and the local oscillator.

the output state evaluated at the origin in phase space,

$$\langle \Pi \rangle = \langle e^{i\pi n} \rangle = \frac{\pi}{2} W(0,0), \tag{4.1}$$

where $n = b^\dagger b$ is the number operator and b is the mode operator for $\mathrm{B_{out}}$ [51]. The Wigner function for a coherent state has a particularly simple form [4],

$$W_{\alpha_\varphi}(\gamma, \gamma^*) = \frac{2}{\pi} \exp(-2|\gamma - \alpha_\varphi|^2), \tag{4.2}$$

where γ is a complex phase space coordinate and $\alpha_\varphi = \alpha \sin(\varphi/2)$ is the output coherent state in mode $\mathrm{B_{out}}$. The corresponding radar intensity in the mode is proportional to the mean photon number, defined by $\bar{n}_\varphi = |\alpha_\varphi|^2 = \bar{n} \sin^2(\varphi/2)$. Combining these two equations we get,

$$\langle \alpha_\varphi | \Pi | \alpha_\varphi \rangle = \exp\left(-2|\alpha_\varphi|^2\right) = \exp\left(-2\bar{n} \sin^2(\varphi/2)\right), \tag{4.3}$$

which agrees with previous result [64]. This signal is plotted in Figure 4.3 as a solid curve with the dashed curve being the signal from ordinary output intensity differencing (scaled by $\bar{n}$.) It is clear that the parity signal is super-resolving. As shown in Ref. [64] the width of the parity central peak can be estimated by taking $\varphi \approx 0$ so that Eq. (4.3) becomes a Gaussian $\exp(-\bar{n}\varphi^2/2)$. Then we have $\delta\varphi = 1/\sqrt{\bar{n}}$, where $\bar{n}$ is proportional to the return power. Converting this to an uncertainty in range we get,

$$\delta R_{\mathrm{Q}} = \frac{\lambda}{2\pi\sqrt{\bar{n}}}, \tag{4.4}$$

where the classical Rayleigh resolution would instead be just $\delta R_{\mathrm{C}} = \lambda$ therefore we are a factor of $2\pi\sqrt{\bar{n}}$ below the Rayleigh limit. For $\bar{n} = 100$ average return photons the quantum result is about 60 times smaller than the classical diffraction limit. *Notice that by uncertainty we mean the full width at half maximum of the parity signal in Figure 4.3, which is not the same as the sensitivity of phase estimation. The similar scaling of our super-resolution and the general shot-noise limit is merely a coincidence.*

Since extraction of the parity signal will require some post-processing, one approach would be to simply measure the output intensity $\bar{n}_\varphi$ directly and plug the result into Eq. (4.3). This approach is problematic for radar, in particular at low return photon numbers, since the best result would be obtained with efficient, low-noise, photon-number counters that are difficult to obtain at such long wavelengths. In addition the signal for few return photons will be well below the thermal noise floor of most detector at these frequencies. Also, in addition the quantum intensity fluctuations there will be classical fluctuations due to instabilities in the radar source, turbulence in the atmosphere, and so forth. Therefore a intensity differencing is usually done between output modes $\mathrm{A_{out}}$ and $\mathrm{B_{out}}$ to give a common mode noise cancellation of these classical fluctuations. To obtain the optimal performance we should measure parity at each output using balanced QHD to extract the Wigner function at the origin directly and amplify the signal to well above the thermal noise floor. We will discuss this approach in the next section.

4.3 Parity Implemented with Quantum Homodyne Detection

We propose to carry out balanced homodyne detection of the parity signal at each of the two output ports of the interferometer. Such a detection scheme is shown in Figure 4.4. Quantum

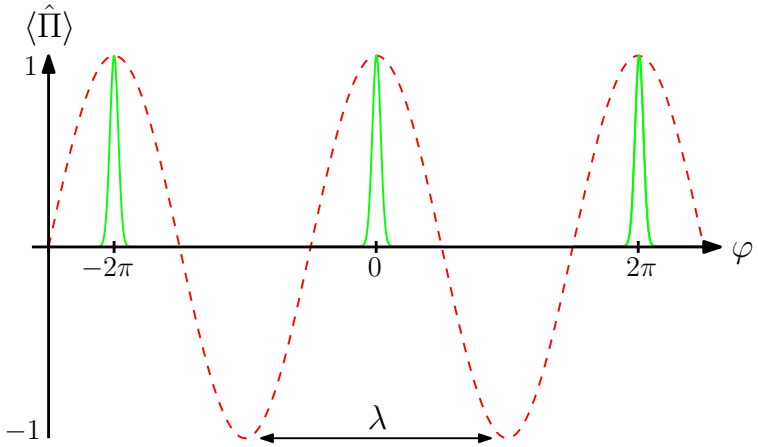

FIGURE 4.3: Here we show the signal of quantum parity detection (solid curve) against the ordinary classical signal obtained by differencing the intensity of the two detectors and scaled by the intensity (dashed curve). The parity curve is for a return power of $\bar{n} = 100$ giving a ten-fold improvement in the fringe resolution compared to that of the classical curve where the peak-to-peak spacing is at the diffraction limit of λ.

homodyne detection (QHD) is actually inspired by classical microwave radar technology called the balanced-mixer radiometer [76]. The balanced mixer is what we call here a 50:50 beam splitter. For this technique to work well in the microwave regime at the quantum level, we also require that the detectors have a high quantum efficiency, which is routinely obtained these days with superconducting technology [77]. We first work with the lower port $\mathrm{B_{out}}$. The signal output for $\mathrm{B_{out}}$ is mixed on a 50:50 beam splitter with a strong coherent state $|\delta_{\mathrm{LO}}\rangle_{\mathrm{C}}$ in mode C, which is called the local oscillator. The local oscillator may be taken from the same coherent radar source (CRS) used to perform the ranging in the monostatic Michelson configuration and it has a well define phase ϑ_{LO} so that $\left|\delta_{\mathrm{LO}}\right\rangle_{\mathrm{C}} = \left||\delta_{\mathrm{LO}}|\exp\left(i\vartheta_{\mathrm{LO}}\right)\right\rangle_{\mathrm{C}}$. The two outputs are then guided to the two detectors D and E where the intensity between them is differenced. This intensity difference, as a function of the unknown ranging phase φ, is our signal.

Using the standard beam splitter back-transformations

$$e \to 1/\sqrt{2}(b + ic),$$

$$d \to 1/\sqrt{2}(c + ib),$$

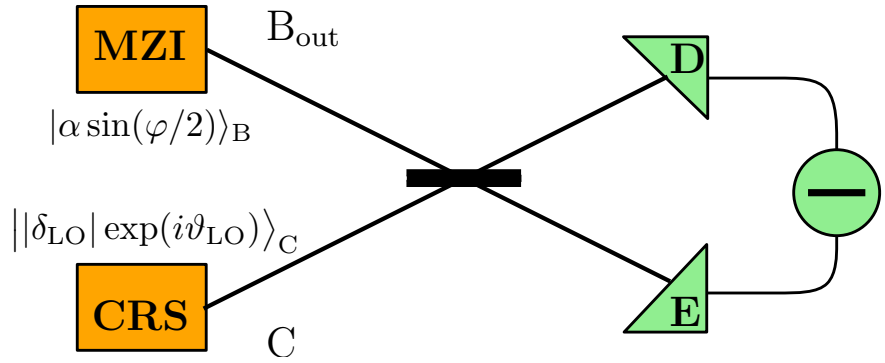

FIGURE 4.4: Here we depict the quantum homodyne detection. The lower mode output B of the Michelson interferometer (MI, unfolded and monostatic) or Mach-Zehnder interferometer (MZI, folded and bistatic) from Figure 4.2 is fed into a 50:50 beam splitter. At the other input port C to this beam splitter we insert a strong coherent state $\left|\delta_{\mathrm{LO}}\right\rangle_{\mathrm{C}} = \left||\delta_{\mathrm{LO}}|\exp\left(i\vartheta_{\mathrm{LO}}\right)\right\rangle_{\mathrm{C}}$ with a known phase ϑ_{LO}. After the beam splitter we carry out intensity differencing between the two detectors (D, E). The data is then inverted to extract the parity measurement. The same detection will be implemented on upper mode output A as well.

the intensity difference operator at the two detectors M can be written as,

$$\begin{aligned} \mathrm{M} &= e^{\dagger}e - d^{\dagger}d \\ &= i(b^{\dagger}c - c^{\dagger}b). \end{aligned}$$

This allows us to compute the expectation of M in terms of the input states. From the states shown in Figure 4.4 we have

$$\begin{aligned} Y_{\mathrm{B}}(\vartheta_{\mathrm{LO}}, \varphi) &= {}_{\mathrm{B}}\langle \alpha_{\varphi}| \, {}_{\mathrm{C}}\langle \delta_{\mathrm{LO}}|\mathrm{M}|\delta_{\mathrm{LO}}\rangle_{\mathrm{C}}|\alpha_{\varphi}\rangle_{\mathrm{B}} \\ &= {}_{\mathrm{B}}\langle \alpha_{\varphi}| \, {}_{\mathrm{C}}\langle \delta_{\mathrm{LO}}| i\left(b^{\dagger}c - c^{\dagger}b\right)|\delta_{\mathrm{LO}}\rangle_{\mathrm{C}}|\alpha_{\varphi}\rangle_{\mathrm{B}} \\ &= i\left(\langle b^{\dagger}\rangle_{\mathrm{B}}\langle c\rangle_{\mathrm{C}} - \langle c^{\dagger}\rangle_{\mathrm{C}}\langle b\rangle_{\mathrm{B}}\right) \\ &= i\left(\alpha_{\varphi}^{*}\,|\delta_{\mathrm{LO}}|e^{i\vartheta_{\mathrm{LO}}} - \alpha_{\varphi}\,|\delta_{\mathrm{LO}}|e^{-i\vartheta_{\mathrm{LO}}}\right) \\ &= -2|\alpha_{\varphi}||\delta_{\mathrm{LO}}|\sin(\vartheta_{\mathrm{LO}}) \\ &= -2\sqrt{\bar{n}_{\varphi}}\sqrt{\bar{n}_{\mathrm{LO}}}\sin(\vartheta_{\mathrm{LO}}), \end{aligned} \tag{4.5}$$

where the fact $\alpha_{\varphi}^{*} = \alpha_{\varphi}$ is used and $\bar{n}_{\varphi} = \bar{n}\sin^2(\varphi/2)$ as before. It is clear from Eq. (4.5) that a balanced quantum homodyne detector is an amplifier since, in general, $\bar{n}_{\mathrm{LO}} \gg \bar{n}$. This amplification provides a critical advantage in that the amplified signal can be made to be well above the thermal electronic noise floor of radar detectors. Hence by using a quantum balanced homodyne approach the detectors need not to be photon number resolving (difficult) but rather just highly efficient (easier) [73, 78]. In addition, the intensity differencing in balance homodyne detection removes all technical noise and classical noise of the local oscillator [73]. Finally, a well-known result in coherent LIDAR says that the signal-to-noise of the output is limited by the shot-noise of the local oscillator that scales like $\sqrt{\bar{n}_{\mathrm{LO}}}$ [79].

On the other hand, from Eq. (4.5) we have

$$|\alpha_{\varphi}| = -\frac{Y_{\mathrm{B}}(\vartheta_{\mathrm{LO}}, \varphi)}{2\sqrt{\bar{n}_{\mathrm{LO}}}\sin(\vartheta_{\mathrm{LO}})}. \tag{4.6}$$

This can be substituted into the general expressions Eqs. (4.1) and (4.2) and the parity signal from mode $\mathrm{B}_{\mathrm{out}}$ becomes

$$\langle \Pi \rangle = \frac{\pi}{2} W(0,0) \tag{4.7}$$

$$= \exp\left(-2|\alpha_\varphi|^2\right). \tag{4.8}$$

Setting the phase of the local oscillator to $\vartheta_{\mathrm{LO}} = \pi/2$ we have our reconstructed parity signal as,

$$S_{\mathrm{B}}(\varphi) = {}_{\mathrm{B}}\langle \alpha_\varphi | \Pi | \alpha_\varphi \rangle_{\mathrm{B}} \tag{4.9}$$

$$= \exp\left(-\frac{Y_{\mathrm{B}}^2(\pi/2,\varphi)}{2\bar{n}_{\mathrm{LO}}}\right), \tag{4.10}$$

where we emphasize that $Y_{\mathrm{B}}^2(\pi/2,\varphi)$ *is the measured (normalized) intensity difference between detectors D and E.* By combining Eq. (4.5) and (4.10) we recover the parity result in Eq. (4.3). However by implementing balanced homodyne detection we have gained control over signal-to-noise and removed the need for photon-number resolving radar detectors.

Since every photon is precious we should not ignore the upper exit port $\mathrm{A}_{\mathrm{out}}$ in Figure 4.2. Note that if we are working near the sweet spot of $\varphi \approx 0$ most of the signal photons will emerge at this port. By measuring φ we really mean that we are measuring the phase difference between the phase in the target arm φ_{T} and that in the reference arm φ_{R} of the interferometer. For simplicity we have set the phase of the reference arm to zero in which case $\varphi = \varphi_{\mathrm{T}}$ is the phase difference. In actual operation we would put a tunable phase shifter in the reference arm, with phase difference $\varphi = \varphi_{\mathrm{T}} - \varphi_{\mathrm{R}}$ being the signal. In this way, typically in a feed-back loop, as we gather information about φ_{T} in the data we can tune the interferometer in real time to always maintain the 'sweet spot' condition $\varphi \approx 0$. This tuning also gives us information about the absolute phase difference. The problem is that tuning the signal in the lower output port $\mathrm{B}_{\mathrm{out}}$ to the sweet spot moves it to a phase point where the signal in the upper port $\mathrm{A}_{\mathrm{out}}$ is not super resolved. Luckily, from the tuning in

the reference arm and the signal in the lower port we will have enough information about the unknown range phase φ to do the following trick on the upper port. In the homodyne measurement at $\mathrm{A_{out}}$ we take the phase of the local oscillator to be $\vartheta_{\mathrm{LO}} \approx \varphi/2$ and notice for port $\mathrm{A_{out}}$ the average photon number $\bar{n}_\varphi = \bar{n}\cos^2(\varphi/2)$, in which case Eq. (4.5) becomes

$$Y_{\mathrm{A}}(\varphi/2, \varphi) = \sqrt{\bar{n}_{\mathrm{LO}}}\sqrt{\bar{n}}\sin(\varphi).$$

This leads to the parity signal from the upper port as

$$\begin{aligned} S_{\mathrm{A}}(\varphi) &= \exp\left(-\frac{Y_{\mathrm{A}}^2(\varphi/2, \varphi)}{2\bar{n}_{\mathrm{LO}}}\right) \\ &= \exp\left(-\bar{n}\sin^2(\varphi)/2\right) \\ &\approx \exp(-\bar{n}\varphi^2/2), \end{aligned} \tag{4.11}$$

where the last term is taken near $\varphi \approx 0$ and the range resolution is the same as that of Eq. (4.4). The outputs signals of the two ports are then simply averaged to give the best estimate of the range phase.

4.4 Super-Resolved Angle Determination

In the preceding section we described how to obtain super-resolved ranging information using monostatic Michelson interferometer combined with quantum homodyne detection. Super-resolved angle information is critical for complete target location as well. However this is difficult to obtain at radar wavelengths since, as discussed in the Sec. 4.1, the return signal arrives as a plane wave. We discuss here how to get such a signal for the altitudinal angle Θ and azimuthal angle Φ. The critical point is to realize that a MZI can be mapped onto a two-slit diffraction configuration and thus the desired unknown angle can be mapped into an unknown phase. We can then use the same homodyne technique to measure that phase and extract the angle. Consider in Figure 4.5 the return signal arriving at the detector as a plane wave with a Poynting vector at an angle Θ with respect to the horizon. We again treat the signal as a coherent state $|\alpha\rangle$ where any phase accumulated on the journey to the

target and back is suppressed. Two resonant receiver cavities are placed a distance L apart and connected to a BS and then we perform a QHD at each output as before. The coherent state is split over the two receivers but the lower state acquires a relative phase shift $\phi = k\ell$ due to the path difference $\ell = L\sin(\Theta)$. Here the wavenumber is $k = 2\pi/\lambda$. From this point on the measurement of that phase shift is carried out precisely as before. The resolution of the phase is again $\delta\phi = 1/\sqrt{\bar{n}}$ for $\phi \approx 0$ corresponding to $\Theta \approx 0$ that is a target close to the horizon.

Since L is fixed and known this yields a super-resolved measurement of the altitudinal angle with a resolution approximately equal to

$$\delta\Theta_{\rm Q} \approx \frac{\lambda}{L}\frac{1}{2\pi\sqrt{\bar{n}}}. \tag{4.12}$$

This is a factor of $2\pi\sqrt{\bar{n}}$ smaller than the classical diffraction limit of $\delta\Theta_{\rm C} = \lambda/L$. For $\bar{n} = 100$ average return photons the quantum result is about 60 times smaller than the classical

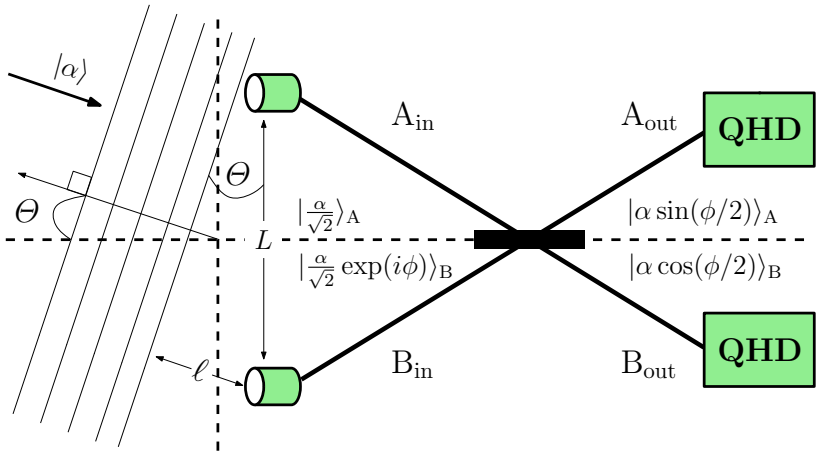

FIGURE 4.5: Here we indicate how to use QHD to extract the super-resolved altitudinal angle Θ. Two resonant radar cavity detectors are placed a distance L apart and connected via a 50:50 BS as shown. The incoming coherent signal $|\alpha\rangle$ arrives as a plane wave and hence the state at the lower cavity experiences a phase shift $\phi = k\ell$ due to the path difference $\ell = L\sin(\Theta)$. Here the wave number is $k = 2\pi/\lambda$. As before the two signals are mixed at the BS and a QHD is performed at each output providing a super-resolved measurement of phase with resolution $\delta\phi = 1/\sqrt{\bar{n}}$. Since L is fixed and known this yields a super-resolved measurement of the altitudinal angle with a resolution approximately equal to $\delta\Theta_{\rm Q} = \lambda/2\pi(L\sqrt{\bar{n}})$ for a target close to the horizon. This is a factor of $2\pi\sqrt{\bar{n}}$ smaller than the classical diffraction limit of $\delta\Theta_{\rm C} = \lambda/L$.

diffraction limit. Rotating the detector system about its bilateral axis allows us to extract the azimuthal phase Φ with the same resolution. These two angular measurements, when combined with the range measurement, completely characterize the instantaneous location of the target. Temporal differentiation of the signal then is performed to acquire the velocity and acceleration.

4.5 Discussion and Conclusion

4.5.1 Discussion on Resolution and Sensitivity

Super-sensitivity (signal-to-noise) below the shot-noise limit is often discussed in the same context of super-resolution (sub-Rayleigh) below the diffraction limit. The reason that these two properties are closely related is that the slope of a super-resolving interference fringe in part determines the sensitivity of the device [16]. Usually the sensitivity can be thought of as the 'fine-grained' version of the resolution.

In the context of quantum imaging and metrology the question arises as to what is the relevant figure of merit when designing a practical system, resolution or sensitivity? For example in coherent quantum lithography, where the Rayleigh diffraction limit rules, the goal is to place features as close together as possible. Therefore resolution is the only relevant figure of merit and discussions of sensitivity never occur. However, in contrast, in the Laser Interferometer Gravitational Wave Observatory (LIGO), they can measure relative arm displacements on the order of an attometer while deploying laser radiation of a wavelength on the order of a micron. That is they are doing 12 orders of magnitude better than the Rayleigh diffraction limit. That community never discusses resolution and only concerns themselves with sensitivity, which currently is at shot-noise for a large range of frequencies.

The LIGO interferometers can perform with such high sensitivity for three reasons. Firstly, in LIGO the gravitational wave causes the arms of the interferometer to change very slowly. Most of the time the gravitational wave is not present and so they can lock the interferometer. Secondly they have a circulating laser power of 100 kW and therefore huge numbers of

photons to work with, about $\bar{n} \approx 10^{20}$ per second in the interferometer. Thirdly they have the luxury to integrate their data over periods of hours, days, and even weeks. In this manner they beat down the noise until the minimal detectable arm displacement is given by the quantum shot-noise expression $\Delta x = \lambda/(2\pi\sqrt{\bar{n}})$, which gives the attometer precision.

A radar ranging system is different from LIGO in that radar operators do not have the luxury to integrate their data over long periods of time. The target speeds of Mach 30 are not uncommon for some applications. Hence the interference fringes are moving very rapidly. There is no time to lock down the interferometer and integrate at these speeds. In addition data integration times are measured in seconds, not hours or days. And finally the number of photons arriving at the detector is very small so there is little data to integrate. The strategy then for coherent lidar and radar is to track the narrowest feature can be found in the interferogram and follow this to establish the range and angular position parameter R, Θ and Φ, and then temporally differentiate these in real time to extract vector velocity and acceleration. It is for these reasons that radar designers often only worry about diffraction rather than sensitivity. It is in such a scenario that we propose the design of our super-resolving quantum radar scheme.

4.5.2 Conclusion

What we have shown in this chapter is that, setting super-sensitivity aside as a goal, it is possible to beat the Rayleigh resolution by an arbitrary amount with coherent state sources and a homodyne implementation of a quantum parity detection scheme [64]. *In the absence of loss*, it is well known that the protocol for producing maximal phase super-resolution is to transmit an entangled state of the electromagnetic field, called a N00N state, in an interferometric set up as shown in Figure 4.1(a) [80]. However, as discussed in Sec. 4.1, several groups have shown that in the presence of high loss the optimal strategy is to transmit coherent states to the target. We then reviewed in Sec. 4.2 that super-resolved ranging is attainable, in Sec. 4.3 how to extract this with homodyne, and then we showed in Sec. 4.4 that altitudinal

and azimuthal angular determination is also possible using a modified homodyne scheme. Given that ordinary radar systems already transmit coherent states of the electromagnetic field, and also given that homodyne detection is a standard radar detection technique (balanced mixer radiometry) our entire proposed quantum radar system can be implemented mostly with commercial-off-the-shelf components with minimal redesign of existing radar systems.

In this chapter as well as in related works [64, 74, 75], we are using the term 'super resolution' in a slightly different fashion than in previous works. In previous work on quantum lithography, super resolution was used to mean many fringes per unit wavelength [57, 58]. This usage explicitly implied narrower fringes in that more fringes per wavelength necessarily implies narrower ones. In this current chapter we restrict the usage to only the narrowing of the fringes. It is clear from Figure 4.3 that the spacing between the fringes is still at the classical wavelength. For coherent interferometric lithography, the increased number of fringes per wavelength is critical to the capability of writing more features N-times closer than is possible classically. However it is not so critical in radar ranging. For radar what is important is that, once we have locked on to a particular fringe, we can tell if the fringe has moved and if so by how much. That sets the resolution, particularly on a rapidly changing range R. The one-dimensional Rayleigh criterion then holds — one can tell if the fringe moves by one full width at half maximum. From Figure 4.3 we see that this distance is classically $\delta x_{\mathrm{C}} = \lambda$ but that in our quantum scheme proposed here it is $\delta x_q = \lambda/(2\pi\sqrt{\bar{n}})$, which is approximately 60 times narrower than the classical result for a return power of 100 photons. It is interesting to note that, since our scheme is also shot-noise limited, that the minimum sensitivity has the same scaling, namely, $\Delta x_q = \lambda/(2\pi\sqrt{\bar{n}})$. However, as we have argued above, in a situation where the target moves quickly, there is little time to integrate data, and the return number of photons is small, that the resolution and not sensitivity is the relevant metric of system performance. One of the most important points to notice for

our proposed scheme is that we have mapped this $1/\sqrt{\bar{n}}$ scaling out of the sensitivity (where it is useless for our application) and into the resolution (where it is critical).

In principle, for complete ranging, we need to have not only narrow fringes but in addition the knowledge of which fringe we are on. Without the latter information we can specify R only modulo a wavelength. This 'which-fringe information can be obtained by using a standard technique in radar ranging. We simply apply a narrow temporal chirp in the outgoing radar beam and time its round trip to the target and back. That then gives us an absolute distance measurement to supply the needed information as to what fringe we are locked on and hence completely determines R. (In practical radar systems one must compensate for changes in the atmospheric index of refraction as a function of distance, altitude, weather, time of day, etc. Such models of the index are well developed and may be deployed here in our scheme with little or no change.)

Finally, even though we have only considered the use of the 'quantum radar system when the return power is very small, our proposal is likely to be useful even at high return powers — the quadrature noise measured in homodyne detection is independent of the excitation of the coherent state. Moreover, in that high-power regime the entire quantum radar system may described within the context of classical radar theory.

In summary, we have presented a quantum radar system with super-resolving ranging and angular determination that is much below the classical Rayleigh diffraction limit. The system will be particularly useful for the radar tracking of far distant and fast moving objects in which little radar power returns to the detector. The system can be implemented using mostly off-the-shelf technologies with only minor modifications to current radar systems.

Chapter 5
Quantum Lithography and SRSP state

Optical lithography is the process of generating patterns, usually very small, on target surfaces by using light sources. Classical lithography is fundamentally limited by the wavelength of the light source. Quantum lithography goes around this limitation by taking advantage of the quantum nature of the light sources. In this chapter, we discuss two protocols for generating super-resolving *single-photon* (SRSP) number-path entangled states from general maximally number-path entangled states, *i.e.*, the N00N states. It is our purpose to show that, contrary to popular belief, a field in a single-photon state *can* carry multifold phase information. We also show that both protocols generate the desired state with different probabilities depending on the type of detectors being used. Such SRSP number-path entangled states preserve high resolving power but lack the requirement of a multiphoton absorbing resist, which may serve as a proof-of-principle prototype for quantum lithography in the future.[1]

5.1 Introduction

With the promising ability to beat the Rayleigh diffraction limit, quantum lithography has drawn a great amount of attention ever since it was first proposed by Boto *et al.* [57]. The original proposal and the experiment realizing quantum lithography [57, 58, 81] exploit the path entanglement of an ensemble of N photons whose de Broglie wavelengths are effectively N times smaller than that of a single photon. However, one of the difficulties of such a scheme is that the arriving quantum-correlated photons are not always concentrated in the same absorption spot [82]. Moreover, an N-photon absorption process requires a multiphoton

[1]Sections 5.3, 5.4 and 5.5 previously appeared as Wei Feng, Kebei Jiang, Michelle L.-J. Lollie, M. Suhail Zubairy, and Jonathan P. Dowling, *Super-resolving single-photon number-path-entangled state and its generation*, Phys. Rev. A, **89**, 043824 (2014). Permission of using it in this dissertation has been granted by the principal author.

absorbing resist [83, 84], and a general trade-off relation between resolution enhancement in quantum lithography and the multiphoton absorption rate has been proved [85]. Therefore, instead of utilizing photon entanglement, several other approaches with non-quantum states of light [86, 87, 88, 89, 90, 91, 92] have been developed, all of which require either a nonlinear material or resonant field-atom interaction.

An N-photon maximally number-path entangled state, which is also known as the N00N state, in a two-path interferometer with a φ phase shift in one path is defined, as in previous chapters, as

$$|N::0\rangle^{N\varphi} \equiv \frac{1}{2}\left(|N,0\rangle + e^{iN\varphi}|0,N\rangle\right). \tag{5.1}$$

The super-resolving power of the N00N state comes from the N-fold relative phase between $|N,0\rangle$ and $|0,N\rangle$.

Generally, only maximally number-path entangled states with the exact form of Eq. (5.1), *i.e.*, with the number of photons equal to the multiplier of the phase, are considered in quantum lithography and metrology. However, a super-resolving single-photon (SRSP) number-path entangled state, which refers to a N00N state with a single photon number but original super-resolving power, can be defined as

$$|1::0\rangle^{N\varphi} \equiv \frac{1}{2}\left(|1,0\rangle + e^{iN\varphi}|0,1\rangle\right). \tag{5.2}$$

Moreover, such a state does not require the aforementioned multiphoton absorbing resist. Consequently, although far from being practical, we believe such a state may lead to a rudimentary design of quantum lithography sources. For the sake of later calculation, we also define a more general N00N state whose super-resolving power is different from its photon number:

$$|N::0\rangle^{M\varphi} \equiv \frac{1}{2}\left(|N,0\rangle + e^{iM\varphi}|0,N\rangle\right). \tag{5.3}$$

The purpose of this chapter is to show how to produce states of Eq. (5.2) from states of Eq. (5.1) by generating the sequence of states of Eq. (5.3), with only linear quantum optical

elements applied. To do so, first we need to show how a high-photon-number N00N state is generated. One of such constructive protocols is proposed by Kok *et al.* in 2002 [93], on which the discussion in next section is based.

5.2 Generation of Maximally Number-Path Entangled States

The generation of low-photon-number N00N ($N = 1$ or 2) states, or low-N00N states, is straightforward. A single-photon N00N state can be produced by injecting a single-photon two-mode state, $|1\rangle_a|0\rangle_b$, into a 50:50 beam splitter (BS). A simple transformation shows the output state to be proportional to $|1\rangle_{a'}|0\rangle_{b'} + |0\rangle_{a'}|1\rangle_{b'}$.

Two-photon N00N state generation depends on the Hong-Ou-Mandel (HOM) effect [94] where a $|1\rangle_a|1\rangle_b$ enters a 50:50 BS. This effect was first proposed to demonstrate the quantum interference between photons from different sources (as opposed to the famous quote, 'photon interferes only with itself', by Dirac) and can be mathematically described as

$$|1\rangle_a|1\rangle_b \xrightarrow{\text{BS}} \frac{1}{\sqrt{2}}\left(|2\rangle_{a'}|0\rangle_{b'} + |0\rangle_{a'}|2\rangle_{b'}\right). \tag{5.4}$$

The lack of cross term, $|1\rangle_{a'}|1\rangle_{b'}$, can be explained in Figure 5.1. The probability amplitudes of the two possible 'paths' of transition $|1\rangle_a|1\rangle_b \xrightarrow{\text{BS}} |1\rangle_{a'}|1\rangle_{b'}$ completely cancel each other, *i.e.*, destructively interfere with each other.

Unfortunately this cancellation does not generalize beyond $N = 2$ for there are not enough free parameters available to suppress high-N cross terms. However, with the cost of more complicated setup and lower generation efficiency, Kok *et al.* proposed a protocol of gener-

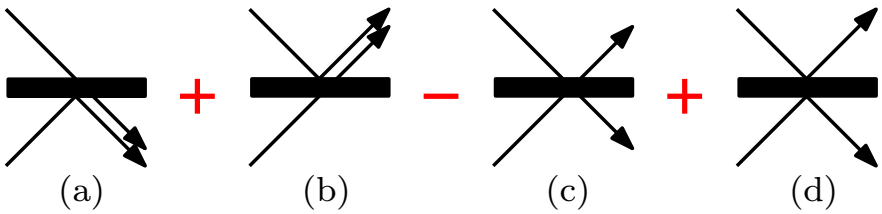

FIGURE 5.1: Four possible outputs of a $|1, 1\rangle$ input. (c) represents a double transmission with probability amplitude $(i)(i) = -1$; (d) represents a double reflection with probability amplitude $(-1)(-1) = 1$. Both (c) and (d) lead to the same cross terms, therefore they cancel each other completely.

ating high-N00N states ($N \geq 3$) from a $|N, N\rangle$, which is based on repeated implementation of HOM effect. Other proposals on high-N00N state generation, all of which involve strong Kerr nonlinearity or adding ancillary BS's and detectors, are reviewed in Ref. [16]. More recently, a 'High-N00N' state with N up to five has been generated in the lab [95].

The basic element of Kok's protocol is shown in Figure 5.2, where two BS's peel off photons from incident beams a and b. The reflected modes are recombined at the 50:50 BS in the middle and a coincidence detection is carried out on both of the output modes c' and d'. If one of the incident photons is from mode a and the other is from b, then from Eq. 5.4 we will have a $|2 :: 0\rangle_{c',d'}$ as the output, where a coincidence will never be detected. On the other hand, if both photons are from mode a or b, the inverse of Eq. 5.4 guarantees a coincidence at the output. Therefore, by post-selecting on a two fold coincidence in the output modes c' and d', and considering the tunable phase shift φ, the outgoing state in modes a' and b' becomes $|N_a - 2, N_b\rangle + e^{-2i\varphi}|N_a, N_b - 2\rangle$, given the incoming state in modes a and b is $|N_a, N_b\rangle$.

Kok *et al.* stated that *an even photon-number $|N :: 0\rangle$ can be generated by stacking $N/2$ of such basic elements, with a $|N, N\rangle$, which is much easier to produce than its corresponding N00N state, as the incoming state of the first basic element.* This scheme is shown in Fig-

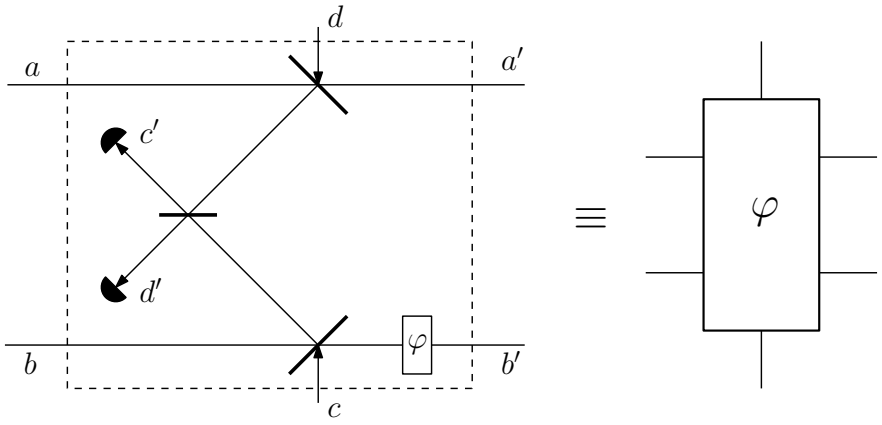

FIGURE 5.2: The basic element of Kok's protocol of high-N00N state generation. Two photons are peeled off from incident beams a and b, which are later subjected to a coincident detection at c' and d'. The tunable phase shift φ are required to eliminate all cross terms in the output states.

ure 5.3. To prove this statement, we can write the action of each basic element as $a^2 + e^{i\varphi} b^2$. Then the statement under consideration is equivalent to

$$\prod_{k=1}^{N/2} (a^2 + e^{i\varphi_k} b^2) |N, N\rangle = |N :: 0\rangle. \tag{5.5}$$

Therefore we require $\prod_{k=1}^{N/2} (a^2 + e^{i\varphi_k} b^2) \propto \left(a^N + b^N\right)$ and the values of the phase shifts become

$$\varphi_k = \ 4\pi k/N.$$

The generation of odd photon-number high-N00N states can be accomplished in mostly the same way with the introduction of a polarization BS. After applying a phase shift φ to the out-coming state of Figure 5.3, we obtain a $|N :: 0\rangle^{N\varphi}$ defined in Eq. (5.1).

5.3 Which-Way Information and Quantum Eraser

In this section we discuss in detail the effect of the extra BS on a incoming N00N state. We show that the acquisition of which-way information destroys the phase-resolving power of the $|N :: 0\rangle^{N\varphi}$. For pedagogical reasons, we start with $|2 :: 0\rangle^{2\varphi}$ as the input state before the BS in Figure 5.4. Assuming the two BSs have the same transmittance t and reflectance r, and from the standard quantum transformation [4]

$$a^\dagger = ta'^\dagger + irc^\dagger, \quad b^\dagger = tb'^\dagger + ird^\dagger, \tag{5.6}$$

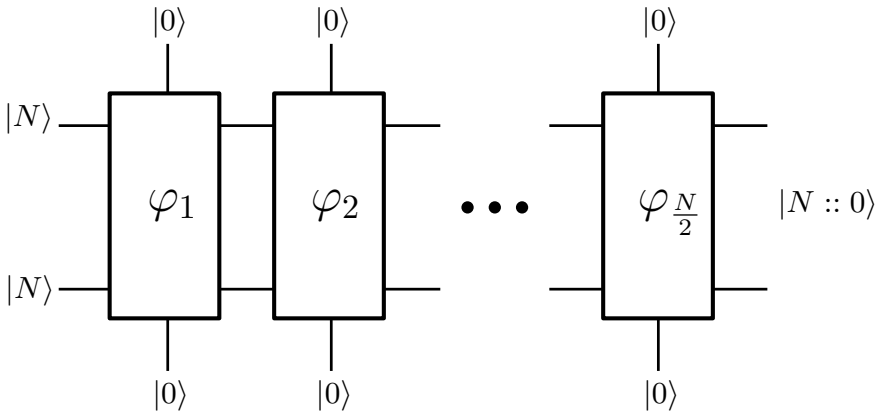

FIGURE 5.3: The repeated use of the basic element defined in Figure 5.2 will transform a $|N, N\rangle$ into a $|N :: 0\rangle$.

it is straightforward to calculate the probabilities of transmitting all possible states to a' and b', and the result is shown in Table 5.1. Notice that because of the availability of the which-way information of the incoming photon, the chance of transmitting $|1::0\rangle^{2\varphi}$ is zero.

If an extra 50:50 BS is introduced as in Figure 5.5, the information regarding which path (mode c' or d') the detected photons come from would be hidden from the environment. Therefore photons are subtracted coherently from the original state (modes a and b) and the relative phase is preserved in the transmitted state (modes a' and b'). The detection probabilities change accordingly and are shown in Table 5.2. Note that even though states such as $1/\sqrt{2}\left(|1,0\rangle_{a',b'} - ie^{i2\varphi}|0,1\rangle_{a',b'}\right)$ and $1/\sqrt{2}\left(|1,0\rangle_{a',b'} + ie^{i2\varphi}|0,1\rangle_{a',b'}\right)$ are single-photon states

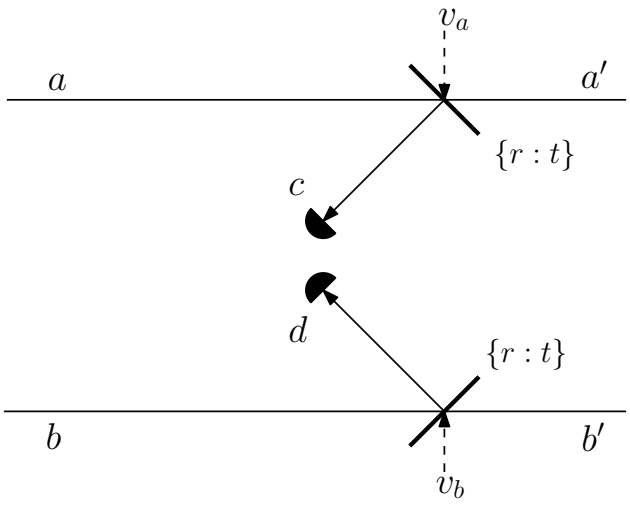

FIGURE 5.4: Two BS's with the same reflectance $\rho = r^2$ are employed to reduce the number of the photons being transmitted. The existence of detectors c and d reveals the which-way information of the reflected photons and the incoming N00N states in modes a and b collapse into a separable state in mode a' or b'. Therefore the relative phase is lost and the phase-resolving power is destroyed.

TABLE 5.1: Probabilities without quantum eraser, as shown in Figure 5.4.

Detector state	Transmitted state	Probability
$\|0,0\rangle_{d,c}$	$t^2\left(\|2,0\rangle_{a',b'} + e^{i2\varphi}\|0,2\rangle_{a',b'}\right)/\sqrt{2}$	t^4
$\|0,1\rangle_{d,c}$	$itr\|1,0\rangle_{a',b'}$	t^2r^2
$\|0,2\rangle_{d,c}$	$-r^2\|0,0\rangle_{a',b'}/\sqrt{2}$	$r^4/2$
$\|1,0\rangle_{d,c}$	$e^{i2\varphi}itr\|0,1\rangle_{a',b'}$	t^2r^2
$\|2,0\rangle_{d,c}$	$-e^{i2\varphi}r^2\|0,0\rangle_{a',b'}/\sqrt{2}$	$r^4/2$

and preserve the twofold phase-resolving power, they are, in general, not valid output states because of the extra i in the relative phase. However, we can apply certain phase shifts to make such states usable, which is discussed in later sections. Moreover, quantum interference is observed when all photons are reflected into the 50:50 BS and the corresponding probabilities vary as a function of the phase shift φ, as would be expected from a lossless Mach-Zehnder interferometer.

In conclusion, a 'quantum eraser' is necessary to generate a SRSP number-path entangled state, and we refer to the setup shown in Figure 5.5 as a 'unit' since it is used repeatedly

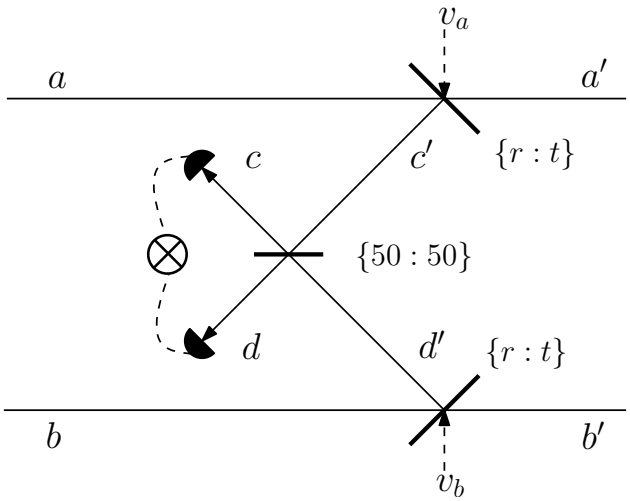

FIGURE 5.5: A single "unit": Figure 5.4 plus an extra 50:50 BS which erases the which-way information; the relative phase is preserved at the output. The dashed lines connecting detectors c and d represents the fact that coincidence detection is only needed under certain circumstances which will be specified in later sections. On the other hand, the 50:50 BS is always necessary.

TABLE 5.2: Probabilities with quantum eraser, as shown in Figure 5.5.

Detector state	Transmitted state	Probability
$\|0,0\rangle_{d,c}$	$t^2\left(\|2,0\rangle_{a',b'} + e^{i2\varphi}\|0,2\rangle_{a',b'}\right)/\sqrt{2}$	t^4
$\|0,1\rangle_{d,c}$	$-tr\left(\|1,0\rangle_{a',b'} - ie^{i2\varphi}\|0,1\rangle_{a',b'}\right)/\sqrt{2}$	t^2r^2
$\|0,2\rangle_{d,c}$	$r^2(1-e^{i2\varphi})\|0,0\rangle_{a',b'}/2\sqrt{2}$	$r^4\sin^2\varphi/2$
$\|1,0\rangle_{d,c}$	$itr\left(\|1,0\rangle_{a',b'} + ie^{i2\varphi}\|0,1\rangle_{a',b'}\right)/\sqrt{2}$	t^2r^2
$\|2,0\rangle_{d,c}$	$-r^2(1-e^{i2\varphi})\|0,0\rangle_{a',b'}/2\sqrt{2}$	$r^4\sin^2\varphi/2$
$\|1,1\rangle_{d,c}$	$-ir^2(1+e^{i2\varphi})\|0,0\rangle_{a',b'}/2$	$r^4\cos^2\varphi$

in the following calculation. In addition, with a general $|N :: 0\rangle^{M\varphi}$ as the input state, the probability of detecting a $|m,n\rangle_{d,c}$ in a unit is shown to be

$$\begin{aligned} & P_N^{M\varphi}(m,n,\rho) \\ &= |_{d,c}\langle m,n|\psi_{\text{total}}\rangle|^2 \\ &= \binom{N}{m+n}(1-\rho)^{N-(m+n)}\rho^{m+n}\binom{m+n}{m}\left(\frac{1}{2}\right)^{m+n} \\ &\quad \times\left\{1+\delta_{N,m+n}\cos\left(M\varphi+\frac{(m-n)\pi}{2}\right)\right\}. \end{aligned} \tag{5.7}$$

Here $\rho = r^2$, $1-\rho = t^2$, and $|\psi_{\text{total}}\rangle$ is the full output state in modes a', b', d, and c. In the last line of the previous equation, the expression $\binom{N}{m+n}(1-\rho)^{N-(m+n)}\rho^{m+n}$ comes from reflecting $m+n$ photons out of N photons from the $\{r,t\}$ BS's while $\binom{m+n}{m}\left(\frac{1}{2}\right)^{m+n}$ is from the 50:50 BS. The $\delta_{N,m+n}\times\cos$ term reflects the quantum interference when none of the N photons are transmitted.

5.4 Generation of $|1 :: 0\rangle^{N\varphi}$ without Number-Resolving Detectors

With ordinary photodetectors we are only able to tell whether or not any photon arrives at the detector, but not how many of them. Consequently, how many photons are reflected in a single unit is unknown. Therefore we introduce a stacking of units, implementing coincidence detection in each one to enhance the probability of generating the correct state.

To see how the coincidence detection is beneficial, we consider the example where the input of a unit is $|3 :: 0\rangle^{3\varphi}$. We take into account two probabilities. With the first probability, it is easy to see that there are ten possible detected states, and only when a $|1,1\rangle_{d,c}$ is detected do we generate the $|1 :: 0\rangle^{3\varphi}_{a',b'}$. This is a direct result from the HOM effect [94, 96]. With the second probability, if we perform coincidence detection and take the output states only when both c and d click, the chance of $|1,1\rangle_{d,c}$ being detected is much higher, since there are only two other coincidence states: $|2,1\rangle_{d,c}$ and $|1,2\rangle_{d,c}$. We call the former the "probability of detecting some state" and the latter the "conditional probability of detecting some state". Both kinds of probabilities are discussed in the following calculations.

5.4.1 Odd-Photon-Number Input State

For a general input state $|N_{\rm o} :: 0\rangle^{N_{\rm o}\varphi}$ with $N_{\rm o} \equiv N_l = 2l+1,\ l = 1, 2, 3, ...$, we need l units to generate the desired output $|1 :: 0\rangle^{N_{\rm o}\varphi}$, as shown in Figure 5.6. The procedure is as follows: *we propagate the input state from lth unit, which is at the leftmost, to the first unit, which is to the immediate left of the output, and for each unit i we only pass on those cases where a coincidence between d and c is detected* (*see Figure 5.5*). This ensures that, in each unit, at least two photons are subtracted from the input state while the multifold relative phase $e^{iN_{\rm o}\varphi}$ is intact. This is exactly what is needed to generate a SRSP number-path entangled state from a general maximally number-path entangled state.

On the other hand, such a procedure has a low efficiency. The reason is that any state that loses more than three photons in any unit will not be propagated to the output because it has to lose one photon or none at all (*i.e.*, no coincidence) in some other units to compensate for excess photon loss. Therefore there are only two possible output states: (a) $|1 :: 0\rangle$, where every unit subtracts two photons, *i.e.*, $|1,1\rangle_{d,c}$ is detected in each unit, and (b) $|0 :: 0\rangle$, where one of the units subtracts three photons, *i.e.*, $|1,2\rangle_{d,c}$ or $|2,1\rangle_{d,c}$ is detected, and all others subtract two photons.

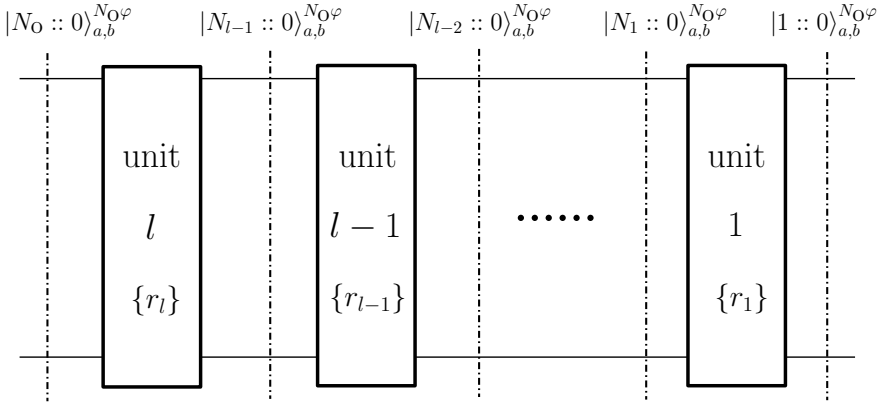

FIGURE 5.6: A stacking of units to reduce a $|N_{\rm o} :: 0\rangle^{N_{\rm o}\varphi}$, with $N_{\rm o} = 2l+1$ being an odd number. Each rectangle represents the unit described in Figure 5.5. Notice we count from the output for the ease of calculation. Unit i with a reflectance of r_i is the ith last unit before the output. It has a N00N state $|N_i :: 0\rangle^{N_{\rm o}\varphi}$ as the input state. Note that although the number of photons decreases from left to right, the relative phase is always $N_{\rm o}\varphi$, which is exactly what we need to generate a SRSP number-path entangled state.

For scenario (a), the probability can be calculated as

$$\begin{aligned} P^{N_{\rm o}}_{\text{all }|1,1\rangle} &= \prod_{k=1}^{l} P^{N_{\rm o}\varphi}_{2k+1}(1,1,\rho_k) \\ &= \prod_{k=1}^{l} \frac{1}{2}k(2k+1)(1-\rho_k)^{2k-1}\rho_k^2. \end{aligned} \tag{5.8}$$

For scenario (b), we first show that the probability of detecting $|1,2\rangle_{d,c}$ in the ith unit while $|1,1\rangle_{d,c}$ is detected in all others is

$$P^{N_{\rm o}}_{i\text{th }|1,2\rangle} = \begin{cases} P^{N_{\rm o}}_{\text{all }|1,1\rangle}\frac{\rho_1(1+\sin(N_{\rm o}\varphi))}{4(1-\rho_1)}, & i=1; \\ P^{N_{\rm o}}_{\text{all }|1,1\rangle}\frac{\rho_i(1+\cos(N_{\rm o}\varphi))}{4(1-\rho_i)}\prod_{k=1}^{i-1}\frac{1}{1-\rho_k}, & \text{otherwise.} \end{cases} \tag{5.9}$$

The sum of all possible units for which $|1,2\rangle_{d,c}$ is detected becomes $P^{N_{\rm o}}_{\text{one }|1,2\rangle} = \sum_{i=1}^{l} P^{N_{\rm o}}_{i\text{th }|1,2\rangle}$. Similarly, we have that the probability of detecting $|2,1\rangle_{d,c}$ in the ith unit while $|1,1\rangle_{d,c}$ is detected in all others is

$$P^{N_{\rm o}}_{i\text{th }|2,1\rangle} = \begin{cases} P^{N_{\rm o}}_{\text{all }|1,1\rangle}\frac{\rho_1(1-\sin(N_{\rm o}\varphi))}{4(1-\rho_1)}, & i=1; \\ P^{N_{\rm o}}_{\text{all }|1,1\rangle}\frac{\rho_i(1+\cos(N_{\rm o}\varphi))}{4(1-\rho_i)}\prod_{k=1}^{i-1}\frac{1}{1-\rho_k}, & \text{otherwise,} \end{cases} \tag{5.10}$$

and $P^{N_{\rm o}}_{\text{one }|2,1\rangle} = \sum_{i=1}^{l} P^{N_{\rm o}}_{i\text{th }|2,1\rangle}$. Now the conditional probability of transmitting $|1::0\rangle^{N_{\rm o}\varphi}$ after unit 1, given the photon number of the input state is odd and coincidence detection is employed in every unit, becomes

$$\begin{aligned} & P^{N_{\rm o}}_{\text{cond.}} \\ &= \frac{P^{N_{\rm o}}_{\text{all }|1,1\rangle}}{P^{N_{\rm o}}_{\text{all }|1,1\rangle} + P^{N_{\rm o}}_{\text{one }|1,2\rangle} + P^{N_{\rm o}}_{\text{one }|2,1\rangle}} \\ &= \frac{1}{\displaystyle\sum_{i=2}^{l}\frac{(1+\cos(N_{\rm o}\varphi))\rho_i}{2(1-\rho_i)}\prod_{k=1}^{i-1}\frac{1}{1-\rho_k} + \frac{2-\rho_1}{2(1-\rho_1)}}. \end{aligned} \tag{5.11}$$

The probability of generating $|1::0\rangle^{N_{\rm o}}$ can be maximized by choosing an optimal reflectance ρ_k for the kth unit. Physically, it is easy to show from Eq. (5.8) that this probability

maximizes when $\rho_k = 2/(2k+1)$ (*i.e.*, the most probable number of photons being reflected in each unit is two) and

$$P^{N_o}_{\text{all }|1,1\rangle}|_{\max} = \prod_{k=1}^{l} \frac{2k}{2k-1}\left(\frac{2k-1}{2k+1}\right)^{2k} = \frac{N_o!}{{N_o}^{N_o}} \tag{5.12}$$

$$\approx \sqrt{2\pi N_o} e^{-N_o}, \tag{5.13}$$

where in the last line Sterling's formula is used in the large N_o limit. [2] This probability decreases exponentially with increasing N_o, as expected.

On the other hand, there is no optimal $\rho_k \in [0,1]$ that leads to a maximal conditional probability; $P^{N_o}_{\text{cond.}}$ in Eq. (5.11) is independent of $P^{N_o}_{\text{all }|1,1\rangle}$ and approaches unity when all ρ_k are close to zero. However, we can set a critical conditional probability $P^{N_o}_{\text{cond.}}|_c$ and compute the corresponding ρ_k. Assuming $N_o = 7$, $\varphi = \pi/14$, all ρ_k are equal to ρ_c, and we want a 50% chance of transmitting a $|1::0\rangle^{7\varphi}$ state whenever a coincidence is detected in unit 1, *i.e.*, $P^{N_o}_{\text{cond.}}|_c = 0.5$, then ρ_c can be calculated to be around 0.31; when $P^{N_o}_{\text{cond.}}|_c = 0.9$, $\rho_c \approx 0.06$.

However, this does not mean that we can obtain more outputs by decreasing the reflectance. In previous example, the probability of generating $|1::0\rangle$ is $P^{N_o}_{\text{all }|1,1\rangle} = 0.2\%$ when $\rho = 0.31$ and almost zero when $\rho = 0.06$. Therefore a higher conditional probability (*i.e.*, higher fidelity) comes with a lower probability (*i.e.*, efficiency), and vice versa [93].

5.4.2 Even-Photon-Number Input State

For a general input state $|N_e::0\rangle^{N_e\varphi}$ with $N_e = 2l,\ l = 1,2,3...$, we need l units to generate the desired output $|1::0\rangle^{N_e\varphi}$, as shown in Figure 5.6. The procedure is as follows: *we propagate the input state from lth unit, which is at the leftmost, to the second unit, which is to the immediate left of the first unit, and for each unit i ($i \in [2,l]$) we only pass on*

[2] In the general case, for each of the N_o photons there are $2l+1$ possible ways of being reflected (there are two paths in each of the l units and one accounts for the case where no reflection occurs), which explains the denominator in Eq. (5.12). On the other hand, when only two photons are expected to be reflected in a unit with a input state $|N::0\rangle$, the number of possible ways of such reflection is $2\binom{N}{2}$. Therefore the total number of possible reflections in this case is $\prod_{k=1}^{l} 2\binom{N_k}{2} = \prod_{k=1}^{N_o}\binom{k}{1} = N_o!$, which is the numerator of Eq. (5.12).

those cases where a coincidence between d and c (see Figure 5.5) is detected; in the first unit, however, we do photodetection on both d and c but no coincidence counting. Whenever d (c) clicks, we apply a $-\pi/2$ ($\pi/2$) phase shift on mode b'. This ensures that in each unit from l to 2, at least two photons are subtracted from the input state while the multifold relative phase $e^{iN_o\varphi}$ is intact.

Similar to the odd-number case, there are only two possible input states for unit 1: (a) $|2::0\rangle$, where every unit from the second to the lth subtracts two photons, *i.e.*, $|1,1\rangle_{d,c}$ is detected in each unit, and (b) $|1::0\rangle$, where one of the other units subtracts three photons, *i.e.*, $|1,2\rangle_{d,c}$ or $|2,1\rangle_{d,c}$ is detected, and all others subtract two photons. Moreover, from Table 5.2, it is easy to see that a single click in d corresponds to $1/\sqrt{2}(|1,0\rangle_{a',b'} + ie^{iN_e\varphi}|0,1\rangle_{a',b'})$ being transmitted, and a $-\pi/2$ phase shift on b' turns it into $|1::0\rangle^{N_e\varphi}$. Similar logic applies to a single click in c.

For scenario (a), the probability of having $|2::0\rangle^{N_e\varphi}$ as the input of unit 1 is

$$\begin{aligned} P^{N_e}_{\text{all }|1,1\rangle} &= \prod_{k=2}^{l} P^{N_e\varphi}_{2k}(1,1,\rho_k) \\ &= \prod_{k=2}^{l} \frac{1}{2}k(2k-1)(1-\rho_k)^{2(k-1)}\rho_k^2. \end{aligned} \tag{5.14}$$

The probability of detecting only one photon in unit 1 with this input state can be easily read off from Table 5.2 as $2t_1^2r_1^2 = 2(1-\rho_1)\rho_1$. Therefore the probability of transmitting the correct state at the output is

$$2P^{N_e}_{\text{all }|1,1\rangle}(1-\rho_1)\rho_1. \tag{5.15}$$

For scenario (b), we first show that the probability that $|1,2\rangle_{d,c}$ is detected in the ith unit while $|1,1\rangle_{d,c}$ is detected in all others is

$$P^{N_e}_{i\text{th }|1,2\rangle} = P^{N_e}_{\text{all }|1,1\rangle}\frac{\rho_i}{2(1-\rho_i)}\prod_{k=2}^{i-1}\frac{1}{1-\rho_k}. \tag{5.16}$$

The sum of all possible units for which $|1,2\rangle_{d,c}$ is detected becomes $P^{N_e}_{\text{one }|1,2\rangle} = \sum_{i=2}^{l} P^{N_e}_{i\text{th }|1,2\rangle}$. Because of symmetry, we have $P^{N_e}_{i\text{th }|2,1\rangle} = P^{N_e}_{i\text{th }|1,2\rangle}$ and $P^{N_e}_{\text{one }|2,1\rangle} = P^{N_e}_{\text{one }|1,2\rangle}$.

Now we are in the position to calculate the conditional probability of transmitting $|1::0\rangle^{N_e\varphi}$ in the case of an even-photon-number input state, given a coincidence is detected in unit 2 to unit l and either d or c (but not both) in unit 1 clicks:

$$\begin{aligned} P_{\text{cond.}}^{N_e} &= \frac{2P_{\text{all }|1,1\rangle}^{N_e}(1-\rho_1)\rho_1}{P_{\text{all }|1,1\rangle}^{N_e}\left\{2-\rho_1\left(1+\cos^2\left(\frac{N_e}{2}\varphi\right)\right)\right\}\rho_1+\left(P_{\text{one }|1,2\rangle}^{N_e}+P_{\text{one }|2,1\rangle}^{N_e}\right)\rho_1} \\ &= \frac{2(1-\rho_1)}{2-\rho_1\left(1+\cos^2\left(\frac{N_e}{2}\varphi\right)\right)+\sum_{i=2}^{l}\frac{\rho_i}{1-\rho_i}\prod_{k=2}^{i-1}\frac{1}{1-\rho_k}}. \end{aligned} \tag{5.17}$$

The $\{2-\rho_1\left[1+\cos^2\left(N_e\varphi/2\right)\right]\}$ in the denominator represents the probability of getting one click in unit 1 given its input is a $|2::0\rangle^{N_e\varphi}$ state, while ρ_1 represents that of an input state of $|1::0\rangle^{N_e\varphi}$.

From Eqs. (5.14) and (5.15), the probability of generating $|1::0\rangle^{N_e\varphi}$ can be maximized by choosing an optimal reflectance ρ_k for the kth unit. Physically, it is easy to show that $P_{\text{all }|1,1\rangle}^{N_e}$ maximizes when $\rho_k = 1/k$ and

$$\begin{aligned} P_{\text{all }|1,1\rangle}^{N_e}|_{\max} &= \prod_{k=2}^{l}\frac{2k-1}{2k}\left(\frac{k-1}{k}\right)^{2(k-1)} \\ &= 2\frac{N_e!}{{N_e}^{N_e}} \qquad (5.18) \\ &\approx 2\sqrt{2\pi N_e}e^{-N_e}, \qquad (5.19) \end{aligned}$$

where in the last line Sterling's formula is used in the large N_e limit. It is easy to show that the expression $2(1-\rho_1)\rho_1$ in Eq. (5.15) has a maximal value of $1/2$ when $\rho_1 = 1/2$. Therefore the maximum probability of transmitting the correct state is $N_e!/{N_e}^{N_e}$, which agrees with Eq. (5.12) and can be reached when the reflectance of the units are such that

$$\rho_k = \begin{cases} 1/k, & k \in [2, N_e/2]; \\ 1/2, & k = 1. \end{cases} \tag{5.20}$$

On the other hand, there is no optimal $\rho_k \in [0,1]$ that leads to a maximal conditional probability in Eq. (5.17). Just like in the case with the odd-photon-number input state, we

may set a critical probability and require the corresponding ρ_k, and the reciprocal relation between fidelity and efficiency stands as well.

5.5 Generation of $|1::0\rangle^{N\varphi}$ with Number-Resolving Detectors

With number-resolving detectors implemented at d and c in Figure 5.5, we are able to tell how many photons are reflected in a unit [97, 98]. Therefore it is much easier to generate a $|1::0\rangle^{N\varphi}$ state from a general $|N::0\rangle^{N\varphi}$ state: only a single unit is needed. The protocol is as follows: *assuming m and n photons are detected at d and c in a single unit with reflectance ρ, we (a) propagate the state to the output only when $m+n=N-1$, and (b) given (a) is true, we apply a $(n-m)\pi/2$ phase shift on mode b'.* This protocol can be easily derived.

A general input N00N state in Figure 5.5 is

$$|\psi_{\text{in}}\rangle = \frac{1}{\sqrt{2}}\left(|N,0;0,0\rangle_{a,v_a;b,v_b} + e^{iN\varphi}|0,0;N,0\rangle_{a,v_a;b,v_b}\right), \tag{5.21}$$

where N can be either odd or even. The corresponding output state at a', b', c', and d' is

$$|\psi_{\text{out}}\rangle = \sum_{k=0}^{N}\binom{N}{k}^{1/2} t^k (ir)^{N-k}\frac{1}{\sqrt{2}}(|k,0;N-k,0\rangle_{a',b';c',d'} + e^{iN\varphi}|0,k;0,N-k\rangle_{a',b';c',d'}). \tag{5.22}$$

Given we are only interested in transmitting one photon to the output, states in $|\psi_{\text{out}}\rangle$ with $k\neq 1$ can be ignored and we are left with

$$|\psi_{\text{target}}\rangle = \frac{\sqrt{N}}{\sqrt{2}} t(ir)^{N-1}\left(|1,0\rangle_{a',b'}\otimes|N-1,0\rangle_{c',d'} + e^{iN\varphi}|0,1\rangle_{a',b'}\otimes|0,N-1\rangle_{c',d'}\right). \tag{5.23}$$

Since $|k,0\rangle_{c',d'} \to \left(\frac{1}{\sqrt{2}}\right)^k \sum_{m=0}^{k}\binom{k}{m}^{\frac{1}{2}} i^n |m,n\rangle_{d,c}$ and $|0,k\rangle_{c',d'} \to \left(\frac{1}{\sqrt{2}}\right)^k \sum_{m=0}^{k}\binom{k}{m}^{\frac{1}{2}} i^m |m,n\rangle_{d,c}$, with $k=N-1$ Eq. (5.23) becomes

$$|\psi_{\text{target}}\rangle = \sqrt{N}t\left(\frac{ir}{\sqrt{2}}\right)^{N-1}\sum_{m=0}^{N-1}\binom{N-1}{m}^{\frac{1}{2}} i^n \left(\frac{|1,0\rangle_{a',b'} + i^{m-n}e^{iN\varphi}|0,1\rangle_{a',b'}}{\sqrt{2}}\right)\otimes|m,n\rangle_{d,c}. \tag{5.24}$$

The state in the last set of parentheses is a $|1::0\rangle^{N\varphi}$ state with an extra phase of $(m-n)\pi/2$, which can be corrected by applying an $(n-m)\pi/2$ phase shift on mode b'. This allows us

to keep all transmitted states with such detected photon numbers m and n in modes d and c so that $m + n = N - 1$. In contrast, there are always faulty transmitted states when only coincidence detection is available.

From Eqs. (5.22) and (5.23), the probability of transmitting the correct state with photon-number-resolving detectors is

$$P^N_{\text{resolving}} = |\langle\psi_{\text{target}}|\psi_{\text{out}}\rangle|^2 = N(1-\rho)\rho^{N-1}, \tag{5.25}$$

where $\rho = r^2$ as before. This probability maximizes at $\rho = r^2 = (N-1)/N$, with

$$P^N_{\text{resolving}}|_{\max} = \left(\frac{N-1}{N}\right)^{N-1} \tag{5.26}$$

$$\approx e^{-1}, \tag{5.27}$$

where in the last line we take the limit of large N.

In Figure 5.7 we plot the probabilities for protocols with and without number-resolving detectors. It is easy to see that with photon-number-resolving detectors, a SRSP number-path entangled state is much more likely to be generated from a general N00N state. Moreover, since we have complete control over the state being transmitted, the conditional probability with photon number-resolving detectors is always 1.

5.6 Conclusion and Discussion

In this chapter, we have proposed two protocols for generating a SRSP number-path entangled state $|1 :: 0\rangle^{N\varphi}$ from a general N-photon N00N state, either with or without photon-number-resolving detectors. On one hand, both protocols require an extra 50:50 BS on top of a general two-path interferometer to cloak the which-way information of the reflected photons to maintain the coherence of the transmitted states. On the other hand, the generation of $|1 :: 0\rangle^{N\varphi}$ without photon-number-resolving detectors has to be realized in $\lfloor N/2 \rfloor$ steps, whereas that with photon-number-resolving detectors can be done in one step since we have full knowledge of the detected photon numbers. In addition, we have shown that both the

probability (efficiency) and conditional probability (fidelity) of generation are higher when photon-number-resolving detectors are involved. In the case with non-resolving detectors we can achieve arbitrarily high fidelity, but at the cost of low efficiency.

One remaining issue is the effect of the imperfection of the detectors. Following the same argument as in Ref. [93], we may ignore the deteriorated efficiency and dark counts because of the short operation-time windows, and consider only the imperfect detection efficiency of the detectors. First, we consider the case without photon-number-resolving detectors and assume all detectors are the same. From previous footnote it is easy to see that the numerator of Eq. (5.12) now becomes $N_{\rm o}!\eta^{N_{\rm o}}$, where η is the detector efficiency and $\eta^{N_{\rm o}}$ is the probability that each of the $N_{\rm o}$ detectors clicks accurately. Thus this protocol performs exponentially poorly when detector efficiency is not unity. With photon-number-resolving detectors, since only two detectors (one unit) are involved, the effect of detector efficiency scales as η^2, which is independent of the number of input photon.

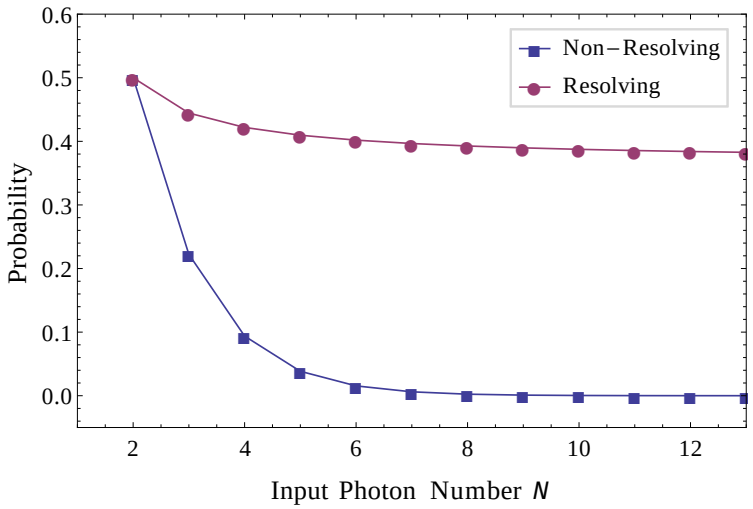

FIGURE 5.7: The maximized probabilities of transmitting a $|1 :: 0\rangle^{N\varphi}$ state following different protocols (see Eqs. (5.12), (5.18) and (5.26)) are plotted as a function of the input photon number. The squares represent the probabilities for a general input state such as in Eq. (5.3) without photon-number-resolving detections, while the circles represent the probabilities with photon-number-resolving detections. It is clear that with increasing the input photon number, number-resolving detection maintains around 40% efficiency, while coincidence detection drops to zero rapidly. This means that with the right kind of detector and an efficient way of generating the N00N state, we can generate the SRSP state efficiently!

We conclude this chapter with the remark that the SRSP number-path entangled state proposed here is far from practical for quantum lithography at the current stage. It might, however, inspire some new perspective for this field of research.

Chapter 6
Squeezed Vacuum and Polarization SR

6.1 Introduction

As shown in Chap. 1, the noise in one of the two quadratures of a squeezed state can be lower than the SNL. This directly leads to the application of squeezed states in quantum interferometry. Caves first pointed out that the use of squeezed light source can improve the sensitivity of an interferometer [13]. The Laser Interferometer Gravitational Wave Observatory (LIGO), which aims to directly detect passing gravitational waves, will use a squeezed light source to achieve extreme precision in its next generation. Although the LIGO is very expensive and takes weeks to be aligned, it is basically nothing more than a huge optical interferometer, whose sensitivity relies on the right choice of state for the light source. As another example, light source in squeezed vacuum state could be used to design a new type of optical magnetometer with noise level 3 dB lower than SNL [99]. While the surpassing superconducting quantum interference device (SQUID) magnetometer is very expensive to operate, the new design based on squeezing is very simple and costs no more than a milliwatt pump laser. A detailed review of squeezed states may be found in Ref. [100].

Many schemes for generating squeezed states have been proposed ever since its discovery. Yuen *et al.* first proposed that squeezed light could be produced by using four-wave mixing (4WM) [101, 102]. Later Caves and Schumaker developed a two-photon formalism for a squeezed state and suggested several nonlinear processes for its generation [103, 104]. In this chapter, we focus on the phenomenon called polarization self-rotation (SR) and its application in creating squeezed vacuum states. There are two major advantages of this protocol. First, polarization SR is relatively simple to realize under modest experimental conditions at room temperature. Second, squeezing via polarization SR can be generated at a low frequency with a narrow bandwidth. For a more comprehensive summary of experimental

efforts in generating squeezed state, especially on polarization SR, readers are referred to the dissertation by Horrom [105].

When an elliptically polarized light field interacts with a nonlinear medium, it introduces circular birefringence (polarization dependent refractive index) into the medium, which in turn cause the polarization ellipse of the light field to rotate. This process is known as the polarization SR and such nonlinear media are called the SR media. Various mechanisms (such as Kerr nonlinearity or ac-Stark shift) are responsible for this effect dependent upon the nonlinear media used. The nonlinear system studied in this chapter is the ^{87}Rb atomic vapor, in which self-rotation is induced by optical pumping and ac-Stark shift [106].

It has been demonstrated, both theoretically and experimentally, that when linearly polarized light propagates through a SR medium, the light in the orthogonal polarization will be in a squeezed vacuum state. However, such vacuum squeezing can be difficult to accomplish in a generic Kerr medium when absorption is present. The atomic system, on the other hand, is believed to be more efficient under resonant conditions, where a high degree of SR and small degree of absorption is achievable [107].

In following sections, we first discuss the level structure of the ^{87}Rb atoms and argue that under certain parametric configurations it can be simplified as a four-level system. Then we provide a simple calculation verifying polarization SR in such a four-level system when an elliptically polarized light field is injected. Later we try to quantify the degree of squeezing in the vacuum mode of the system when a linearly polarized light is used. We first consider the work by Matsko *et al.* [107] where squeezing levels up to 8 dB in a SR atomic system is first predicted. However, this work is based on an analogy to the classical solution and the field is treated classically. Therefore, in the later section, we calculate the degree of vacuum squeezing in the vacuum mode of a fully quantized light field interacting with the simplified four-level system. Our simulation in Section 6.4.3 shows no vacuum squeezing. Finally, we

consider the fluorescence power spectrum of the radiation field at the far-zone and show that vacuum squeezing in some quadrature is achieved.

6.2 ^{87}Rb and $1/2 \rightarrow 1/2$ System (X-system)

Rubidium is an alkaline element with atomic number 37. It is relevant to various quantum optics experiments because of its high reactivity. There is only one electron in the outermost shell of ^{87}Rb and the electron's ground state is $5^2S_{1/2}$. In the $n^{2S+1}L_J$ notation, n is the principal quantum umber, S is the value of spin angular momentum, L is the value of orbital angular momentum and J is value of the total angular momentum of the outer electron. The transitions between the ground state and the first two excited states, $5^2P_{1/2}$ and $5^2P_{3/2}$, of the outer electron are called the D_1 line (795 nm) and D_2 line (780 nm) of ^{87}Rb respectively. The "D" originates from the fact that the latter two states form a fine-structure doublet (see Figure 6.1). More detailed optical properties of ^{87}Rb may be found in Ref. [108].

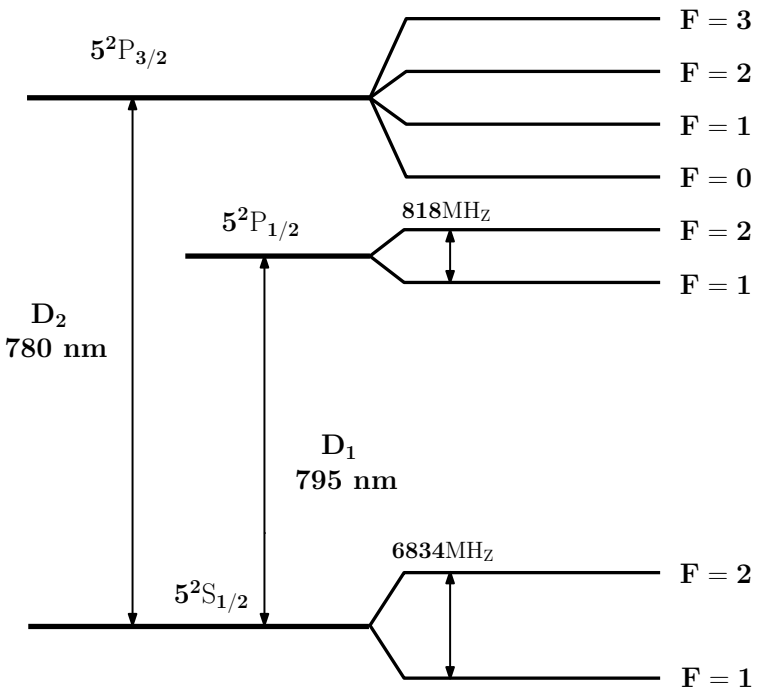

FIGURE 6.1: ^{87}Rb level diagram. The hyperfine levels are neglected in the following calculations. The D_1 line transition is then equivalent to a $J_g = 1/2 \rightarrow J_e = 1/2$ system shown in Figure 6.2. It turns out that the removal of the hyperfine structures leads to negative results in generating squeezed vacuum states, as will be shown in later sections.

Both the D_1 and D_2 lines are further split into hyperfine levels due to the coupling of $\mathbf{J}$ with the total nuclear angular momentum $\mathbf{I}$. The total atomic angular momentum $\mathbf{F}$ is given by $\mathbf{F} = \mathbf{J} + \mathbf{I}$ and the hyperfine levels are labeled by their value F. In this chapter, we consider *only the D_1 transition* and restraint ourselves to the cases where the *hyperfine structure can be neglected* [107, 109]. This can be realized by using either a high buffer gas pressure (overwhelming collisional broadening, see for example Ref. [110]) or a very intensive laser pump (overwhelming power broadening.)[1] Consequently, the D_1 line transition becomes equivalent to a $J_g = 1/2 \rightarrow J_e = 1/2$ system and both ground/excited states become degenerate. Then our system is effectively a four-level X-system shown in Figure 6.2. Moreover, we find that with general real-life parameters, the absorption of the light field in a X-system is very small and can be safely ignored. We therefore assume zero absorption of the medium (see Figure 6.3b.) Finally, we want to point out that the neglect of the hyperfine structure also ignores the Zeeman effect, which is responsible for the nonlinear magneto-optical rotation (NMOR) effect [109, 105]. The NMOR effect is closely related to polarization SR but it requires a non-zero external magnetic field. Throughout this chapter, we always assume zero external magnetic field (this can be done with an external field shield in laboratory) and degenerate ground/excited magnetic sublevels.

Strictly speaking, an *open* system configuration of X-system should be used to model the atoms that are coming in and out of the interaction region with the radiation field. This rate is denoted as γ and is the same for all levels, as shown in Figure 6.2. However, the excited levels can decay much faster than the time of flight through the interaction region because of radiation decay into states outside the X-system or the collision with other atoms. Thence we have the total decay rate of the excited state as $(\gamma_0 + \gamma + \gamma')$ where γ_0 is the rate of decaying to the ground states of the X-system. The rate of pumping fresh atoms into the

[1] According to the Rabi solution, the absorption line will have a broadened Lorentzian FWHM that depends on the intensity of the injecting field. This broadening can not be obtained from perturbation treatment where the field must be weak. See [111, 31].

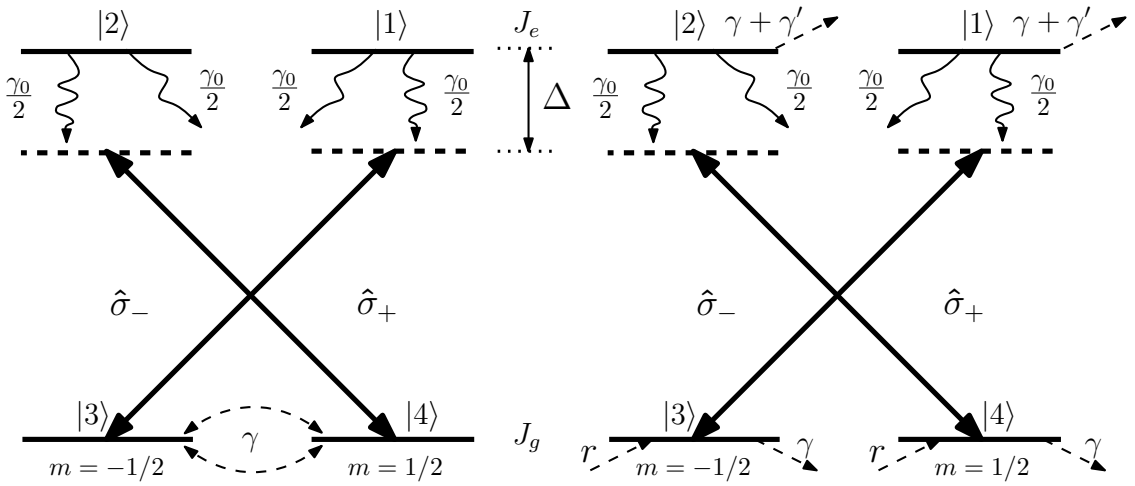

(a) Closed X-system (b) Open X-system

FIGURE 6.2: Schematic diagram for a $J_g = 1/2 \rightarrow J_e = 1/2$ (X-) system. The eigenfrequencies of the four levels are $\omega_1 = \omega_2 = \omega_e$ and $\omega_3 = \omega_4 = \omega_g$ with $\omega_0 = \omega_e - \omega_g$. $\hat{\sigma}_+(\hat{\sigma}_-)$ is the left- (right-) circularly polarized component of the light field, whose frequency is detuned by Δ from resonance. In the (a) *closed* configuration, γ_0 is the natural width of the upper states; γ denotes the population exchange rate between the ground states; in the (b) *open* configuration, the excited states decay at the rate of $\gamma_0 + \gamma + \gamma'$ while the ground states decay at the rate of γ and get repumped at rate of r. When $\gamma' \gg \gamma$ and $\gamma' = r$, the open configuration is equivalent to the closed one. See context for more detail. In such symmetric configurations, no classical self-rotation will occur when linearly polarized field is injected; however, quantum mechanical effect changes the statistics of the vacuum field on the orthogonal polarization and results in squeezed vacuum state.

interaction region is denoted by r. It is shown in Ref. [112] that when $r = \gamma' \gg \gamma$ the open system is equivalent to the *closed* system (see Figure 6.2), which we will use throughout this chapter.

6.3 Self-Rotation of a Classical Elliptically Polarized Light

Before proceeding into the calculation, we will establish an intuitive explanation for the polarization SR of elliptically polarized light field interacting with the X-system. The main mechanism we consider here is optical pumping.[2] Suppose that the atom is initially in an equal superposition of ground states $|3\rangle$ and $|4\rangle$. It starts interacting with an elliptically polarized light field (propagating along $\hat{\mathbf{z}}$) which has a stronger $\hat{\sigma}_+$ component than $\hat{\sigma}_-$component.

[2]Another popular mechanism is the ac-Stark effect [4] where the difference in the intensities of the circularly polarized components of the light field cause different energy shifts on different magnetic sublevels. The associated susceptibilities are changed because of the steep dispersion as a function of detuning (see Figure 6.3a.) However, the ac-Stark effect is usually much smaller than the optical pumping and therefore is ignored in this discussion [106].

Accordingly this will lead to uneven Rabi frequencies between the $|1\rangle \leftrightarrow |3\rangle$ and $|2\rangle \leftrightarrow |4\rangle$ transitions. Consequently, more atomic population accumulates in ground state $|3\rangle$ than $|4\rangle$. This population difference depends on the ellipticity of the light polarization.[3] The population difference between the two lower states gives rise to different real parts of the linear susceptibility of $\hat{\sigma}_{\pm}$ components of the light field, which in turn induces a phase shift between the $\hat{\sigma}_{\pm}$ components and results in the rotation of the polarization ellipse. We conclude this explanation with a comparison between polarization SR and NMOR. In polarization SR, the atomic system starts out in a symmetric configuration but the asymmetry of the elliptically polarized light field destroys the isotropy of the atomic transitions. On the other hand, in NMOR the atomic system is prepared with non-degenerate sublevels by applying an external magnetic field.

The calculation in this section is structured as follows. First we decompose both the elliptically polarized light field $\vec{E}(\vec{r},t)$ and atomic dipole operator $\vec{d}(\vec{r},t) = e\vec{r}$ into the eigenbasis of angular momentum s, *i.e.*, the left- and right-circular polarization states. From there we derive the interaction Hamiltonian $H_1 = -\vec{E}\cdot\vec{d}$ and drop several terms violating energy conservation. Then we solve the Liouville equation in for the steady-state density matrix of the X-system, which in turn gives rise to the average induced dipole per atom $\langle\vec{d}\rangle = \mathrm{Tr}(\rho\vec{d})$ and the susceptibility χ of the system. Finally we show that the different susceptibilities between left- and right-circularly polarized components of the light field lead to the polarization SR.

6.3.1 Circular Basis

As there is no unique definition of circular basis [113], we dedicate this subsection to explicitly deriving the dipole moment operator in the circular basis in detail. We start the calculation by writing the plane-wave electric field vector of the incoming light field, which is propagating

[3]The ellipticity $\epsilon \in (-\pi/4, \pi/4)$ is defined as the arctangent of the ratio between the minor and major axes of the polarization ellipse of the incoming light field. It defines the "shape" of the ellipse and when $\epsilon = \pm\pi/4$ the field is circularly polarized while when $\epsilon = 0$ is linearly polarized. Here we assume the initial ellipticity $\epsilon(z)|_{z=0}$ is small.

in $\hat{\mathbf{z}}$ and is elliptically polarized in $x-y$ plane, as

$$\vec{\mathbf{E}}(z,t) = E_x(z)\cos(kz-\omega t+\phi(z))\hat{\mathbf{x}} + E_y(z)\cos(kz-\omega t)\hat{\mathbf{y}} \tag{6.1}$$

$$= \frac{1}{2}\left(E_x(z)e^{i\phi(z)}\hat{\mathbf{x}} + E_y(z)\hat{\mathbf{y}}\right)e^{i(kz-\omega t)} + \text{c.c.}, \tag{6.2}$$

where $E_x(z)$ and $E_y(z)$ are the real positive amplitudes of the x- and y-polarized components of the light field, ω is the light frequency, $k=\omega/c$ is the vacuum wave number, $\phi(z)$ is the relative phase between the two components and c.c. stands for complex conjugate. The value of $E_x(0)$, $E_y(0)$ and $\phi(0)$ can be determined from the initial ellipticity $\epsilon(0)$. Given the wavelength of the light field is much longer than the size of the atom, we may safely drop the position-dependence of the field. However, one should notice that this approximation does not apply to $\phi(z)$, whose z-dependence is the reason for the polarization SR.

We define $\vec{\mathbf{E}}^{(\pm)}$ to be the positive and negative-frequency parts of $\vec{\mathbf{E}}(t)$ and write them in the left- and right-circular polarization bases as

$$\vec{\mathbf{E}}^{(\pm)} = \frac{1}{2}\left(E_+^{(\pm)}\hat{\sigma}_+ + E_-^{(\pm)}\hat{\sigma}_-\right), \tag{6.3}$$

where

$$E_+^{(+)} = -\frac{E_x e^{i\phi(z)} - iE_y}{\sqrt{2}} = -E_-^{(-)*},$$
$$E_-^{(+)} = \frac{E_x e^{i\phi(z)} + iE_y}{\sqrt{2}} = -E_+^{(-)*} \tag{6.4}$$

with the subscripts $\pm$ denote the left- and right-circular polarizations and

$$\hat{\sigma}_+ = -\frac{\hat{\mathbf{x}}+i\hat{\mathbf{y}}}{\sqrt{2}},$$
$$\hat{\sigma}_- = \frac{\hat{\mathbf{x}}-i\hat{\mathbf{y}}}{\sqrt{2}}.$$

These circular bases are two of the three standard components of the spherical basis[114, 15].

To derive the dipole moment in circular basis, we first write the position vector in the circular basis as

$$\vec{r} = x\hat{\mathbf{x}} + y\hat{\mathbf{y}} + z\hat{\mathbf{z}} \tag{6.5}$$

$$= r\left(\sin\theta\cos\phi\hat{\mathbf{x}} + \sin\theta\sin\phi\hat{\mathbf{y}} + \cos\theta\hat{\mathbf{z}}\right) \tag{6.6}$$

$$\propto r\left(Y_{1,-1}\hat{\sigma}_-^* + Y_{1,1}\hat{\sigma}_+^* + Y_{1,0}\hat{\mathbf{z}}\right), \tag{6.7}$$

where $Y_{l,m}$ are the spherical harmonics. Combining Eqs. (6.3) and (6.7), we have

$$\vec{r}\cdot\vec{\mathbf{E}}^{(+)} \propto r\left(E_+^{(+)}Y_{1,1} + E_-^{(+)}Y_{1,-1}\right),$$

where $\hat{\sigma}_\pm^*\cdot\hat{\sigma}_\pm = 1$ and $\hat{\sigma}_\pm\cdot\hat{\sigma}_\pm = 0$. It is clear that the $\hat{\sigma}_\pm$ components of the field induce a $\Delta m = \pm 1$ transition of the electron respectively.

To precisely evaluate the magnitude of the dipole moment, we need the Wigner-Eckart theorem [5]:

$$\langle J\ m_J|er_q|J'\ m'_J\rangle = \langle J||er||J'\rangle(-1)^{J'-1+m_J}\sqrt{2J+1}\begin{pmatrix} J' & 1 & J \\ m'_J & q & -m_J\end{pmatrix}, \tag{6.8}$$

where r_q with $q = \pm 1, 0$ represents the three spherical components of $\vec{r}$. The 3-j symbol requires that $m_J = m_{J'} + q$, otherwise it equals to zero. As an example, we consider the states $|1\rangle = |1/2\ \ 1/2\rangle$ and $|3\rangle = |1/2\ \ -1/2\rangle$ in the X-system. We then have

$$\begin{aligned}\langle 1|er_q|3\rangle &= \langle 1/2||er||1/2\rangle(-1)^0\sqrt{2}\begin{pmatrix} 1/2 & 1 & 1/2 \\ -1/2 & q & -1/2\end{pmatrix} \\ &= -\langle 1/2||er||1/2\rangle\sqrt{\frac{2}{3}}\delta_{1,q} \\ &= -\mu\delta_{1,q},\end{aligned}$$

with $\mu = \langle 1/2||er||1/2\rangle\sqrt{2/3}$ and the value of $\langle 1/2||er||1/2\rangle$ can be found in Table 6.1. Therefore $\langle 1|e\vec{r}|3\rangle = \langle 1|er_1|3\rangle\hat{\sigma}_+^* = -\mu\hat{\sigma}_+^*$ which agrees with the middle term of Eq. (6.7).[4]

[4] An arbitrary 2D vector $\vec{\mathbf{V}}$ can be expanded as a linear combination of $\vec{\mathbf{V}} = \hat{\sigma}_+^* V_+ + \hat{\sigma}_-^* V_-$ with $V_\pm = \hat{\sigma}_\pm\cdot\vec{\mathbf{V}}$

Similarly we have $\langle 2|e\vec{r}|4\rangle = \mu\hat{\sigma}_-^*$. The electric dipole operator then can be written as

$$\vec{d} = -\mu\sigma_{13}\hat{\sigma}_+^* + \mu\sigma_{31}\hat{\sigma}_-^* + \mu\sigma_{24}\hat{\sigma}_-^* - \mu\sigma_{42}\hat{\sigma}_+^*, \tag{6.9}$$

where $\sigma_{ij} = |i\rangle\langle j|$ are the atomic transition operators and h.c. stands for hermitian conjugate. Combining Eqs. (6.3) and (6.9) gives

$$\vec{d}\cdot\vec{\mathbf{E}}^{(+)} = \frac{1}{2}\left(-\mu\sigma_{13}E_+^{(+)} + \mu\sigma_{31}E_-^{(+)} + \mu\sigma_{24}E_-^{(+)} - \mu\sigma_{42}E_+^{(+)}\right).$$

However, since σ_{31} and σ_{42} have the unperturbed time dependence $e^{-i\omega_0 t}$, the two terms of $\sigma_{31}E_-^{(+)}$ and $\sigma_{42}E_+^{(+)}$ will oscillate in time as $e^{-i(\omega+\omega_0)t}$. In optics domain, these fast oscillating terms can be averaged out and are usually dropped using the *rotating-wave approximation* (RWA) [115].

6.3.2 Solving for the Atomic Density Matrix

By simplifying the negative-frequency part with the same argument, we can write the interaction Hamiltonian as

$$\begin{aligned}
H_1 =& -\vec{d}\cdot\vec{E} \\
=& -\frac{1}{2}\left(-\mu\sigma_{13}E_+^{(+)}e^{-i\omega t} + \mu\sigma_{24}E_-^{(+)}e^{-i\omega t} + \mu\sigma_{31}E_-^{(-)}e^{i\omega t} - \mu\sigma_{42}E_+^{(-)}e^{i\omega t}\right) \\
=& -\frac{1}{2}\left(-\mu\sigma_{13}E_+^{(+)}e^{-i\omega t} + \mu\sigma_{24}E_-^{(+)}e^{-i\omega t} - \mu\sigma_{31}E_+^{(+)*}e^{i\omega t} - \mu\sigma_{42}E_-^{(+)*}e^{i\omega t}\right) \\
=& \frac{1}{2}\hbar\left(\sigma_{13}\Omega_+e^{-i\omega t} - \sigma_{24}\Omega_-e^{-i\omega t} + \text{h.c.}\right),
\end{aligned} \tag{6.10}$$

using Eq. (6.4). Here $\Omega_\pm = \mu E_\pm^{(+)}/\hbar$ are the Rabi frequencies associated with $\sigma_\pm$ transitions respectively. The total Hamiltonian then becomes

$$\begin{aligned}
H &= H_0 + H_1 \\
&= \frac{1}{2}\hbar\omega_0\big(\sigma_{z13} + \sigma_{z24}\big) + \frac{1}{2}\hbar\left(\sigma_{13}\Omega_+e^{-i\omega t} - \sigma_{24}\Omega_-e^{-i\omega t} + \text{h.c.}\big),
\end{aligned} \tag{6.11}$$

where $\sigma_{zij} = |i\rangle\langle i| - |j\rangle\langle j|$ and the reference energy level is at $(\omega_g + \omega_0/2)$. Plugging this Hamiltonian into the Liouville equation gives

$$i\hbar\frac{d\rho}{dt} = [H, \rho] \tag{6.12}$$

we have

$$\begin{aligned}
\dot{\rho}_{11} &= -\frac{i}{2}(\Omega_+ e^{-i\omega t}\rho_{31} - \text{h.c.}) - \gamma_0\rho_{11},\\
\dot{\rho}_{22} &= -\frac{i}{2}(\Omega_- e^{-i\omega t}\rho_{42} - \text{h.c.}) - \gamma_0\rho_{22},\\
\dot{\rho}_{33} &= \frac{i}{2}(\Omega_+ e^{-i\omega t}\rho_{31} - \text{h.c.}) - \gamma(\rho_{33} - \rho_{44}) + \frac{\gamma_0}{2}(\rho_{11} + \rho_{22}),\\
\dot{\rho}_{44} &= \frac{i}{2}(\Omega_- e^{-i\omega t}\rho_{42} - \text{h.c.}) - \gamma(\rho_{44} - \rho_{33}) + \frac{\gamma_0}{2}(\rho_{11} + \rho_{22}),\\
\dot{\rho}_{13} &= -\frac{i}{2}\Omega_+ e^{-i\omega t}(\rho_{33} - \rho_{11}) - (\gamma + \frac{\gamma_0}{2} + i\omega_0)\rho_{13},\\
\dot{\rho}_{24} &= -\frac{i}{2}\Omega_- e^{-i\omega t}(\rho_{44} - \rho_{22}) - (\gamma + \frac{\gamma_0}{2} + i\omega_0)\rho_{24},
\end{aligned}$$

where the overhead dot stands for time derivative and $\omega_0 = \omega_e - \omega_g$ is the resonant frequency of the atom. Notice that here the decay terms γ_0 and γ are introduced into the Liouville equation phenomenologically. A more rigorous derivation using Liouville operator can be found in Ref. [116].

To remove the rapidly-oscillating terms we can transform the density matrix into a *rotating frame* such that

$$\rho_{ij} = \begin{cases} x_{ij}e^{i\omega t}, & \text{if } i \in g, j \in e;\\ x_{ij}e^{-i\omega t}, & \text{if } i \in e, j \in g;\\ x_{ij}, & \text{if } i,j \in e \text{ or } i,j \in g, \end{cases} \tag{6.13}$$

where $e = \{1, 2\}$ and $g = \{3, 4\}$. In terms of x_{ij} the Liouville equation becomes

$$\begin{aligned}
\dot{x}_{11} &= -\gamma_0 x_{11} - \frac{i}{2}(\Omega_+ x_{31} - \text{h.c.}),\\
\dot{x}_{22} &= -\gamma_0 x_{22} - \frac{i}{2}(\Omega_- x_{42} - \text{h.c.}),\\
\dot{x}_{33} &= -\gamma(x_{33} - x_{44}) + \frac{\gamma_0}{2}(x_{11} + x_{22}) + \frac{i}{2}(\Omega_+ x_{31} - \text{h.c.}),\\
\dot{x}_{44} &= -\gamma(x_{44} - x_{33}) + \frac{\gamma_0}{2}(x_{11} + x_{22}) + \frac{i}{2}(\Omega_- x_{42} - \text{h.c.}),\\
\dot{x}_{13} &= -\tilde{\Gamma}x_{13} - \frac{i}{2}\Omega_+(x_{33} - x_{11}),\\
\dot{x}_{24} &= -\tilde{\Gamma}x_{24} - \frac{i}{2}\Omega_-(x_{44} - x_{22}),
\end{aligned}$$

where $\tilde{\Gamma} = \gamma + \gamma_0/2 + i\Delta$ and $\Delta = \omega_0 - \omega$. In order to obtain the steady state solution, we require $\forall\ i, j \in e \cup g : \dot{x}_{ij} = 0$ so that

$$\begin{aligned} x_{13} &= \frac{i}{2\tilde{\Gamma}}\Omega_+(x_{11} - x_{33}), \\ x_{24} &= \frac{i}{2\tilde{\Gamma}}\Omega_-(x_{22} - x_{44}). \end{aligned} \tag{6.14}$$

The first four equations of x_{ij} are linearly dependent, therefore using the normalization condition of the atomic population we obtain

$$\begin{aligned} 0 &= -\gamma_0 x_{11} + \frac{|\Omega_+|^2}{2}(x_{33} - x_{11})\eta, \\ 0 &= -\gamma_0 x_{22} + \frac{|\Omega_-|^2}{2}(x_{44} - x_{22})\eta, \\ 0 &= -\gamma(x_{33} - x_{44}) + \frac{\gamma_0}{2}(x_{11} + x_{22}) - \frac{|\Omega_+|^2}{2}(x_{33} - x_{11})\eta, \\ 0 &= -\gamma(x_{44} - x_{33}) + \frac{\gamma_0}{2}(x_{11} + x_{22}) - \frac{|\Omega_-|^2}{2}(x_{44} - x_{22})\eta, \\ 1 &= x_{11} + x_{22} + x_{33} + x_{44}, \end{aligned} \tag{6.15}$$

where $\eta = \mathrm{Re}(\tilde{\Gamma})/|\tilde{\Gamma}|^2$.

Now it is straightforward to calculate the average induced dipole per atom

$$\begin{aligned} \langle\vec{d}\rangle &= \mathrm{Tr}(\rho\vec{d}) \\ &= \mu x_{13} e^{-i\omega t}\hat{\sigma}_-^* - \mu x_{24} e^{-i\omega t}\hat{\sigma}_+^* + \text{h.c.} \end{aligned} \tag{6.16}$$

using the results from Eqs. (6.14) and (6.15). From $\vec{P} = \varepsilon_0\chi\vec{E}$ we can identify the positive-frequency susceptibilities associated with different polarizations of the light field to be

$$\begin{aligned} \chi_{\sigma_+}^{(+)}(\Delta) &= -\frac{N}{\varepsilon_0}\frac{\mu x_{13}}{E_+^{(+)}/2} \\ &= -i\frac{N}{\hbar\varepsilon_0}\frac{\mu^2}{\tilde{\Gamma}}(x_{11} - x_{33}), \\ \chi_{\sigma_-}^{(+)}(\Delta) &= \frac{N}{\varepsilon_0}\frac{\mu x_{24}}{E_-^{(+)}/2} \\ &= -i\frac{N}{\hbar\varepsilon_0}\frac{\mu^2}{\tilde{\Gamma}}(x_{22} - x_{44}). \end{aligned} \tag{6.17}$$

Here N is the atomic density in the medium and ε_0 is the free space permittivity. The real and imaginary parts of $\chi^{(+)}_{\sigma_+}(\Delta)$ and $\chi^{(+)}_{\sigma_-}(\Delta)$ and their differences are shown in Figure 6.3a and Figure 6.3b respectively.

To describe the SR effect of the propagating field, one just needs to use the $\vec{P}$ calculated above and solve the wave equation

$$(\frac{\omega^2}{c^2} + \frac{d^2}{dz^2})\vec{E} = -\frac{4\pi}{c^2}\frac{d^2}{dt^2}\vec{P} \tag{6.18}$$

for the $\vec{E}$ field as a function of propagation distance z. This has been done in Ref. [106, 109].

6.4 Vacuum Squeezing via Polarization SR in Atomic Vapor

In 2002, Matsko *et al.* [107] predicted that it should be possible to generate a squeezed vacuum state of a light field using SR in an atomic system. They suggested that 8 dB of squeezing should be achievable. Since then a number of efforts has been made, mostly experimentally, to search the parametric space for the optimal generation of such squeezed vacuum states. However, contradictory results are reported from different groups (successful generation of a squeezed vacuum was reported in Ref. [117, 118, 119] while the authors

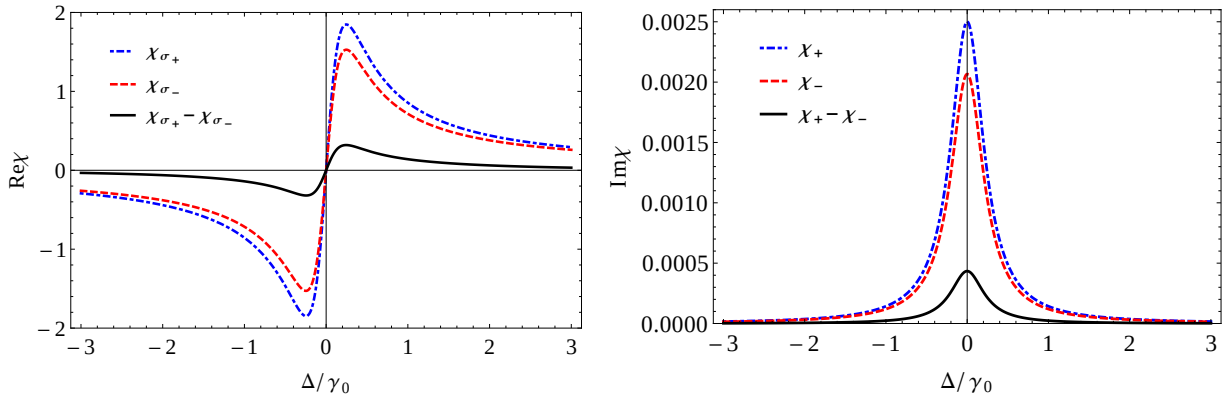

(a) (b)

FIGURE 6.3: The (a) real part (phase shift) and (b) imaginary part (absorption) of the susceptibilities are plotted as a function of the detuning Δ of the X-system. The susceptibilities associated with left- and right-circular polarization and their difference are labeled as χ_{σ_+}, χ_{σ_-} and $\chi_{\sigma_+} - \chi_{\sigma_-}$. Notice that (a) the largest SR occurs when the field is slightly off resonance and (b), given the same parameters, the magnitude of absorption is much smaller than that of the phase shift, which justifies our exclusion of absorption in the X-system.

of Ref. [120] argued that no squeezing should be seen because of the dominant resonance fluorescence.) Most of the previous work is summarized in Ref. [121, 105].

In this section, we first present the prediction made by Matsko *et al.* and then calculate the quadrature noise of the light field after interacting with the simplified X-system. No vacuum squeezing is shown in our semi-classical or quantum mechanical simulations. This negative result motivates us to calculate the power spectrum of the resonance fluorescence of the far field, which will be discussed in the next section.

6.4.1 Prediction of Vacuum Squeezing via Polarization SR

Intuitively, generating vacuum squeezing via polarization SR may be understood as follows. Assuming an elliptically polarized light field with a strong y-component and a weak x-component interacts with an SR medium, the polarization rotation projects a portion of the y-polarized field onto the x-component. As a result, the weak x-polarized field is either amplified or attenuated depending on the relative phase between the two components. Matsko *et al.* extended this analysis to the case where the x-component is in a vacuum state. They argued that because of the vacuum fluctuation from quantum mechanics, the zero component would still be able to interact with the strong component and sometimes be attenuated to a state even less noisy than the vacuum, *i.e.*, the squeezed vacuum. Another explanation of vacuum squeezing via polarization SR is provided by Mikhailov *et al.* in [119], where the generation scheme is understood to be a four-wave mixing process.

We again consider the classical electric field propagating in the $\hat{\mathbf{z}}$ direction (Eq. 6.2) as

$$\vec{\mathbf{E}}^{(\pm)}(z,t) = \frac{E_x(z)}{2} e^{\pm i(kz-\omega t+\phi(z))}\hat{\mathbf{x}} + \frac{E_y(z)}{2} e^{\pm i(kz-\omega t)}\hat{\mathbf{y}}.$$

Readers should not confuse the superscript $E^{(\pm)}$ with the circular polarization subscript $E_\pm$. The ellipticity of the light field can be calculate from the Stokes parameters [122] as

$$\epsilon = \frac{1}{2}\arcsin\frac{i(E_x^{(-)}E_y^{(+)} - E_y^{(-)}E_x^{(+)})}{|E_x|^2 + |E_y|^2}. \tag{6.19}$$

Assuming that $E_y(z) \gg E_x(z)$, *i.e.*, $\epsilon(z) \ll 1$, Eq. (6.19) becomes

$$\epsilon(z) \approx \frac{E_x(z)}{E_y(z)} \sin(\phi(z)). \tag{6.20}$$

Now consider an SR medium of length ℓ and assume that the ellipticity does not change much, *i.e.*, $\epsilon(0) = \epsilon(\ell) = \epsilon$. In such a medium the polarization ellipse rotates by an angle

$$\varphi = g\epsilon(0)\ell. \tag{6.21}$$

Here g with a dimension of inverse length is the SR parameter which, for a given medium, depends only on the intensity and frequency of the incoming light field. Now the output field at $z = \ell$ are associated with the input field by

$$\begin{bmatrix} E_x^{(+)}(\ell) \\ E_y^{(+)}(\ell) \end{bmatrix} \approx \begin{bmatrix} 1 & \varphi \\ -\varphi & 1 \end{bmatrix} \begin{bmatrix} E_x(0)e^{i\phi(0)} \\ E_y(0) \end{bmatrix} e^{i(k\ell-\omega t)}, \tag{6.22}$$

where the approximations $\cos(\varphi) \approx 1$ and $\sin(\varphi) \approx \varphi$, which are valid for small φ, are used. Combining Eqs. (6.20), (6.21) and (6.22) gives

$$E_x^{(+)}(\ell) \approx \left(E_x(0)e^{i\phi(0)} + g\ell\epsilon(0)E_y(0)\right) e^{i(k\ell-\omega t)}, \tag{6.23}$$

which describes the evolution of the incoming light field classically.

Next we try to quantize the field and search for vacuum squeezing. In order to describe the quantum vacuum squeezing, Matsko *et al.* rewrote the monochromatic electric field by replacing the classical amplitudes with photon annihilation and creation operators

$$\hat{E}_x = \frac{E_0}{2}\left(\hat{a}_x e^{i(kz-\omega t)} + \hat{a}_x^\dagger e^{-i(kz-\omega t)}\right), \tag{6.24}$$

where E_0 has the dimension of an electric field and is proportional to the square-root of ω. As the degree of squeezing depends upon the phase of the field, we need to separate the the quadrature phase χ from the propagating terms $(kz - \omega t)$. Therefore, we write Eq. (6.24) as

$$\hat{E}_x = \frac{E_0}{2}\left(\hat{a}_x(z)e^{i\chi} + \hat{a}_x^\dagger(z)e^{-i\chi}\right). \tag{6.25}$$

Notice that the field operators are now functions of position, z, but independent of time, t. This is because we now measure the phase of the field in respect to some local oscillator which rotates in the phase space with the same frequency ω as the phase of the field.

In analogy with the classical expression, we can define an ellipticity operator $\hat{\epsilon}$ for a nearly y-polarized light field as

$$\hat{\epsilon}(z) = E_0 \frac{\hat{a}_x(z) - \hat{a}_x^\dagger(z)}{2iE_y(z)}, \tag{6.26}$$

where the expectation value in a coherent state agrees with Eq. (6.20). The quantum mechanical version of Eq. (6.23) then becomes

$$\hat{E}_x^{(+)}(\ell) = \frac{E_0}{2}\left\{\hat{a}_x(0) + \frac{ig\ell}{2}\left[\hat{a}_x^\dagger(0) - \hat{a}_x(0)\right]\right\} e^{i\chi}. \tag{6.27}$$

The evolution of the annihilation operator in propagation distance can be identified as

$$\hat{a}_x(\ell) = \hat{a}_x(0) + \frac{ig\ell}{2}\left[\hat{a}_x^\dagger(0) - \hat{a}_x(0)\right]. \tag{6.28}$$

Inserting Eq. (6.28) into Eq. (6.24), we find that the phase-dependent field operator of the x-polarized component becomes

$$\hat{E}_x(\chi, \ell) = \frac{E_0}{2}\hat{a}_x(0)(e^{i\chi} - ig\ell\cos\chi) + \frac{E_0}{2}\hat{a}_x^\dagger(0)(e^{-i\chi} + ig\ell\cos\chi). \tag{6.29}$$

We can now calculate the vacuum fluctuations in the x-polarized field by assuming taht it is in a vacuum state, so $\langle\hat{E}_x(\chi,\ell)\rangle = 0$ and

$$\begin{aligned}\langle\Delta\hat{E}_x(\chi,\ell)^2\rangle &= \langle\hat{E}_x(\chi,\ell)^2\rangle - \langle\hat{E}_x(\chi,\ell)\rangle^2 \\ &= \frac{E_0^2}{4}(g^2\ell^2\cos^2\chi - 2g\ell\sin\chi\cos\chi + 1).\end{aligned} \tag{6.30}$$

It is apparent from Eq. (6.30) and Figure 6.4 that for a certain choice of the local oscillator phase, χ, the quantum noise in the x-polarized field is lower than the shot-noise-limit.

We conclude this subsection with two remarks. (a) The evolution of the field operators in Eq. (6.28) is not rigorously derived from solving the wave equation of the quantized

field, but from an analogy with the classical expression. The accuracy of this result may not be high. Therefore, we present our version of the quantum noise calculation of the polarized component in vacuum state starting from the field-atom interaction Hamiltonian in the following subsections; (b) Eq. (6.30) shows that for vacuum squeezing caused by SR, not only does the degree of squeezing increase with a longer propagation length but the squeezing angle changes as well. This can be visualized in Figure 6.5.

6.4.2 Derivation of the Interaction Hamiltonian of the X-system with Quantized Fields.

In this subsection we start by quantizing the incident light field as

$$\vec{\mathbf{E}} = \mathcal{E}\big(a_+\hat{\sigma}_+ + a_-\hat{\sigma}_- + \text{h.c.}\big), \tag{6.31}$$

where $\mathcal{E} = (\hbar\omega/2\epsilon_0 V)^{1/2}$ has the dimension of an electric field and V is the quantization volume. Notice that the annihilation operators $a_\pm$, which are associated with $\hat{\sigma}_\pm$ respectively, are time-independent because we start in the Schrdinger picture. Throughout this subsection, $\hbar$ is set to be one.

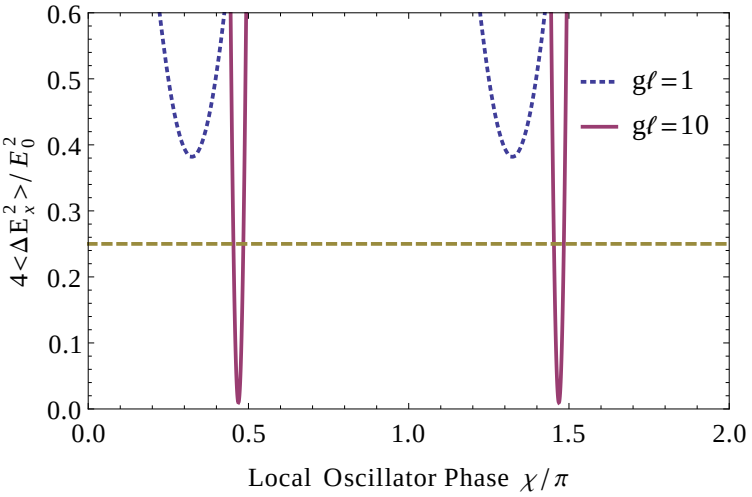

FIGURE 6.4: Normalized quantum noise of the x-polarized field in a vacuum state (calculated based on Eq. (6.29)) is plotted as a function of the local oscillator phase χ. The solid and dotted curves represent the cases of $g\ell = 10$ and $g\ell = 1$ respectively. The dashed line denotes the shot-noise limit. It is shown that with increasing propagation distance (assuming zero absorption) a higher degree of squeezing is generated and the squeezing angle is shifted by an angle ϑ. See Figure 6.5.

Now we first write down the unperturbed atomic Hamiltonian

$$\mathcal{H}_0 = \frac{\omega_0}{2}(\sigma_{z13} + \sigma_{z24}) + \omega(a_+^\dagger a_+ + a_-^\dagger a_-). \tag{6.32}$$

The last two terms on the r.h.s. account for the energy of the light field.

By combining Eqs. (6.9) and (6.31), the full quantum interaction Hamiltonian under electric dipole approximation becomes

$$\begin{aligned}
\mathcal{H}_1 =& -\vec{d}\cdot\vec{E} \\
=& \big(\mu\sigma_{13}\hat{\sigma}_+^* - \mu\sigma_{31}\hat{\sigma}_-^* - \mu\sigma_{24}\hat{\sigma}_-^* + \mu\sigma_{42}\hat{\sigma}_+^*\big)\cdot\mathcal{E}\big(a_+\hat{\sigma}_+ + a_-\hat{\sigma}_- + a_+^\dagger\hat{\sigma}_+^* + a_-^\dagger\hat{\sigma}_-^*\big) \\
=& -g\big(a_+\sigma_{13} + a_+^\dagger\sigma_{31} - a_-\sigma_{24} - a_-^\dagger\sigma_{42}\big) + g\big(a_-^\dagger\sigma_{13} + a_-\sigma_{31} - a_+^\dagger\sigma_{31} - a_+\sigma_{42}\big),
\end{aligned}$$

where $g = -\mu\mathcal{E}$. The four terms in the last parenthesis of the last equation should be dropped because of the violation of energy conservation [3]. For example, the term $a_-^\dagger\sigma_{13}$ corresponds to the process where one $\hat{\sigma}_-$ photon is emitted and the atom is raised from ground state $|3\rangle$ to excited state $|1\rangle$; on the other hand, the term $a_+\sigma_{13}$ in thefirst parenthesis describe the process where one $\hat{\sigma}_+$ photon is absorbed and the atom is raised from ground state $|3\rangle$ to excited state $|1\rangle$. The latter conserves the energy while the former results in the gain of

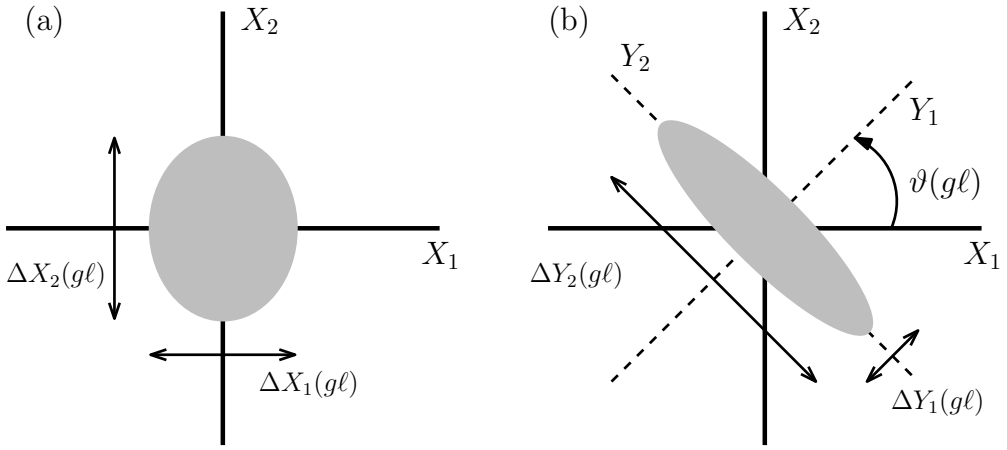

FIGURE 6.5: The phase space representation of the x-polarized component of the output light field after interacting with an SR medium of effective length (a) $g\ell = 1$ and (b) $g\ell = 10$. The level of squeezing is enhanced when the effective length of propagation is elongated. More interestingly, the phase for maximum squeezing is rotated by an $g\ell$-dependent angle ϑ.

$\omega + \omega_0$ energy. Also as before, the dropping of these four terms amounts to applying the RWA. Therefore we have

$$\mathcal{H}_1 = -g\big(a_+\sigma_{13} + a_+^\dagger\sigma_{31} - a_-\sigma_{24} - a_-^\dagger\sigma_{42}\big). \tag{6.33}$$

Similar to Eq. (6.2) we have

$$a_\pm = \frac{\mp a_x + ia_y}{\sqrt{2}}, \tag{6.34}$$

from which we may transform $\mathcal{H}_0$ and $\mathcal{H}_1$ back into the $\hat{\mathbf{x}}$ and $\hat{\mathbf{y}}$ basis as

$$\begin{aligned}
\mathcal{H}_0 =& \frac{\omega_0}{2}(\sigma_{z13} + \sigma_{z24}) + \omega(a_x^\dagger a_x + a_y^\dagger a_y), \\
\mathcal{H}_1 =& \frac{g}{\sqrt{2}}\big(a_x\sigma_{13} + a_x\sigma_{24} + \text{h.c.}\big) + \frac{g}{\sqrt{2}}\big(ia_y\sigma_{13} - ia_y\sigma_{24} + \text{h.c.}\big)
\end{aligned} \tag{6.35}$$

Eq. (6.35) is the full Hamiltonian when both x- and y-polarized components of the incident light field are considered quantum states of light. However, we usually work with lasers with intensity on the order of 1 W, which corresponds to 10^{19} photon per second on average. Therefore it is reasonable to reform the Hamiltonian so that the y-polarized component is treated classically. To do this we first note that

$$\begin{aligned}
&\langle\alpha_y e^{-i\omega t}|\left(iga_y\sigma_{13} - iga_y^\dagger\sigma_{31}\right)|\alpha_y e^{-i\omega t}\rangle \\
=& -i\langle\alpha_y|\mu\mathcal{E}a_y\sigma_{13} - \mu\mathcal{E}a_y^\dagger\sigma_{31}|\alpha_y\rangle \\
=& -i\mu\mathcal{E}\alpha_y\sigma_{13}e^{-i\omega t} + i\mu\mathcal{E}\alpha_y^*\sigma_{31}e^{i\omega t},
\end{aligned} \tag{6.36}$$

where $|\alpha_y e^{-i\omega t}\rangle$ is a strong coherent state. Notice that the time-dependence is introduced by the oscillating field and the operators are still time-independent. Recall that

$$\begin{aligned}
\mu &= -\langle 1|er_1|3\rangle \\
&= 1/\sqrt{2}\langle 1|e(x+iy)|3\rangle \\
&= 1/\sqrt{2}(\mu_{x13} + i\mu_{y13}) \\
&= \sqrt{2}i\mu_{y13},
\end{aligned}$$

where we used the fact that $\mu_{x13} = i\mu_{y13}$ which can be shown from the angular integration of spherical harmonics[113]. Therefore Eq. (6.36) becomes

$$\begin{aligned}&\sqrt{2}\mu_{y13}\mathcal{E}\alpha_y\sigma_{13}e^{-i\omega t} + \sqrt{2}\mu_{y31}\mathcal{E}\alpha_y^*\sigma_{31}e^{i\omega t}\\ =&\sqrt{2}\big(\Omega_{y13}\sigma_{13}e^{-i\omega t} + \Omega_{y13}^*\sigma_{31}e^{i\omega t}\big),\end{aligned}$$

where $\mu_{y13} = \mu_{y31}^*$ and $\Omega_{y13} = \mu_{y13}\mathcal{E}\alpha_y$ is the Rabi frequency of the $|1\rangle \to |3\rangle$ transtion induced by the y-polarized field which is now classical. Therefore Eq. (6.35) becomes

$$\begin{aligned}\mathcal{H}_0 &= \frac{\omega_0}{2}(\sigma_{z13} + \sigma_{z24}) + \omega a_x^\dagger a_x,\\ \mathcal{H}_1 &= \frac{g}{\sqrt{2}}\big(a_x\sigma_{13} + a_x\sigma_{24} + \text{h.c.}\big) + \big(\Omega_{y13}\sigma_{13}e^{-i\omega t} + \Omega_{y24}\sigma_{24}e^{-i\omega t} + \text{h.c.}\big).\end{aligned}$$

Now we may transfer the total Hamiltonian into the some *rotating frame* to get rid of its time-dependenc. First we rewrite $\mathcal{H}_0$ and $\mathcal{H}_1$ as

$$\begin{aligned}\tilde{\mathcal{H}}_0 &= \frac{\omega}{2}(\sigma_{z13} + \sigma_{z24}) + \omega a_x^\dagger a_x,\\ \tilde{\mathcal{H}}_1 &= \frac{\Delta}{2}(\sigma_{z13} + \sigma_{z24}) + \frac{g}{\sqrt{2}}\big(a_x\sigma_{13} + a_x\sigma_{24} + \text{h.c.}\big) + \big(\Omega_{y13}\sigma_{13}e^{-i\omega t} + \Omega_{y24}\sigma_{24}e^{-i\omega t} + \text{h.c.}\big)\end{aligned}$$

with $\Delta = \omega_0 - \omega$. We then transfer $\tilde{\mathcal{H}}_1$ into its interaction picture as[5]

$$\tilde{\mathcal{H}}_I = e^{i\tilde{\mathcal{H}}_0 t}\tilde{\mathcal{H}}_0 e^{-i\tilde{\mathcal{H}}_0 t}.$$

Using the Baker-Hausdorf-Campell theorem, we have

$$\begin{aligned}e^{i\omega a_x^\dagger a_x t}a_x e^{-i\omega a_x^\dagger a_x t} &= a_x e^{-i\omega t},\\ e^{i\omega a_x^\dagger a_x t}a_x^\dagger e^{-i\omega a_x^\dagger a_x t} &= a_x^\dagger e^{i\omega t},\\ e^{i\omega\sigma_{zeg}t/2}\sigma_{eg}e^{-i\omega\sigma_{zeg}t/2} &= \sigma_{eg}e^{i\omega t},\\ e^{i\omega\sigma_{zeg}t/2}\sigma_{ge}e^{-i\omega\sigma_{zeg}t/2} &= \sigma_{ge}e^{-i\omega t},\end{aligned}$$

where in the last two equantions $eg = 13$ or 24. These relations give rise to

$$\tilde{\mathcal{H}}_I = \frac{\Delta}{2}(\sigma_{z13} + \sigma_{z24}) + \frac{g}{\sqrt{2}}\big(a_x\sigma_{13} + a_x\sigma_{24} + \text{h.c.}\big) + \big(\Omega_{y13}\sigma_{13} + \Omega_{y24}\sigma_{24} + \text{h.c.}\big). \qquad (6.37)$$

[5]The time dependent rotation in general is $\tilde{V} = UVU^\dagger + i\hbar\partial U/\partial t$ where U is the unitary rotational operator. Interaction picture is just one particular case of the rotating frame where the $i\hbar\partial U/\partial t$ part is always canceled out.

6.4.3 Simulation Results

From Eq. (6.37) we may numerically simulate the evolution of the state of the x-polarized vacuum state. The equation we are trying to solve is the master equation in the Lindblad form (Eq. (6.38)), which is the most general trace-preserving and completely positive form of the non-unitarty evolution of the X-system term when interacting with the vacuum reservoir. To obtain the density matrix of the system at any future time $\rho(t)$, we have

$$\dot{\rho} = -\frac{i}{\hbar}[\tilde{\mathcal{H}}_I, \rho] - \frac{1}{2}\sum_{i=1}^{6} h_i(\rho L_i^\dagger L_i + L_i^\dagger L_i \rho - 2L_i \rho L_i^\dagger), \tag{6.38}$$

where L_i is the operator for possible decay and h_i is the corresponding constant. In our case $h_i = \gamma_0$ if the decay is from the excited states to grond states and $h_i = \gamma$ if the decay is between the two ground levels. Since we assume the incident field is polarized in y direction, the x component of the field is then in a vacuum state. The rotated quadrature operator of the x-polarized field can be defined as

$$\hat{X}_1 = \hat{a}_x e^{-i\chi} + \hat{a}_x^\dagger e^{i\chi},$$

where χ is the quadrature angel ranging in $[0, 2\pi]$. The software we use is the Quantum Toolbox in Python developed by J. R. Johansson and P. D. Nation [123, 124], which aims for simulating the dynamics of the quantum systems.

Our simulation shows that only when $g \approx \Omega \geq 10^2\gamma_0$ does significant squeezing occur. This is however, not compatible with our X-system model. On one hand, the value of g is quite fixed because of the resonant condition $\omega \approx \omega_0$ and this value is much smaller than γ_0. On the other hand, if we reduce the strength of the incident beam to $\approx 10^{-4}$ mW/cm^2 such that $\Omega \approx g$, the squeezing also disappears because we can no longer ignore the ground-state hyperfine lines at such low intensity (the highest light intensity while still resolving hyperfine structure is $\approx 10^4$ mW/cm^2.) The values of the parameters used in our simulation are summarized in Table 6.1.

The X-system is obviously an oversimplification of the real atoms. First of all, according to Ref. [119], an uneven four-level configuration of the Zeeman sublevels is necessary to avoid the trapping of atoms in one of the ground sublevels and this trapping prevents any degree of squeezing from being generated. Moreover, when the power broadening caused by the incident field is small, the ac-Stark effect and the Doppler broadening caused by atom velocity distribution should be taken into account. Finally, the quantum fluctuations of the atomic operators also affect the generation of squeezing. A more complete yet very complicated numerical calculation considering all effects above can be found in Ref. [125]. Even though the X-system model does not provide us with overall squeezing, we may still use it to calculate the power spectrum of the fluorescent radiation field and search for squeezing at different frequencies.

TABLE 6.1: Simulation Parameters

Description		Equals to	Value	Ref.
$D_1(5^2S_{1/2} \longrightarrow 5^2P_{1/2})$ Transition Dipole Matrix Element	$d_\pm$	$\langle J = \frac{1}{2}\|\|er_\pm\|\|J' = \frac{1}{2}\rangle$	2.5×10^{-29} C·m	[108]
$D_1(5^2S_{1/2} \longrightarrow 5^2P_{1/2})$ Frequency	ω_0	NA	$2\pi \cdot 3.77 \times 10^{14}$ Hz	[108]
Excited Levels Homogeneous Width	γ_0	NA	5.7×10^6 Hz	[108]
Cell Length	ℓ	NA	10 cm	[107]
Beam Diameter	D	NA	100 μm	[107]
Interaction Volume	V	$D^2\ell\pi/4$	$7.85 \cdot 10^{-9}$ m^3	[107]
Interaction Strength	g	$g = \mu\sqrt{\frac{\omega}{\hbar\epsilon_0 V}}$	$7.7 \times 10^{-3}\sqrt{\omega}$ Hz	[3]
Rabi Frequency	Ω_y	$\Omega_y = \mu E_y/\hbar$	$2.0 \times 10^5 E_y$ Hz	[3]

6.5 Fluorescence Power Spectrum of the Far Field

The resonance fluorescence originates from the scattering of the quasi-resonant incident photon by the atom. The atom is excited by absorbing one of the photons and is later de-excited by spontaneously emitting one. In contrast to stimulated emission where all emitted photons have the same direction and polarization, photons from spontaneous emission can be of any direction and polarization. The resonance fluorescence is of significant importance in studying quantum systems having a closed transition.

We first develop the relation between the field operators in the far-zone ($kr \gg 1$) and the atomic dipole operator at the atom. By assuming the atom is at the origin and the line joining the atom to the observation point r is the z-axis, we set up a coordinate system such that the field operator $\mathbf{E}^{(+)}(\mathbf{r}, \mathrm{t})$ in the far-zone of the X-system becomes (see Figure 6.6)

$$\frac{\omega_0 \mu}{4\sqrt{2}\pi c^2 \epsilon_0 r}\left\{\Big(\sigma_{31}(t-\frac{r}{c})+\sigma_{42}(t-\frac{r}{c})\Big)\hat{x}+i\Big(\sigma_{31}(t-\frac{r}{c})-\sigma_{42}(t-\frac{r}{c})\Big)\hat{y}\right\}, \tag{6.39}$$

where μ and ω_0 are defined as before. By denoting

$$I_0(r)=\left(\frac{\omega_0\mu}{4\sqrt{2}\pi c^2\epsilon_0 r}\right)^2$$

we have the x-component of the field operator as

$$\begin{aligned}
\mathrm{E}_x^{(+)}(r,t) =& \sqrt{I_0}\Big(\sigma_{31}(t-\frac{r}{c})+\sigma_{42}(t-\frac{r}{c})\Big),\\
\mathrm{E}_x^{(-)}(r,t) =& \sqrt{I_0}\Big(\sigma_{13}(t-\frac{r}{c})+\sigma_{24}(t-\frac{r}{c})\Big).
\end{aligned} \tag{6.40}$$

A detailed derivation of Eq. (6.39) is shown in Appendix A.

6.5.1 Power Spectrum and Its Detection

The power spectrum $S(\omega)$ is defined in terms of the two-time correlation function of the radiation field as

$$S(\omega)=\frac{1}{2\pi}\lim_{T\to\infty}\int_0^T dt\int_0^T dt'\langle E^{(-)}(t)E^{(+)}(t')\rangle e^{-i\omega(t-t')},$$

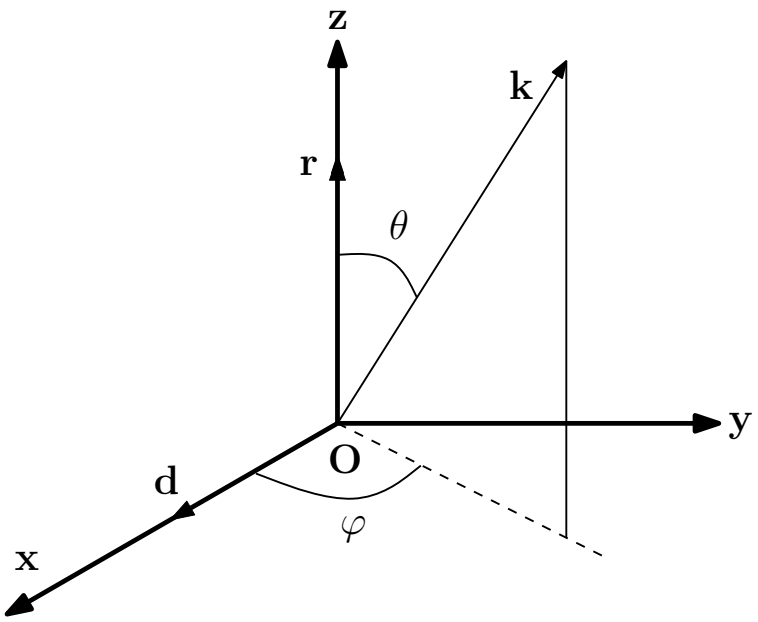

FIGURE 6.6: The coordinate of the far-field calculation. The atom is at the origin **O**, **r** is the observation point, **d** is the atomic dipole (assumed in $x-y$ plane) and **k** is the wave-vector of an arbitrary mode of the vacuum. See Appendix A for more detail.

where the expectation value is averaged over the state of the field. Under the stationary assumption, the two-time correlation only depends on the time difference $\tau = t - t'$ and the previous equation becomes

$$\begin{aligned} S(\omega) =& \frac{1}{2\pi}\int_0^\infty d\tau \big(\langle E^{(-)}(\tau)E^{(+)}(0)\rangle e^{-i\omega\tau} + \langle E^{(-)}(0)E^{(+)}(\tau)\rangle e^{i\omega\tau}\big) \\ =& \frac{1}{\pi}\mathrm{Re}\int_0^\infty d\tau \langle E^{(-)}(0)E^{(+)}(\tau)\rangle e^{i\omega\tau}. \end{aligned} \tag{6.41}$$

In the last equation the relation $\langle E^{(-)}(0)E^{(+)}(\tau)\rangle = \langle E^{(-)}(\tau)E^{(+)}(0)\rangle^*$ is used.

The detection of power spectrum is actually quite straightforward. Following Section 10.D of Ref. [3], we may consider a two-level atom interacting with linearly polarized light. We assume initially the atom is in the ground state $|b\rangle$ and the field is in state $|i\rangle$. We also require that $\omega_\alpha = \omega_a - \omega_b$ is adjustable, which can be achieved in the laboratory by applying an external magnetic field. Then the interaction picture Hamiltonian in RWA can be written as

$$\mathcal{V} = -d_{ab}\sigma_{ab}E^{(+)}(t)e^{i\omega_\alpha t} + \text{h.c.}$$

The total state then evolves as

$$|\psi(t)\rangle \approx \left(1 - \frac{i}{\hbar}\int_0^t dt'\mathcal{V}(t')\right)|b\rangle \otimes |i\rangle.$$

The probability of finding the atom at the excited state $|a\rangle$ can be found as

$$\begin{aligned} P(\omega_\alpha, t) &= \langle\psi(t)|a\rangle\langle a|\psi(t)\rangle \\ &\propto \int_0^t dt' \int_0^t dt''\langle i|E^{(-)}(t'')E^{(+)}(t')|i\rangle e^{-i\omega_\alpha(t''-t')} \\ &\propto S(\omega_\alpha). \end{aligned}$$

Therefore it is easy to see that we may detect the full power spectrum of the resonant fluorescence by tuning the energy separation of the detectors (atoms).

6.5.2 Calculation of the Two-Time Average from the Single-Time Average

It is obvious from the last subsection that to calculate the power spectrum of the radiation field we need to obtain the two-time average term $\langle E_x^{(-)}(0)E_x^{(+)}(\tau)\rangle$. According to Eq. (6.40), this is equivalent to calculating the two-time average of the atomic operators such as $\langle\sigma_{13}(0)\sigma_{31}(\tau)\rangle$.

However, by solving the Lindblad equation one obtains the density matrix elements as functions of time, which connects to only the single-time average of the atomic operators.[6] To calculate the two-time average from the single-time average, one need to use the quantum regression theorem. Here we derive the value of $\langle\sigma_{13}(0)\sigma_{31}(\tau)\rangle e^{i\omega_0\tau}$ of the X-system as an example.

First, we drop the g-dependent terms in $\tilde{\mathcal{H}}_I$ in Eq. (6.37) and solve the Lindblad equation (see Section 10.C of Ref. [3]) by flattening the density matrix $\rho(\tau)$ into a column $R(\tau)$. As a result we have

$$\dot{R}(t) = -MR(t) + B,$$

[6]The atomic operators are connected to the density matrix in such a way that $\langle\sigma_{ij}(t)\rangle = \rho_{ji}(t)\exp(i\omega_0 t)$ in the interaction picture.

where B is the constant terms. A solution can be found as

$$R(t+\tau) = \sum_l \left\{ \check{\mathbf{v}}_l \left[R(t) - M^{-1}B \right] \mathbf{v}_l e^{-\lambda_l \tau} \right\} + M^{-1}B,$$

where $\mathbf{v_l}$ is the l-th eigenvector of M with $\check{\mathbf{v}}_l$ as its transpose and λ_l as the associated eigenvalue. Throughout this calculation, we assume $t = 0$ so the previous solution becomes

$$R(\tau) = \sum_l \left\{ \check{\mathbf{v}}_l \left[R(0) - M^{-1}B \right] \mathbf{v}_l e^{-\lambda_l \tau} \right\} + M^{-1}B,$$

so that each density matrix element $\rho_{ij}(\tau)$ can be represented as a linear combination of $\rho_{ij}(0)$. In particular, for $\rho_{13}(\tau)$, we have

$$\begin{aligned}
\rho_{13}(\tau) &= \langle \sigma_{31}(\tau) \rangle e^{i\omega_0 \tau} \\
&= C_{13}^{(0)}(\tau) + C_{13}^{(1)}(\tau)\rho_{11}(0) + C_{13}^{(2)}(\tau)\rho_{13}(0) + C_{13}^{(3)}(\tau)\rho_{31}(0) + C_{13}^{(4)}(\tau)\rho_{33}(0) \\
&\quad + C_{13}^{(5)}(\tau)\rho_{22}(0) + C_{13}^{(6)}(\tau)\rho_{24}(0) + C_{13}^{(7)}(\tau)\rho_{42}(0).
\end{aligned}$$

Next we notice that $\rho_{ij}(0)$ terms can be written as $\mathrm{Tr}[\rho(0)\sigma_{ji}(0)]$ and the quantum regression theorem states that $\langle \sigma_{13}(0)\sigma_{31}(\tau) \rangle e^{i\omega_0 \tau}$ can be calculated by simply replacing $\mathrm{Tr}[\rho(0)\sigma_{ji}(0)]$ with $\mathrm{Tr}[\rho(0)\sigma_{13}(0)\sigma_{ji}(0)]$ everywhere.[7] Therefore we have

$$\begin{aligned}
&\langle \sigma_{13}(0)\sigma_{31}(\tau) \rangle e^{i\omega_0 \tau} \\
&= C_{13}^{(0)}(\tau)\mathrm{Tr}[\rho(0)\sigma_{13}(0)] + C_{13}^{(1)}(\tau)\mathrm{Tr}[\rho(0)\sigma_{13}(0)\sigma_{11}(0)] + C_{13}^{(2)}(\tau)\mathrm{Tr}[\rho(0)\sigma_{13}(0)\sigma_{31}(0)] \\
&\quad + C_{13}^{(3)}(\tau)\mathrm{Tr}[\rho(0)\sigma_{13}(0)\sigma_{13}(0)] + C_{13}^{(4)}(\tau)\mathrm{Tr}[\rho(0)\sigma_{13}(0)\sigma_{33}(0)] + C_{13}^{(5)}(\tau)\mathrm{Tr}[\rho(0)\sigma_{13}(0)\sigma_{22}(0)] \\
&\quad + C_{13}^{(6)}(\tau)\mathrm{Tr}[\rho(0)\sigma_{13}(0)\sigma_{42}(0)] + C_{13}^{(7)}(\tau)\mathrm{Tr}[\rho(0)\sigma_{13}(0)\sigma_{24}(0)] \\
&= C_{13}^{(0)}(\tau)\mathrm{Tr}[\rho(0)\sigma_{13}(0)] + C_{13}^{(2)}(\tau)\mathrm{Tr}[\rho(0)\sigma_{13}(0)\sigma_{31}(0)] + C_{13}^{(4)}(\tau)\mathrm{Tr}[\rho(0)\sigma_{13}(0)\sigma_{33}(0)] \\
&= \left(C_{13}^{(0)}(\tau) + C_{13}^{(4)}(\tau) \right)\rho_{31}(0) + C_{13}^{(2)}(\tau)\rho_{11}(0).
\end{aligned}$$

Finally, under the stationary condition, we argue that the initial density matrix elements $R(0)$ should be τ-independent so that their values can be obtained by setting $\tau \to \infty$ (so

[7] Order of σ matters.

that $\exp(-\lambda_l \tau)$ terms die out and only $M^{-1}B$ is left.) Thus the previous equation becomes

$$\langle \sigma_{13}(0)\sigma_{31}(\tau)\rangle e^{i\omega_0\tau} = \big(C_{13}^{(0)}(\tau) + C_{13}^{(4)}(\tau)\big)M^{-1}B[3] + C_{13}^{(2)}(\tau)M^{-1}B[1],$$

where $M^{-1}B[i]$ refers to the i-th element of $M^{-1}B$. Similarly, we have

$$\begin{aligned}
\langle \sigma_{13}(0)\sigma_{42}(\tau)\rangle e^{i\omega_0\tau} &= \big(C_{24}^{(0)}(\tau) + C_{24}^{(4)}(\tau)\big)M^{-1}B[3] + C_{24}^{(2)}(\tau)M^{-1}B[1] \\
\langle \sigma_{24}(0)\sigma_{42}(\tau)\rangle e^{i\omega_0\tau} &= C_{24}^{(0)}(\tau)M^{-1}B[7] + C_{24}^{(6)}(\tau)M^{-1}B[5], \\
\langle \sigma_{24}(0)\sigma_{31}(\tau)\rangle e^{i\omega_0\tau} &= C_{13}^{(0)}(\tau)M^{-1}B[7] + C_{13}^{(6)}(\tau)M^{-1}B[5]. \qquad (6.42)
\end{aligned}$$

Recall that the two-time average of the x-field $\langle E_x^{(-)}(0)E_x^{(+)}(\tau)\rangle$ is

$$I_0\big\{\langle \sigma_{13}(0)\sigma_{31}(\tau)\rangle + \langle \sigma_{13}(0)\sigma_{42}(\tau)\rangle + \langle \sigma_{24}(0)\sigma_{42}(\tau)\rangle + \langle \sigma_{24}(0)\sigma_{31}(\tau)\rangle\big\},$$

and the power spectrum $S(\omega)$ follows easily.

6.5.3 Calculation of Squeezing in Fluorescence

To determine the degree of squeezing in the fluorescence [126] we need to introduce phase dependence into the radiation field operator. We first define the x-component electric field operator with phase χ as

$$\mathrm{E}_\chi(r,t) = \mathrm{E}^{(+)}(r,t)e^{i\chi} + \mathrm{E}^{(-)}(r,t)e^{-i\chi},$$

where we have dropped the subscript x. In addition, we define $\langle A, B\rangle$ of operator A and B such that

$$\langle A, B\rangle = \langle (A - \langle A\rangle)(B - \langle B\rangle)\rangle.$$

It is easy to see that the condition for squeezing in the radiation field is

$$\langle : \mathrm{E}_\chi(r,t), \mathrm{E}_\chi(r,t) : \rangle < 0,$$

where '::' means that the operators are in normal order. This leads to a definition of the normally-ordered squeezing power spectrum similar to Eq. (6.41)

$$: S(\omega) : = \frac{1}{2\pi}\int_0^\infty d\tau \big(\langle : E_\chi(0), E_\chi(\tau) : \rangle e^{i\omega\tau} + \langle : E_\chi(\tau), E_\chi(0) : \rangle e^{-i\omega\tau}\big), \qquad (6.43)$$

where the last equation comes from the stationary condition. For the first part of the integrand of the previous equation, we have

$$\begin{aligned}
&\langle : E_\chi(0), E_\chi(\tau) : \rangle \\
&= \langle E^{(+)}(0), E^{(+)}(\tau)\rangle e^{2i\chi} + \langle E^{(-)}(\tau), E^{(+)}(0)\rangle + \langle E^{(-)}(0), E^{(+)}(\tau)\rangle + \langle E^{(-)}(0), E^{(-)}(\tau)\rangle e^{-2i\chi} \\
&= K_1 e^{2i\chi} + K_2 + K_3 + K_4 e^{-2i\chi}
\end{aligned}$$

where

$$\begin{aligned}
K_1 &= \langle \sigma_{31}(\tau), \sigma_{31}(0)\rangle + \langle \sigma_{31}(\tau), \sigma_{42}(0)\rangle + \langle \sigma_{42}(\tau), \sigma_{31}(0)\rangle + \langle \sigma_{42}(\tau), \sigma_{42}(0)\rangle, \\
K_2 &= \langle \sigma_{13}(\tau), \sigma_{31}(0)\rangle + \langle \sigma_{13}(\tau), \sigma_{42}(0)\rangle + \langle \sigma_{24}(\tau), \sigma_{31}(0)\rangle + \langle \sigma_{24}(\tau), \sigma_{42}(0)\rangle, \\
K_3 &= \langle \sigma_{13}(0), \sigma_{31}(\tau)\rangle + \langle \sigma_{13}(0), \sigma_{42}(\tau)\rangle + \langle \sigma_{24}(0), \sigma_{31}(\tau)\rangle + \langle \sigma_{24}(0), \sigma_{42}(\tau)\rangle, \\
K_4 &= \langle \sigma_{13}(0), \sigma_{13}(\tau)\rangle + \langle \sigma_{13}(0), \sigma_{24}(\tau)\rangle + \langle \sigma_{24}(0), \sigma_{13}(\tau)\rangle + \langle \sigma_{24}(0), \sigma_{24}(\tau)\rangle. \qquad (6.44)
\end{aligned}$$

In addition, we can easily show that

$$\begin{aligned}
\langle \sigma_{eg}(\tau), \sigma_{ge}(0)\rangle &= \langle \sigma_{eg}(0), \sigma_{ge}(\tau)\rangle, \\
\langle \sigma_{ge}(\tau), \sigma_{ge}(0)\rangle &= \langle \sigma_{eg}(0), \sigma_{eg}(\tau)\rangle,
\end{aligned}$$

where $|e\rangle$ and $|g\rangle$ are any excited and ground state, respectively. Therefore we have $K_1 = K4, K_2 = K_3$ and the first (also the second) integrand becomes

$$\langle : E_\chi(0), E_\chi(\tau) : \rangle = 2 * K_1 \cos 2\chi + 2 * K_2.$$

Eq. (6.43) then reads

$$: S(\omega) := \frac{1}{\pi} \int_0^\infty d\tau (K_1 \cos 2\chi + K_2)(e^{i\omega\tau} + e^{-i\omega\tau}).$$

It is obvious that $: S(\omega) :=: S(-\omega) :$, which manifests the fact that frequencies from different sides of the laser frequency are correlated [126]. The in-phase quadrature ($\chi = 0$) squeezing spectrum becomes

$$: S_{\text{in}}(\omega) : = \frac{1}{\pi} \int_0^\infty d\tau (K_1 + K_2)(e^{i\omega\tau} + e^{-i\omega\tau}),$$

while the out-of-phase quadrature ($\chi = \pi/2$) squeezing spectrum becomes

$$: S_{\text{out}}(\omega) : = \frac{1}{\pi} \int_0^\infty d\tau(-K_1 + K_2)(e^{i\omega\tau} + e^{-i\omega\tau}).$$

By combining Eqs. (6.42) and (6.44) and assuming resonant condition, we have

$$: S_{\text{in}}(\omega, \Delta = 0) : = \frac{\gamma_0^2\Omega^2 \left(2\gamma_0^2 \left(\omega^2 + 3\Omega^2\right) + 8\gamma_0^4 - \omega^2\Omega^2 + \Omega^4\right)}{\pi \left(\gamma_0^2 + \omega^2\right)\left(2\gamma_0^2 + \Omega^2\right)\left(\gamma_0^2 \left(5\omega^2 + 4\Omega^2\right) + 4\gamma_0^4 + \left(\omega^2 - \Omega^2\right)^2\right)}, \quad (6.45)$$

$$: S_{\text{out}}(\omega, \Delta = 0) : = \frac{\gamma_0^2\Omega^2 \left(2\gamma_0^2 \left(\Omega^2 - \omega^2\right) - 8\gamma_0^4 + 3\omega^2\Omega^2\right)}{\pi \left(\gamma_0^2 + \omega^2\right)\left(2\gamma_0^2 + \Omega^2\right)\left(\gamma_0^2 \left(5\omega^2 + 4\Omega^2\right) + 4\gamma_0^4 + \left(\omega^2 - \Omega^2\right)^2\right)}, \quad (6.46)$$

where Ω is the driving Rabi frequency and γ_0 is the natural width of the excited states of the X-system.

As shown in Figure 6.7a, when the driving field is strong ($\Omega = 10\gamma_0$) the side-band peaks appear at $\omega = \sqrt{\Omega^2 + \Delta^2}$ in both on- and off-resonance fluorescence spectra [127]. Moreover, the in-phase quadrature is squeezed under significant detuning from resonance. Our simulation shows that the degree of squeezing increases with growing driving field, Ω, and the optimal detuning is always $\Delta = \Omega$. In contrast, when the driving field is weak as shown in Figure 6.8b, the side-band peaks disappear and the out-of-phase quadrature is squeezed. Integration over all ω of Eq. (6.46) leads to the total variance of the out-of-phase quadrature and we can show that when $\Omega^2/\gamma_0^2 < 2$ there is squeezing present in the *total field*.

We conclude this section with several remarks. (a) The physical mechanisms responsible for the on- and off-resonance squeezing are different. When the incident light frequency ω is very close to the resonance frequency ω_0, most of the photons are absorbed through stimulated absorption and some of them are spontaneously emitted with the same frequency. This leads to the resonant fluorescence and it requires a large decay rate, γ_0, (*i.e.*, small Ω) for squeezing to be seen. On the other hand, when the field is far-detuned (large Δ) a fraction of the incident photons are elastically scattered from the atom without being absorbed. The photons are diffracted in any direction because of the size of the atom is much smaller than the field wavelength. (b) The far-field and local atomic relation derived in Appendix

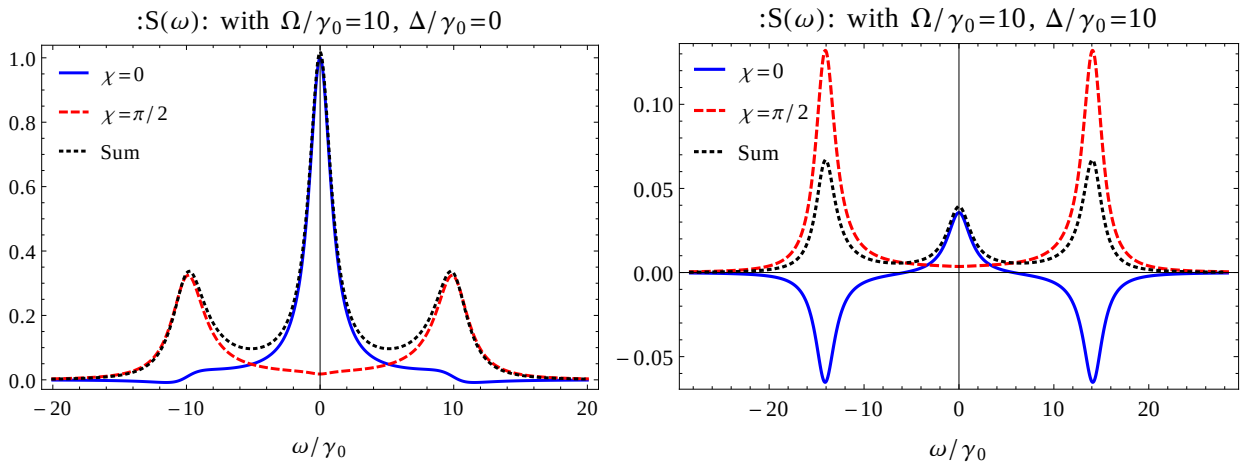

FIGURE 6.7: The squeezing power spectrum of the resonance fluorescence of a X-system driven by a linear polarized field. Spectra of both in-phase ($\chi = 0$) and out-of-phase ($\chi = \pi/2$) quadratures and their sum are shown. Here we choose the Rabi frequency $\Omega = 10\gamma_0$, where γ_0 is natrual width of the excited atomic states. (a) When $\Delta = 0$ both quadratures shows no squeezing since their spectra are positive; (b) When $\Delta = 10\gamma_0$, the in-phase quadrature is squeezed at $\omega = \pm\sqrt{\Omega^2 + \Delta^2}$ where a maximum squeezing of $:S(\omega) := -0.065$ (1.3 dB) is found. The resonance spectrum peaks at side-bands $\pm\Omega$ under strong driving field as expected (Mollow triplet) [127].

A connects the field modes to the atomic modes and is therefore independent of the state of the driving field.[8] Thus it applies to both mechanisms we just discussed. Also notice that the polarization of the radiation field in the far-zone depends only on that of the atomic dipole. (c) Our results agree with Ref. [126] in the low intensity regime and agrees with Ref. [125], where a different method (Heisenberg-Langevin approach) is used, in the high intensity regime.

6.6 Conclusion

In this chapter we have discussed the generation of vacuum squeezing via polarization self-rotation of the incident linearly polarized light field. The SR system we used is the symmetric four-level X-system reduced from the D1 line of ^{87}Rb. We showed that elliptically polarized classical light induces uneven interactions between different transitions and undergoes self-rotation. This calculation is done by treating the incident field classically. Then we argue that

[8] Just like my advisor Prof. Jon Dowling always likes to say, "a mode is a mode is a mode!"

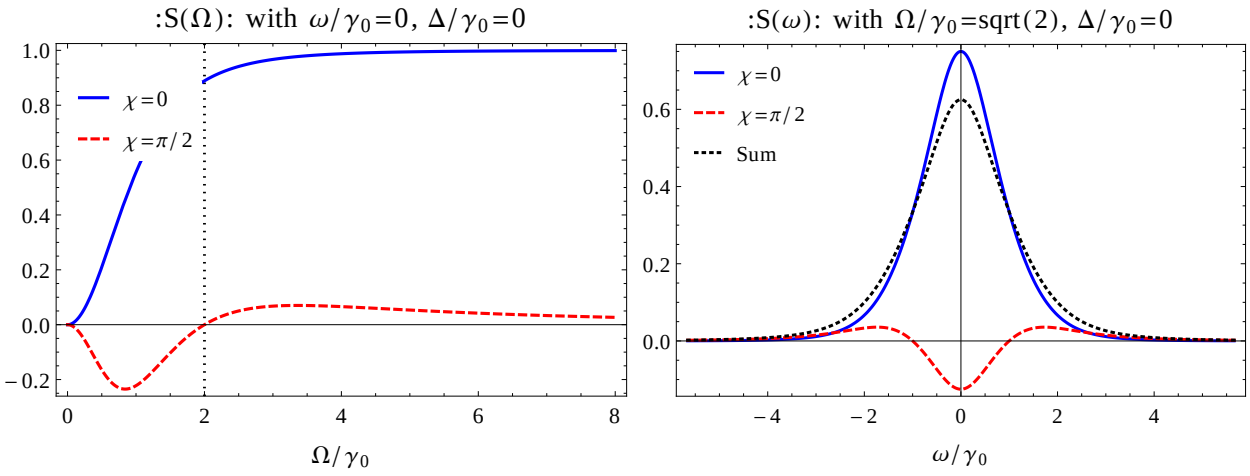

FIGURE 6.8: Under the resonance condition $\Delta = 0$, (a) it can be shown from Eq. (6.46) that when $\Omega^2/\gamma_0^2 \leq 4$ squeezing occurs in the out-of-phase quadrature spectrum; (b) by integrating Eq. (6.46) over all ω we can show that when $\Omega^2/\gamma_0^2 < 2$, there is squeezing present in the out-of-phase quadrature of the *total field*. Also we can see that with weak driving field, the scattering spectrum has no side-band peaks. Both (a) and (b) agree with the two-level atom results in Ref. [126]

such self-rotation of linearly-polarized light field may lead to vacuum squeezing following the analogy made by Matsko *et al*. Later we explicitly calculated the noise spectrum of the light field originally in vacuum state and squeezing is found under extreme conditions. Finally, we studied the fluorescence spectrum of the radiation field at the far-zone and discovered squeezing under both low and high intensity conditions.

A series of experiments on the generation and application of the squeezed vacuum via polarization SR have been conducted by Dr. Novikova's research group in William and Mary University. Readers interested in more experimental progress on this subject may find several of their papers helpful [121, 119, 105].

Bibliography

[1] P. A. M. Dirac. The quantum theory of the emission and absorption of radiation. *Proc. Roy. Soc.*, A114:243, 1927.

[2] E. Fermi. Quantum theory of radiation. *Rev. Mod. Phys.*, 4:87–132, Jan 1932.

[3] M. O. Scully and M. S. Zubairy. *Quantum Optics*. Cambridge University Press, 1997.

[4] C C. Gerry and P.L. Knight. *Introductory Quantum Optics*. Cambridge University Press, 2005.

[5] J J. Sakurai. *Modern Quantum Mechanics*. Addison Wesley, 1993.

[6] Bernard Yurke, Samuel L. McCall, and John R. Klauder. SU(2) and SU(1,1) interferometers. *Phys. Rev. A*, 33:4033–4054, 1986.

[7] P. R. Bevington. *Data Reduction and Error Analysis for the Physical Sciences*. McGraw-Hill, New York, 1969.

[8] R. A. Fisher. Theory of statistical estimation. *Proc. Cambridge Philos. Soc.*, 22:700, 1925.

[9] J. J. Cooper. *Quantum Metrology with Bose-Einstein Condenstates*. PhD thesis, University of Leeds, 2011.

[10] Samuel L. Braunstein and Carlton M. Caves. Statistical distance and the geometry of quantum states. *Phys. Rev. Lett.*, 72:3439–3443, May 1994.

[11] C. W. Helstrom. *Quantum detection and estimation theory*. Academic Press, New York, 1976.

[12] S. L. Braunstein, C. M. Caves, and G. J. Milburn. Generalized uncertainty relations: Theory, examples, and lorentz invariance. *Annals of Physics*, 247:135, 1996.

[13] Carlton M. Caves. Quantum-mechanical noise in an interferometer. *Phys. Rev. D*, 23:1693–1708, Apr 1981.

[14] T. Ono. *Generation of multi-photon states with phase sensitivities at the Heisenberg limit by interference of coherent light and squeezed vacuum*. PhD thesis, Advanced Science of Matter Hiroshima University, 2010.

[15] G. Gilbert, A. Aspect, and C. Fabre. *Introduction to Quantum Optics: From the Semi-classical Approach to Quantized Light*. Cambridge University Press, 2010.

[16] Jonathan P. Dowling. Quantum optical metrology the lowdown on high-n00n states. *Contemp. Phys.*, 49:125–143, 2008.

[17] M. A. Nielsen and I. L. Chuang. *Quantum Computation and Quantum Information*. cambridge university press, 2000.

[18] Christoph F. Wildfeuer, Austin P. Lund, and Jonathan P. Dowling. Strong violations of bell-type inequalities for path-entangled number states. *Phys. Rev. A*, 76:052101, Nov 2007.

[19] H. Lee, P. Kok, and J. P. Dowling. A quantum rosetta stone for interferometry. *J. Mod. Opt.*, 49:2325, 2002.

[20] C. M. Caves and A Shaji. Quantum-circuit guide to optical and atomic interferometry. *Opt. Commun.*, 283:695, 2010.

[21] P. Walther, J. W. Pan, M. Aspelmeyer, R. Ursin, S. Gasparoni, and A. Zeilinger. De broglie wavelength of a non-local four-photon state. *Nature*, 429:158, 2004.

[22] Christopher C. Gerry and Jihane Mimih. The parity operator in quantum optical metrology. *Contemp. Phys.*, 51(6):497–511, 2010.

[23] Joseph Jacobson, Gunnar Björk, Isaac Chuang, and Yoshihisa Yamamoto. Photonic de broglie waves. *Phys. Rev. Lett.*, 74:4835–4838, Jun 1995.

[24] Animesh Datta, Lijian Zhang, Nicholas Thomas-Peter, Uwe Dorner, Brian J. Smith, and Ian A. Walmsley. Quantum metrology with imperfect states and detectors. *Phys. Rev. A*, 83:063836, 2011.

[25] Nicholas Thomas-Peter, Brian J. Smith, Animesh Datta, Lijian Zhang, Uwe Dorner, and Ian A. Walmsley. Real-world quantum sensors: Evaluating resources for precision measurement. *Phys. Rev. Lett.*, 107:113603, 2011.

[26] Mark A. Rubin and Sumanth Kaushik. Loss-induced limits to phase measurement precision with maximally entangled states. *Phys. Rev. A*, 75:053805, 2007.

[27] G. Gilbert, M. Hamrick, and Y. S. Weinstein. Practical quantum interferometry using photonic n00n states. *Proc. SPIE*, 6573:65730K, 2007.

[28] A D. Parks, S. E. Spence, J. E. Troupe, and N. J. Rodecap. Tripartite loss model for mach-zehnder interferometers with application to phase sensitivity. *Rev. Sci. Instrum*, 76:043103, 2007.

[29] Sean D. Huver, Christoph F. Wildfeuer, and Jonathan P. Dowling. Entangled fock states for robust quantum optical metrology, imaging, and sensing. *Phys. Rev. A*, 78:063828, 2008.

[30] Ryan T. Glasser, Hugo Cable, Jonathan P. Dowling, Francesco De Martini, Fabio Sciarrino, and Chiara Vitelli. Entanglement-seeded, dual, optical parametric amplification: Applications to quantum imaging and metrology. *Phys. Rev. A*, 78:012339, Jul 2008.

[31] R. Loudon. *The Quantum Theory of Light*. Oxford University Press, thrid edition edition, 2000.

[32] C W. Gardiner and P. Zoller. *Quantum Noise*. Springer, Berilin, 2004.

[33] B. M. Escher, R. L. de Matos Filho, and L. Davidovich. General framework for estimating the ultimate precision limit in noisy quantum-enhanced metrology. *Nature Physics*, 7:406, 2011.

[34] Tae-Woo Lee, Sean D. Huver, Hwang Lee, Lev Kaplan, Steven B. McCracken, Changjun Min, Dmitry B. Uskov, Christoph F. Wildfeuer, Georgios Veronis, and Jonathan P. Dowling. Optimization of quantum interferometric metrological sensors in the presence of photon loss. *Phys. Rev. A*, 80:063803, 2009.

[35] U. Dorner, R. Demkowicz-Dobrzanski, B. J. Smith, J. S. Lundeen, W. Wasilewski, K. Banaszek, and I. A. Walmsley. Optimal quantum phase estimation. *Phys. Rev. Lett.*, 102:040403, 2009.

[36] R. Demkowicz-Dobrzanski, U. Dorner, B. J. Smith, J. S. Lundeen, W. Wasilewski, K. Banaszek, and I. A. Walmsley. Quantum phase estimation with lossy interferometers. *Phys. Rev. A*, 80:013825, 2009.

[37] K. J. Resch, K. L. Pregnell, R. Prevedel, A. Gilchrist, G. J. Pryde, J. L. O'Brien, and A. G. White. Time-reversal and super-resolving phase measurements. *Phys. Rev. Lett.*, 98:223601, 2007.

[38] Vittorio Giovannetti, Seth Lloyd, Lorenzo Maccone, and Jeffrey H. Shapiro. Sub-rayleigh-diffraction-bound quantum imaging. *Phys. Rev. A*, 79:013827, 2009.

[39] M. W. Mitchell, J. S. Lundeen, and A. M. Steinberg. Super-resolving phase measurements with a multiphoton entangled state. *Nature*, 429:161, 2004.

[40] Eli Yablonovitch and Rutger B. Vrijen. Optical projection lithography at half the rayleigh resolution limit by two-photon exposure. *Opt. Eng.*, 38(2):334–338, February 1999.

[41] Tomohisa Nagata, Ryo Okamoto, Jeremy L. O'Brien, Keiji Sasaki, and Shigeki Takeuchi. Beating the standard quantum limit with four-entangled photons. *Science*, 316:726, 2007.

[42] J. J. Bollinger, Wayne M. Itano, D. J. Wineland, and D. J. Heinzen. Optimal frequency measurements with maximally correlated states. *Phys. Rev. A*, 54:R4649–R4652, Dec 1996.

[43] Christopher C. Gerry. Heisenberg-limit interferometry with four-wave mixers operating in a nonlinear regime. *Phys. Rev. A*, 61:043811, Mar 2000.

[44] R. A. Campos, Christopher C. Gerry, and A. Benmoussa. Optical interferometry at the heisenberg limit with twin fock states and parity measurements. *Phys. Rev. A*, 68:023810, 2003.

[45] Kaushik P. Seshadreesan, Sejong Kim, Jonathan P. Dowling, and Hwang Lee. Phase estimation at the quantum cramér-rao bound via parity detection. *Phys. Rev. A*, 87:043833, Apr 2013.

[46] Taesoo Kim, Olivier Pfister, Murray J. Holland, Jaewoo Noh, and John L. Hall. Influence of decorrelation on heisenberg-limited interferometry with quantum correlated photons. *Phys. Rev. A*, 57:4004–4013, 1998.

[47] Aravind Chiruvelli and Hwang Lee. Parity measurements in quantum optical metrology. *J. Mod. Opt.*, 58:945–953, 2011.

[48] I. S. Gradshteyn and I. M. Ryzhik. *Table of Integrals Series and Products*. Academic press, fourth edition, 1965.

[49] Adriana E. Lita, Aaron J. Miller, and Sae Woo Nam. Counting near-infrared single-photons with 95% efficiency. *Opt. Express*, 16:3032–3040, 2008.

[50] Christopher C. Gerry, A. Benmoussa, and R. A. Campos. Quantum nondemolition measurement of parity and generation of parity eigenstates in optical fields. *Phys. Rev. A*, 72:053818, 2005.

[51] William N. Plick, Petr M. Anisimov, J. P. Dowling, H. Lee, and Girish S. Agarwal. Parity detecion in quantum optical metrology without number-resolving detectors. *New J. Phys.*, 12:113025, 2010.

[52] H. Carmichael. *Statistical Methods in Quantum Optics, Vol 1*. Springer-Verlag, 1991.

[53] C. Cohen-Tannoudji, J. Dupont-Roc, and G. Grynberg. *Atom-Photon Interactions: Basic Processes and Applications*. Wiley-VCH, 1998.

[54] A. Al-Qasimi and D. F. V. James. Nonexistence of entanglement sudden death in dephasing of high noon states. *Opt. Lett.*, 34:268, 2009.

[55] K. Jacobs. *Stochastic Processes for Physicists: Understanding Noisy Systems*. Cambridge University Press, 2010.

[56] Kebei Jiang, Chase J. Brignac, Yi Weng, Moochan B. Kim, Hwang Lee, and Jonathan P. Dowling. Strategies for choosing path-entangled number states for optimal robust quantum-optical metrology in the presence of loss. *Phys. Rev. A*, 86:013826, Jul 2012.

[57] Agedi N. Boto, Pieter Kok, Daniel S. Abrams, Samuel L. Braunstein, Colin P. Williams, and Jonathan P. Dowling. Quantum interferometric optical lithography: Exploiting entanglement to beat the diffraction limit. *Phys. Rev. Lett.*, 85:2733–2736, 2000.

[58] Pieter Kok, Agedi N. Boto, Daniel S. Abrams, Colin P. Williams, Samuel L. Braunstein, and Jonathan P. Dowling. Quantum-interferometric optical lithography: towards arbitrary two-dimensional patterns. *Phys. Rev. A*, 63:063407, May 2001.

[59] P. Kok, S. L. Braunstein, and J. P. Dowling. Quantum lithography, entanglement and heisenberg-limited parameter estimation. *J. Opt. B*, 6:S811–S815, 2004.

[60] Marco Lanzagorta. *Quantum Radar*. Morgan & Claypool, 2012.

[61] G. Gilbert and Y. S. Weinstein. Aspects of practical remote quantum sensing. *J. Mod. Opt.*, 55:3283–3291, 2008.

[62] G. Gilbert, M. Hamrick, and Y. S. Weinstein. Use of maximally entangled n-photon states for practical quantum interferometry. *J. Opt. Soc. Am. B*, 25:1336–1340, 2008.

[63] Sergey Knysh, Vadim N. Smelyanskiy, and Gabriel A. Durkin. Scaling laws for precision in quantum interferometry and the bifurcation landscape of the optimal state. *Phys. Rev. A*, 83:021804, Feb 2011.

[64] Y. Gao, P. M. Anisimov, C. F. Wildfeuer, J. Luine, H. Lee, and J. P. Dowling. Super-resolution at the shot-noise limit with coherent states and photon-number-resolving detectors. *J. Opt. Soc. Am. B*, 27:A170–A174, 2010.

[65] Y. Gao and H. Lee. Sub-shot-noise quantum optical interferometry: a comparison of entangled state performance within a unified measurement scheme. *J. Mod. Opt.*, 55:3319–3327, 2008.

[66] Christopher C. Gerry, Adil Benmoussa, and R. A. Campos. Nonlinear interferometer as a resource for maximally entangled photonic states: Application to interferometry. *Phys. Rev. A*, 66:013804, Jul 2002.

[67] Danna Rosenberg, Adriana E. Lita, Aaron J. Miller, and Sae Woo Nam. Noise-free high-efficiency photon-number-resolving detectors. *Phys. Rev. A*, 71:061803, Jun 2005.

[68] A. I. Lvovsky and M. G. Raymer. Continuous-variable optical quantum-state tomography. *Rev. Mod. Phys.*, 81:299–332, Mar 2009.

[69] M. Hillery, R. F. OConnell, M. O. Scully, and E. P. Wigner. Distribution functions in physics: fundamentals. *phys. rep.*, 106:121, 1984.

[70] K. E. Cahill and R. J. Glauber. Density operators and quasiprobability distributions. *Phys. Rev.*, 177:1882–1902, Jan 1969.

[71] Antoine Royer. Wigner function as the expectation value of a parity operator. *Phys. Rev. A*, 15:449–450, Feb 1977.

[72] K. Banaszek, C. Radzewicz, K. Wódkiewicz, and J. S. Krasiński. Direct measurement of the wigner function by photon counting. *Phys. Rev. A*, 60:674–677, Jul 1999.

[73] U. Leonhardt. *Measuring the Quantum State of Light*. Cambridge University Press, 1997.

[74] Emanuele Distante, Miroslav Ježek, and Ulrik L. Andersen. Deterministic superresolution with coherent states at the shot noise limit. *Phys. Rev. Lett.*, 111:033603, Jul 2013.

[75] H. S. Eisenberg. (private communication, 2012).

[76] R. H. Dicke. The measurement of thermal radiation at microwave frequencies. *Rev. Sci. Instrum.*, 17:268–275, 1946.

[77] T. Stevenson, D. Benford, C. Bennett, N. Cao, D. Chuss, K. Denis, W. Hsieh, A. Kogut, S. Moseley, J. Panek, G. Schneider, D. Travers, K. U-Yen, G. Voellmer, and E. Wollack. Cosmic microwave background polarization detector with high efficiency, broad bandwidth, and highly symmetric coupling to transition edge sensor bolometers. *J. Low Temp. Phys.*, 151:471–476, 2008.

[78] J. Zmuidzinas and P. L. Richards. Superconducting detectors and mixers for millimeter and submillimeter astrophysics. *Proc. IEEE*, 92:1597, 2004.

[79] A. Belmonte. Statistical model for fading return signals in coherent lidars. *Appl. Opt.*, 49:67371748, 2010.

[80] Gabriel A. Durkin and Jonathan P. Dowling. Local and global distinguishability in quantum interferometry. *Phys. Rev. Lett.*, 99:070801, 2007.

[81] Milena D'Angelo, Maria V. Chekhova, and Yanhua Shih. Two-photon diffraction and quantum lithography. *Phys. Rev. Lett.*, 87:013602, 2001.

[82] Ole Steuernagel. On the concentration behaviour of entangled photons. *J. Opt. B: Quantum Semiclass. Opt.*, 6:S606, 2004.

[83] P. R. Hemmer, A. Muthukrishnan, M. O. Scully, and M. S. Zubairy. Quantum lithography with classical light. *Phys. Rev. Lett.*, 96:163603, 2006.

[84] Qingqing Sun, Philip R. Hemmer, and M. Suhail Zubairy. Quantum lithography with classical light: Generation of arbitrary patterns. *Phys. Rev. A*, 75:065803, 2007.

[85] Mankei Tsang. Relationship between resolution enhancement and multiphoton absorption rate in quantum lithography. *Phys. Rev. A*, 75:043813, 2007.

[86] Kaige Wang and De-Zhong Cao. Subwavelength coincidence interference with classical thermal light. *Phys. Rev. A*, 70:041801, 2004.

[87] S. J. Bentley and R. W. Boyd. Nonlinear optical lithography with ultra-high subrayleigh resolution. *Opt. Express*, 12:5735, 2004.

[88] A. Pe'er, B. Dayan, M. Vucelja, Y. Silberberg, and A. Friesem. Quantum lithography by coherent control of classical light pulses. *Opt. Express*, 12:6600, 2004.

[89] M. Kiffner, J. Evers, and M. S. Zubairy. Resonant interferometric lithography beyond the diffraction limit. *Phys. Rev. Lett.*, 100:073602, 2008.

[90] Zeyang Liao, M. Al-Amri, and M. Suhail Zubairy. Quantum lithography beyond the diffraction limit via rabi oscillations. *Phys. Rev. Lett.*, 105:183601, 2010.

[91] Alexey V. Gorshkov, Liang Jiang, Markus Greiner, Peter Zoller, and Mikhail D. Lukin. Coherent quantum optical control with subwavelength resolution. *Phys. Rev. Lett.*, 100:093005, 2008.

[92] Wenchao Ge, P. R. Hemmer, and M. Suhail Zubairy. Quantum lithography with classical light. *Phys. Rev. A*, 87:023818, 2013.

[93] Pieter Kok, Hwang Lee, and Jonathan P. Dowling. Creation of large-photon-number path entanglement conditioned on photodetection. *Phys. Rev. A*, 65:052104, Apr 2002.

[94] C. K. Hong, Z. Y. Ou, and L. Mandel. Measurement of subpicosecond time intervals between two photons by interference. *Phys. Rev. Lett.*, 59:2044–2046, 1987.

[95] Itai Afek, Oron Ambar, and Yaron Silberberg. High-noon states by mixing quantum and classical light. *Science*, 328:879, 2010.

[96] Hwang Lee, Pieter Kok, Nicolas J. Cerf, and Jonathan P. Dowling. Linear optics and projective measurements alone suffice to create large-photon-number path entanglement. *Phys. Rev. A*, 65:030101, 2002.

[97] J. Kim, S. Takeuchi, Y. Yamamoto, and H. H. Hogue. *Appl. Phys. Lett.*, 74:902, 1999.

[98] S. Takeuchi, J. Kim, Y. Yamamoto, and H. H. Hogue. *Appl. Phys. Lett.*, 74:1063, 1999.

[99] Travis Horrom, Robinjeet Singh, Jonathan P. Dowling, and Eugeniy E. Mikhailov. Quantum-enhanced magnetometer with low-frequency squeezing. *Phys. Rev. A*, 86:023803, Aug 2012.

[100] D. F. Walls. Squeezed states of light. *Nature*, 1983.

[101] H. Yuen and J. H. Shapiro. Optical communication with two-photon coherent states — part i: Quantum-state propagation and quantum-noise. *IEEE Transactions on Information Theory*, 24:657, November 1978.

[102] H. Yuen and J. H. Shapiro. Generation and detection of two-photon coherent states in degenerate four-wave mixing. *Opt. Lett.*, 4:334, 1979.

[103] Carlton M. Caves and Bonny L. Schumaker. New formalism for two-photon quantum optics. i. quadrature phases and squeezed states. *Phys. Rev. A*, 31:3068–3092, May 1985.

[104] Bonny L. Schumaker and Carlton M. Caves. New formalism for two-photon quantum optics. ii. mathematical foundation and compact notation. *Phys. Rev. A*, 31:3093–3111, May 1985.

[105] T. S. Horrom. *Experimental Generation and Manipulation of Quantum Squeezed Vacuum via Polarization Self-Rotation in Rb Vapor*. PhD thesis, College of William and Mary, 2013.

[106] S. M. Rochester, D. S. Hsiung, D. Budker, R. Y. Chiao, D. F. Kimball, and V. V. Yashchuk. Self-rotation of resonant elliptically polarized light in collision-free rubidium vapor. *Phys. Rev. A*, 63:043814, Mar 2001.

[107] A. B. Matsko, I. Novikova, G. R. Welch, D. Budker, D. F. Kimball, and S. M. Rochester. Vacuum squeezing in atomic media via self-rotation. *Phys. Rev. A*, 66:043815, Oct 2002.

[108] Daniel A. Steck. *Rubidium 87 D Line Data*, 2001.

[109] Irina Borisovna Novikova. *Nonlinear Magneto-Optic Effects in optically dense Rb vapor*. PhD thesis, Texas A&M University, 2003.

[110] W. V. Davis, A. L. Gaeta, and R. W. Boyd. Polarization-ellipse rotation by induced gyrotropy in atomic vapors. *Opt. Lett.*, 1992.

[111] M. III. Sargent, M. O. Scully, and W. E. Jr. Lamb. *Laser Physics*. Addison Wesley, 1974.

[112] H. Lee, Y. Rostovtsev, C. J. Bednar, and A. Javan. From laser-induced line narrowing to electro-magnetically induced transparency: closed system analysis. *Appl. Phys. B*, 76:33, 2003.

[113] L. Allen and J. H. Eberly. *Optical Resonance and Two-Level Atoms*. Dover, 1987.

[114] C. J. Foot. *Atomic Physics*. Oxford University Press, 2005.

[115] D. A. Steck. *Quantum and Atom Optics*. available online at http://steck.us/teaching (revision 0.8.3, 25 May 2012).

[116] S. Mukamel. *Principles of Nonlinear Optical Spectroscopy*. Oxford University Press, 1995.

[117] J. Ries, B. Brezger, and A. I. Lvovsky. Experimental vacuum squeezing in rubidium vapor via self-rotation. *Phys. Rev. A*, 68:025801, Aug 2003.

[118] V. Josse, A. Dantan, L. Vernac, A. Bramati, M. Pinard, and E. Giacobino. Polarization squeezing with cold atoms. *Phys. Rev. Lett.*, 91:103601, Sep 2003.

[119] E. E. Mikhailov, A. Lezama, T. W. Noel, and I. Novikova. Vacuum squeezing via polarization self-rotation and excess noise in hot rb vapors. *Journal of Modern Optics*, 56:18, 2009.

[120] M. T. L. Hsu, G. Hétet, A. Peng, C. C. Harb, H.-A. Bachor, M. T. Johnsson, J. J. Hope, P. K. Lam, A. Dantan, J. Cviklinski, A. Bramati, and M. Pinard. Effect of atomic noise on optical squeezing via polarization self-rotation in a thermal vapor cell. *Phys. Rev. A*, 73:023806, Feb 2006.

[121] T. Horrom, A. Lezama, S. Balik, M. D. Havey, and E. E. Mikhailov. Quadrature noise in light propagating through a cold ^{87}rb atomic gas. *Journal of Modern Optics*, 58:1936, 2011.

[122] D. Goldstein. *Polarized Light*. Marcel Dekker, Inc., 2003.

[123] J.R. Johansson, P.D. Nation, and Franco Nori. Qutip: An open-source python framework for the dynamics of open quantum systems. *Computer Physics Communications*, 183(8):1760 – 1772, 2012.

[124] J.R. Johansson, P.D. Nation, and Franco Nori. Qutip 2: A python framework for the dynamics of open quantum systems. *Computer Physics Communications*, 184(4):1234 – 1240, 2013.

[125] A. Lezama, P. Valente, H. Failache, M. Martinelli, and P. Nussenzveig. Numerical investigation of the quantum fluctuations of optical fields transmitted through an atomic medium. *Phys. Rev. A*, 77:013806, Jan 2008.

[126] M. J. Collett, D. F. Walls, and P. Zoller. Spectrum of squeezing in resonance fluorescence. *Optics Communications*, 52:145, 1984.

[127] B. R. Mollow. Power spectrum of light scattered by two-level systems. *Phys. Rev.*, 188:1969, 1969.

Appendix A. Far Field Operator

Follwoing Section 10.A of Ref. [3], we start with the interaction Hamiltonian of a two-level atom with the radiation field

$$\mathcal{H} = \frac{\omega_0}{2}\sigma_z + \sum_{\mathbf{k},\lambda} \omega_k a^\dagger_{\mathbf{k},\lambda} a_{\mathbf{k},\lambda} + \sum_{\mathbf{k},\lambda} g_{\mathbf{k},\lambda}\big(a_{\mathbf{k},\lambda}\sigma_+ e^{i\mathbf{k}\cdot\mathbf{r_0}} + a^\dagger_{\mathbf{k},\lambda}\sigma_- e^{-i\mathbf{k}\cdot\mathbf{r_0}}\big).$$

Here $\sigma_\pm$ are the atomic raising and lowering operators and $a_{\mathbf{k},\lambda}$ is the annihilation operator associated with the radiation mode of wave-number $\mathbf{k}$ and polarization λ. Notice this Hamiltonian is written in the Schrdinger picture and RWA is applied. As before we set $\hbar = 1$ and the $\mathbf{r} = \mathbf{r_0}$ comes from the dipole approximation. For simplicity, we assume the atom is at the origin, *i.e.*, $\mathbf{r_0} = \mathbf{0}$ from now on. By introducing the slowly varying operators $\tilde{a}_{\mathbf{k},\lambda}$ and $\tilde{\sigma}_-$ such that

$$a_{\mathbf{k},\lambda}(t) = \tilde{a}_{\mathbf{k},\lambda}(t)e^{-i\omega_k t},$$

$$\sigma_-(t) = \tilde{\sigma}_-(t)e^{-i\omega_0 t}.$$

The time evolution of the field operators becomes

$$\dot{\tilde{a}}_{\mathbf{k},\lambda}(t) = -ig_{\mathbf{k},\lambda}\tilde{\sigma}_-(t)e^{-i(\omega_0-\omega_k)t},$$

which then can be formally integrated to yield

$$\dot{\tilde{a}}_{\mathbf{k},\lambda}(t) = \dot{\tilde{a}}_{\mathbf{k},\lambda}(0) - ig_{\mathbf{k},\lambda}e^{-i(\omega_0-\omega_k)t}\int_0^t dt'\tilde{\sigma}_-(t')e^{i(\omega_0-\omega_k)(t-t')}.$$

We will concentrate on the second term which contains the field-atom interaction.

Next we may write the positive frequency part of the radiation field as

$$\mathbf{E}^{(+)}(\mathbf{r},\mathrm{t}) = \sum_{\mathbf{k},\lambda} \mathcal{E}_k \hat{\epsilon}_{\mathbf{k},\lambda} a_{\mathbf{k},\lambda}(t)e^{i\mathbf{k}\cdot\mathbf{r}},$$

where $\hat{\epsilon}_{\mathbf{k},\lambda}$ is the polarization unit vector of mode $a_{\mathbf{k},\lambda}$ and $\mathcal{E}_k = (\omega_k/2\epsilon_0 V)^{1/2}$ as before. Notice the field depends on $\mathbf{r}$ but not $\mathbf{r}_0$ anymore. On substituting for $a_{\mathbf{k},\lambda}(t)$ we obtain

$$\mathbf{E}^{(+)}(\mathbf{r},\mathrm{t}) = \frac{i}{16\pi^3\epsilon_0}e^{-i\omega_0 t}\int d^3k \sum_\lambda \hat{\epsilon}_{\mathbf{k},\lambda}[\hat{\epsilon}_{\mathbf{k},\lambda}\cdot\mathbf{d}]\omega_k e^{i\mathbf{k}\cdot\mathbf{r}}\int_0^t dt'\tilde{\sigma}_-(t')e^{i(\omega_0-\omega_k)(t-t')},$$

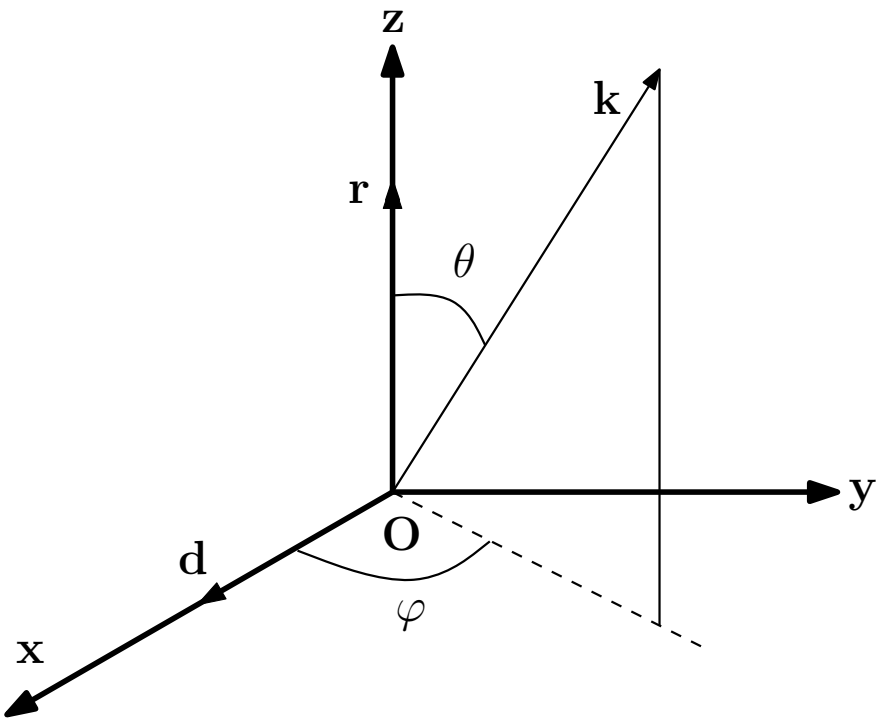

where the sum is replaced by an integral as

$$\sum_{\mathbf{k}} \to \frac{V}{(2\pi)^3} \int d^3k.$$

By using the relation between the polarization and wave-vector that[9]

$$\sum_{\lambda} \hat{\epsilon}_{\mathbf{k},\lambda} \hat{\epsilon}_{\mathbf{k},\lambda} = 1 - \frac{\mathbf{kk}}{k^2},$$

we have the field operator as

$$\mathbf{E}^{(+)}(\mathbf{r}, \mathrm{t}) = \frac{i}{16\pi^3 \epsilon_0} e^{-i\omega_0 t} \int dk d\theta d\varphi k^2 \sin\theta \left(\mathbf{d} - \frac{\mathbf{k}(\mathbf{k}\cdot\mathbf{d})}{k^2} \right) \omega_k e^{i\mathbf{k}\cdot\mathbf{r}} \times \int_0^t dt' \tilde{\sigma}_-(t') e^{i(\omega_0 - \omega_k)(t-t')}.$$

Now we assume the line joining the atom to the observation point to be the z- axis and consider the case where $\mathbf{d} = d\hat{x}$, see Figiure above. With

$$\mathbf{k} = k(\hat{x}\sin\theta\cos\varphi + \hat{y}\sin\theta\sin\varphi + \hat{z}\cos\theta),$$

[9]These are the dyadic product, or tensor product, of the two vectors.

we may first calculate the φ-integration of the field operator. For the x-component

$$\begin{aligned}
&\int_0^{2\pi} d\varphi\left(\hat{x}\cdot\mathbf{d}-\frac{(\hat{x}\cdot\mathbf{k})(\mathbf{k}\cdot\mathbf{d})}{k^2}\right)\\
=\;&\int_0^{2\pi} d\varphi d\left(1-\sin^2\theta\cos^2\varphi\right)\\
=\;&2\pi d\left(1-\frac{1}{2}\sin^2\theta\right);
\end{aligned}$$

and it is easy to see that y- and z- components both vanish.

Next we calculate the θ-integration. By denoting $\beta=\cos\theta$ we have the x- component as

$$\begin{aligned}
&2\pi d\int_0^{\pi} d\theta\left(1-\frac{1}{2}\sin^2\theta\right)\sin\theta e^{i\mathbf{k}\cdot\mathbf{r}}\\
=\;&2\pi d\int_{-1}^{1} d\beta\left(1-\frac{1}{2}(1-\beta^2)\right)e^{ikr\beta}\\
=\;&2\pi d\left(\frac{e^{ikr}-e^{-ikr}}{ikr}+O\big(r^{-2}\big)\right).
\end{aligned}$$

By dropping the $O(r^{-2})$ term in the far-zone region ($kr\gg 1$) we have, for an electric dipole $\mathbf{d}=d\hat{x}$, the electric field operator becomes

$$\begin{aligned}
\mathbf{E}^{(+)}(\mathbf{r},\mathrm{t})=\frac{cd\hat{x}}{8\pi^2\epsilon_0 r}e^{-i\omega_0 t}\int_0^{\infty} dk\,k^2\left(e^{ikr}-e^{-ikr}\right)\\
\times\int_0^{t} dt'\tilde{\sigma}_-(t')e^{i(\omega_0-\omega_k)(t-t')}.
\end{aligned}$$

By rewriting $\omega_k=ck$ and expanding the lower limit to $-\infty$, the radial integral of last equation reads

$$\begin{aligned}
&\int_{-\infty}^{\infty} dk\,k^2\left(e^{ikr}-e^{-ikr}\right)e^{-ick(t-t')}\\
=\;&-\frac{2\pi}{c^3}\left(\frac{\partial}{\partial t'}\right)^2\left\{\delta\left(t'-t+\frac{r}{c}\right)-\delta\left(t'-t-\frac{r}{c}\right)\right\}.
\end{aligned}$$

This is because

$$\begin{aligned}
&\int_{-\infty}^{\infty} dk\, k^2 e^{ikr} e^{-ick(t-t')} \\
= & -\int_{-\infty}^{\infty} dk \frac{1}{c^2}\left(\frac{\partial}{\partial t'}\right)^2 e^{ikr} e^{-ick(t-t')} \\
= & -\frac{1}{c^3}\left(\frac{\partial}{\partial t'}\right)^2 \int_{-\infty}^{\infty} d(ck) e^{i(ck)(t'-t+r/c)} \\
= & -\frac{1}{c^3}\left(\frac{\partial}{\partial t'}\right)^2 \delta\left(t'-t+\frac{r}{c}\right).
\end{aligned}$$

Therefore the electric field operator now reads

$$\begin{aligned}
\mathbf{E}^{(+)}(\mathbf{r},\mathrm{t}) = & \frac{cd\hat{x}}{8\pi^2\epsilon_0 r}\int_0^t dt' \tilde{\sigma}_-(t') e^{-i\omega_0 t'} \\
& \times\left(-\frac{2\pi}{c^3}\left(\frac{\partial}{\partial t'}\right)^2\left\{\delta\left(t'-t+\frac{r}{c}\right)-\delta\left(t'-t-\frac{r}{c}\right)\right\}\right).
\end{aligned}$$

Given that

$$\begin{aligned}
&\int_0^t dt'\left(\frac{\partial}{\partial t'}\right)^2 \delta\left(t'-t+\frac{r}{c}\right)\tilde{\sigma}_-(t') e^{-i\omega_0 t'} \\
= & \int_0^t dt'\left(\frac{\partial}{\partial t'}\right)^2\left(\tilde{\sigma}_-(t') e^{-i\omega_0 t'}\right)\delta\left(t'-t+\frac{r}{c}\right) \\
= & \int_0^t dt' e^{-i\omega_0 t'}\left(-\omega_0^2\tilde{\sigma}_-(t')-2i\omega_0\dot{\tilde{\sigma}}_-(t')+\ddot{\tilde{\sigma}}_-(t')\right)\delta\left(t'-t+\frac{r}{c}\right) \\
= & -\omega_0^2\, e^{-i\omega_0(t-r/c)}\tilde{\sigma}_-(t-r/c),
\end{aligned}$$

where only the leading terms of $\tilde{\sigma}_-(t)$ is kept, we have

$$\begin{aligned}
\mathbf{E}^{(+)}(\mathbf{r},\mathrm{t}) = & \frac{\omega_0 d\hat{x}}{4\pi c^2\epsilon_0 r}\left(e^{-i\omega_0(t-r/c)}\tilde{\sigma}_-(t-r/c)-e^{-i\omega_0(t+r/c)}\tilde{\sigma}_-(t+r/c)\right) \\
= & \frac{\omega_0 d}{4\pi c^2\epsilon_0 r}\sigma_-(t-r/c)\hat{x},
\end{aligned}$$

where the slowly varying transform is used and incoming wave part is dropped.

Similarly, for a dipole along y-axis, *i.e.*, $\mathbf{d} = d\hat{y}$ we have

$$\mathbf{E}^{(+)}(\mathbf{r},\mathrm{t}) = \frac{\omega_0 d}{4\pi c^2\epsilon_0 r}\sigma_-(t-r/c)\hat{y}.$$

Recall that the electric dipole operator of the X-system can be written as

$$\begin{aligned}\vec{d} &= -\mu\sigma_{13}\hat{\sigma}_{+}^{*} + \mu\sigma_{31}\hat{\sigma}_{-}^{*} + \mu\sigma_{24}\hat{\sigma}_{-}^{*} - \mu\sigma_{42}\hat{\sigma}_{+}^{*} \\ &= \frac{\mu}{\sqrt{2}}\Big\{\Big(\sigma_{13} + \sigma_{31} + \sigma_{24} + \sigma_{42}\Big)\hat{x} - i\Big(\sigma_{13} - \sigma_{31} - \sigma_{24} + \sigma_{42}\Big)\hat{y}\Big\},\end{aligned}$$

the field of operator in the far-zone of the X-system then becomes

$$\begin{aligned}\mathbf{E}^{(+)}(\mathbf{r},\mathrm{t}) = &\frac{\omega_0\mu}{4\sqrt{2}\pi c^2\epsilon_0 r} \\ &\times\Big\{\Big(\sigma_{31}(t-\frac{r}{c}) + \sigma_{42}(t-\frac{r}{c})\Big)\hat{x} + i\Big(\sigma_{31}(t-\frac{r}{c}) - \sigma_{42}(t-\frac{r}{c})\Big)\hat{y}\Big\}.\end{aligned}$$

Appendix B. Permission to Use Publications

The following are the copyright policies of the American Physical Society (APS) and American Institute of Physics (AIP) from

- https://journals.aps.org/copyrightFAQ.html

and

- http://www.aip.org/publishing/authors/copyright-reuse,

respectively. Here I am copying the corresponding text from the above websites which allows me to use my published works in this dissertation.

'Yes, the author has the right to use the article or a portion of the article in a thesis or dissertation without requesting permission from APS, provided the bibliographic citation and the APS copyright credit line are given on the appropriate pages.'

'AIP permits authors to include their published articles in a thesis or dissertation. It is understood that the thesis or dissertation may be published in print and/or electronic form and offered for sale, as well as included in a university's repository. Formal permission from AIP is not needed. If the university requires written permission, however, we are happy to supply it.'

Vita

Kebei Jiang was born in 1985, in Changsha, Hunan, China. He finished his undergraduate studies at South China University of Technology July 2007. In August 2007 he came to Louisiana State University to pursue graduate studies in phsics. He is currently a candidate for the degree of Doctor of Philosophy in physics, which will be awarded in August 2014.